ISSN 1075-7015, Geology of Ore Deposits, 2007, Vol. 49, No. 2, pp. 87–128. © Pleiades Publishing, Ltd., 2007.
Original Russian Text © N.S. Bortnikov, G.N. Gamyanin, O.V. Vikent'eva, V.Yu. Prokof'ev, V.A. Alpatov, A.G. Bakharev, 2007, published in Geologiya Rudnykh Mestorozhdenii, 2007, Vol. 49, No. 2, pp. 99–145.

Fluid Composition and Origin in the Hydrothermal System of the Nezhdaninsky Gold Deposit, Sakha (Yakutia), Russia

N. S. Bortnikov[a], G. N. Gamyanin[b], O. V. Vikent'eva[a], V. Yu. Prokof'ev[a], V. A. Alpatov[b], and A. G. Bakharev[b]

[a]*Institute of Geology of Ore Deposits, Petrography, Mineralogy, and Geochemistry, Russian Academy of Sciences, Staromonetnyi per. 35, Moscow, 119017 Russia*

[b]*Institute of Geology of Diamonds and Precious Metals, Siberian Division, Russian Academy of Sciences, pr. Lenina 39, Yakutsk, 677891 Republic of Sakha (Yakutia), Russia*

Received June 15, 2006

Abstract—Petrochemical characteristics of igneous, sedimentary, and metasomatic rocks; chemical and isotopic compositions of minerals and fluids; and *PT* parameters of mineral formation at the Nezhdaninsky deposit are reported. A model of hydrothermal system formation is developed on this basis. In addition to decreasing Ba/Rb and Li/Mg ratios in the course of the hydrothermal process, resulting in the formation of ore-bearing metasomatic rocks, increasing K/Ba and diminishing K/Cs ratios indicate the probable participation of magmatic fluid in the ore deposition. The agreement of the K/Rb and K/Ba ratios with the values typical of the main trend of igneous rocks (MT) implies that the K, Rb, and Ba contents were distributed in the ore-forming hydrothermal fluid according to the ratios in the source magmatic chamber. The K/Rb ratios in metasomatic rocks correspond to the MT and approach the pegmatitic–hydrothermal trend and the composition of orthomagmatic fluid of Mo–W greisen. Similar REE patterns of igneous and terrigenous rocks do not allow the REE source to be constrained unequivocally. The lithological control of lithophile element distribution testifies to the supply of host rock components to the hydrothermal system. All studied rocks and minerals are enriched in LREE. The REE total and the contribution of HREE decrease from preore to synore metasomatic rocks, from preore to regenerated carbonates, and from older to younger scheelite. A similar tendency is noted in granitoids of the Kurum pluton. The $\delta^{18}O$ values of quartz range from +10.3 to +12.6‰ in Au–Mo–W zones, from +15.9 to +16.4‰ in metasomatic rocks, from +14.8 to +16.6‰ in gold-ore veins, and from +13.5 to +16.9‰ in silver–base-metal ore mineralization. The estimates of $\delta^{18}O_{H_2O}$ suggest that water was supplied from a magmatic source ($\delta^{18}O$ = +(5.5–9.0‰)) and as a product of sedimentary rock dehydration. High-temperature (up to 390°C) and highly concentrated (up to 31 wt % NaCl equiv) fluids participated in the mineral formation. The phase separation of the fluid into H_2O–CO_2 liquid and predominantly carbon dioxide gas was combined with mixing of a high-temperature and relatively highly concentrated chloride solution with a low-temperature and poorly mineralized fluid. The redox conditions varied from equilibrium with CH_4-bearing fluid at the gold–molybdenum–tungsten stage to equilibrium with CO_2-bearing fluid during the gold-ore stage.

DOI: 10.1134/S1075701507020018

INTRODUCTION

The Nezhdaninsky deposit, one of Russia's largest, with gold reserves of above 470 t (Konstantinov et al., 2000) is located in the upper reaches of the Tyry River, the right tributary of the Aldan River, at the western spurs of the Suntar-Khayata Range at a distance of 160 km from the settlement of Khandyga, with a population of ~10000 people (the center of the administrative district). The deposit was discovered by G.F. Gurin in 1951. The Nezhdaninsky deposit is a part of northerly widening meridional tectonomagmatic zone up to 15 km long and 4 km wide (on average), where ore occurrences different in composition are localized autonomously (Gamyanin et al., 2000, 2003; Konstantinov et al., 2000). As a result of long-term geological investigations, it has been possible to reconstruct the structural evolution of the deposit, ascertain the ore-feeding and ore-controlling role of faults, characterize the mineralogy of ore and the chemical composition of minerals, outline the vertical mineralogical and geochemical zoning of the deposit, and establish elevated Au contents in sulfides of altered rocks (Gamyanin, 1985).

To estimate the fluid regime, ore deposition conditions, and evolution of ore-forming fluids, fluid inclusions and stable isotopes (S, C, and O) have been studied in minerals (Bortnikov et al., 1998a). It has been established that the ore was formed from two immiscible fluids: (i) aqueous–carbon dioxide with N_2, CH_4, and dissolved chlorides (up to 4.5 wt % NaCl equiv)

Corresponding author: N.S. Bortnikov. E-mail: bns@igem.ru

and (ii) gas-phase mainly composed of CO_2 and CH_4. Sulfur, water, and carbon dioxide of magmatic origin were prevalent in the fluid and mixed with the components taken from host rocks.

Thus, the available mineralogical, geological, isotopic, and geochemical data allowed us to suggest that gold orebodies at the Nezhdaninsky deposit are related to magmatic processes; however, the isotopic evidence could not be interpreted unequivocally. Further confirmation of the contribution of magmatic fluid to the gold-ore deposition may be derived from the behavior of REEs and other trace elements in igneous and related hydrothermally altered rocks. As is known, the distribution of Cs, Tl, Li, Rb, Sr, and Ba between magma and fluid is determined by partition coefficients and follows certain trends described by the ratios of elements to one another or to potassium (Shaw, 1968; Faibridge, 1972); these trends differ from those in amagmatic systems (Kerrich and Fryer, 1988). Our study of the distribution of REEs and other trace elements in igneous and country rocks, as well as in minerals from hydrothermal veins and metasomatic rocks, was supplemented by investigation of fluid inclusions and the oxygen isotopic composition of gold–quartz and Au–Mo–W veins and regenerated ore.

Gold–molybdenum–tungsten mineralization was found near contacts of intrusive bodies (Bakharev et al., 2002; Gamyanin et al., 2003). Both gold–quartz and Au–Mo–W veins at the Nezhdaninsky deposit are considered to be derivatives of the same ore–magmatic system.

The study of the fluid regime in the Nezhdaninsky hydrothermal–magmatic system and recognition of the nature of mineral-forming fluid(s) is an important task. The activity of this system resulted in the formation of a gold deposit classified with orogenic or veined and stringer–disseminated types (Groves et al., 2005). The origin of these deposits and their genetic relation to magmatism is a matter of hot debate. Some researchers regard these types as genetically different, and others, as genetically allied (Bierlein and Maher, 2001). The views on their origin vary from statements that assert a hydrothermal–sedimentary model to ideas of a magmatic or metamorphic mode of ore deposition (Buryak et al., 1990; Hodgson et al., 1993; Kurbanov et al., 1994; Sidorov and Tomson, 2000; Kerrich et al., 2000; Groves et al., 2003). American and Australian geologists uphold the idea of a predominant contribution of metamorphic fluids to their genesis (Goldfarb et al., 1989). The deposits in the northern Cordillera were formed in relation to meteoric convective systems (Nesbitt and Muchlenbachs, 1989). The study of fluid inclusions and stable isotopes in minerals from some gold deposits of the former Soviet Union that are hosted in terrigenous sequences led to the hypothesis of a prevalent role of magmatic fluid (Bortnikov, 1995, 2006; Bortnikov et al., 1993, 1996, 1997, 1998a, 1998b, 2004) that mixed with fluid of metamorphic origin.

GEOLOGICAL OUTLINE

Regional Geology

The Nezhdaninsky ore field is situated in the northern portion of the South Verkhoyansk Synclinorium of the Verkhoyansk Nappe–Fold Belt in the back zone of the easterly located Uda–Murgal and Okhotsk–Chukotka volcanic–plutonic belts (Fig. 1). The geological evolution of the synclinorium and the area of the Nezhdaninsky deposit, in particular, was related to accretion along the Okhotsk active continental margin (Prokop'ev et al., 2003).

The ore field as a part of the Kurum–Gel'dy ore–magmatic system (Fig. 2) is composed of rocks belonging to the Verkhoyansk Complex, which comprises the Lower and Upper Permian sandshale sequences that make up the complexly built and overturned Dyba Anticline (Fig. 3). The western limb of the anticline is gently dipping, while the eastern limb is steep and mainly overturned (Gamyanin et al., 2000). The ore field is localized at the intersection of four fault systems, the Kideriki near-meridional, the Tyry latitudinal, and the Suntar and Khalyya diagonal systems, which break the crest of the anticline into a number of horst-shaped blocks. The Ozerny and Eastern faults bound the ore field on the west and east. The periclinal closure of the Dyba Anticline at the level of the roof of the ore-bearing Dzhuptaga Formation serves as the southern boundary, close to the Gel'dy group of stocks. The northern boundary, along the northern contact of the Kurum granitoid pluton, is conditional and is based on waning of ore mineralization at the drainage divide of the Kurum and Bol'shie Kideriki creeks (Figs. 2, 3).

Magmatism

The sedimentary rocks within the ore field are cut through by various intrusive bodies. The Kurum granite–granodiorite pluton, the Gel'dy group of dioritic stocks, and a swarm of 30 basic and intermediate dikes are known (Bakharev, 1999a, 1999b; Gamyanin and Grinberg, 1973; Gamyanin et al., 2000, 2003).

The Kurum granite–granodiorite pluton, about 6.5 km^2 in exposed area, is situated near the north-northeastern periphery of the ore field. The pluton is composed largely of granodiorite and to a lesser extent of leucogranite, which occurs in the central portion of the pluton. Dikes and veins of aplite-like granite, aplite, and pegmatite cross the contact zones of the pluton. K–Ar, $^{40}Ar/^{39}Ar$, and Rb–Sr dates are discordant (70–126 Ma) due to the closure of the above isotopic systems at different temperatures; $^{87}Sr/^{86}Sr$ = 0.7056–0.7090 (Gamyanin et al., 2002, 2003). The pluton was emplaced and started to cool 126–121 Ma ago, and its evolution was completed 110 Ma ago as a result of slow cooling from 800 to 260°C with formation of Au–Mo–W mineralization hosted in plutonic rocks. Gold–quartz mineralization was formed at the late stage of the evo-

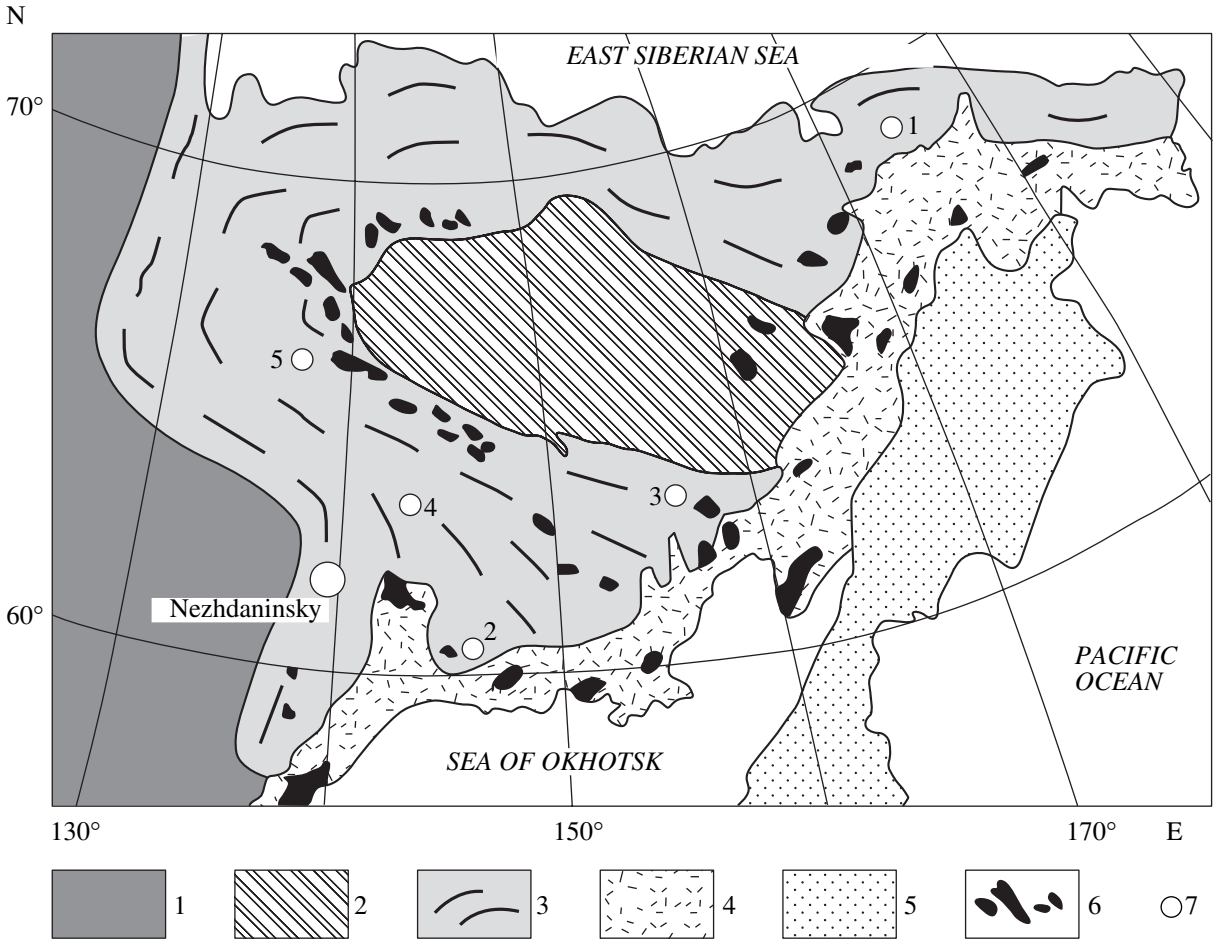

Fig. 1. Regional geological position of the Nezhdaninsky deposit in the northeast of Russia. (1) Siberian Platform, (2) Kolyma–Omolon Superterrane, (3) Mesozoic Verkhoyansk–Chukotka Fold System, (4) Okhotsk–Chukotka volcanic belt, (5) Cenozoic Foldbelt, (6) granitoid plutons, (7) large deposits (numerals in map): 1, Maisky (Au); 2, Natalka (Au); 3, Dukat (Ag); 4, Sarylakh (Sb–Au); 5, Sentachan (Sb–Au).

lution of the ore–magmatic system, and its lower age limit is 105–100 Ma (Bakharev et al., 2002).

The stocks of the Gel'dy group comprise 13 intrusive bodies small in size (50×100–700×1200 m^2) that crop out at the Gel'dy–Yaman interfluve (the left tributaries of the Tyry River in the south-southwest portion of the ore field). Some stocks consist of diorite and quartz diorite that grade into gabbrodiorite close to the contacts; others are completely composed of quartz diorite. K–Ar, Rb–Sr, and Ar/Ar ages of dioritic rocks and minerals therein vary from 105 to 80 Ma. The age of their emplacement and initial crystallization is estimated at 105–100 Ma; the younger ages (95–70 Ma) probably correspond to the closure of isotopic systems during the cooling (Gamyanin et al., 2003).

The dike suite consists of Late Jurassic gabbrodiorites and Cretaceous lamprophyres. The K–Ar age of the older dikes was estimated at 153, 154, and 168 Ma. It is suggested that biotite- and amphibole-bearing lamprophyres are genetically related to granitoids of the Kurum Complex (Gamyanin et al., 2003).

Hydrothermally Altered Rocks

Several stages of hydrothermal metasomatic alteration are recognized at the deposit: (1) autometasomatic propylitic, (2) preore sericite–carbonate, and (3) beresitic and albitic alterations and (4) sulfide disseminations in wall rocks. Propylites and preore sericite–carbonate metasomatic rocks are regionally abundant, whereas alterations (3) and (4) are related to orebodies in both time and space.

Propylitic alteration affected only dikes; the Late Jurassic gabbrodiorite dikes are altered more strongly than the younger lamprophyre dikes. Propylitic alteration corresponds to the low-temperature chlorite–calcite facies.

Quartz–carbonate–sericite alteration is controlled by faults. The assemblage of newly formed quartz, sericite, and Fe-carbonate fits the beresitic alteration type (Zharikov and Omel'yanenko, 1965; Zharikov, 1987). The altered halos near particular faults reach 100 m in width. In zones of closely spaced faults, these

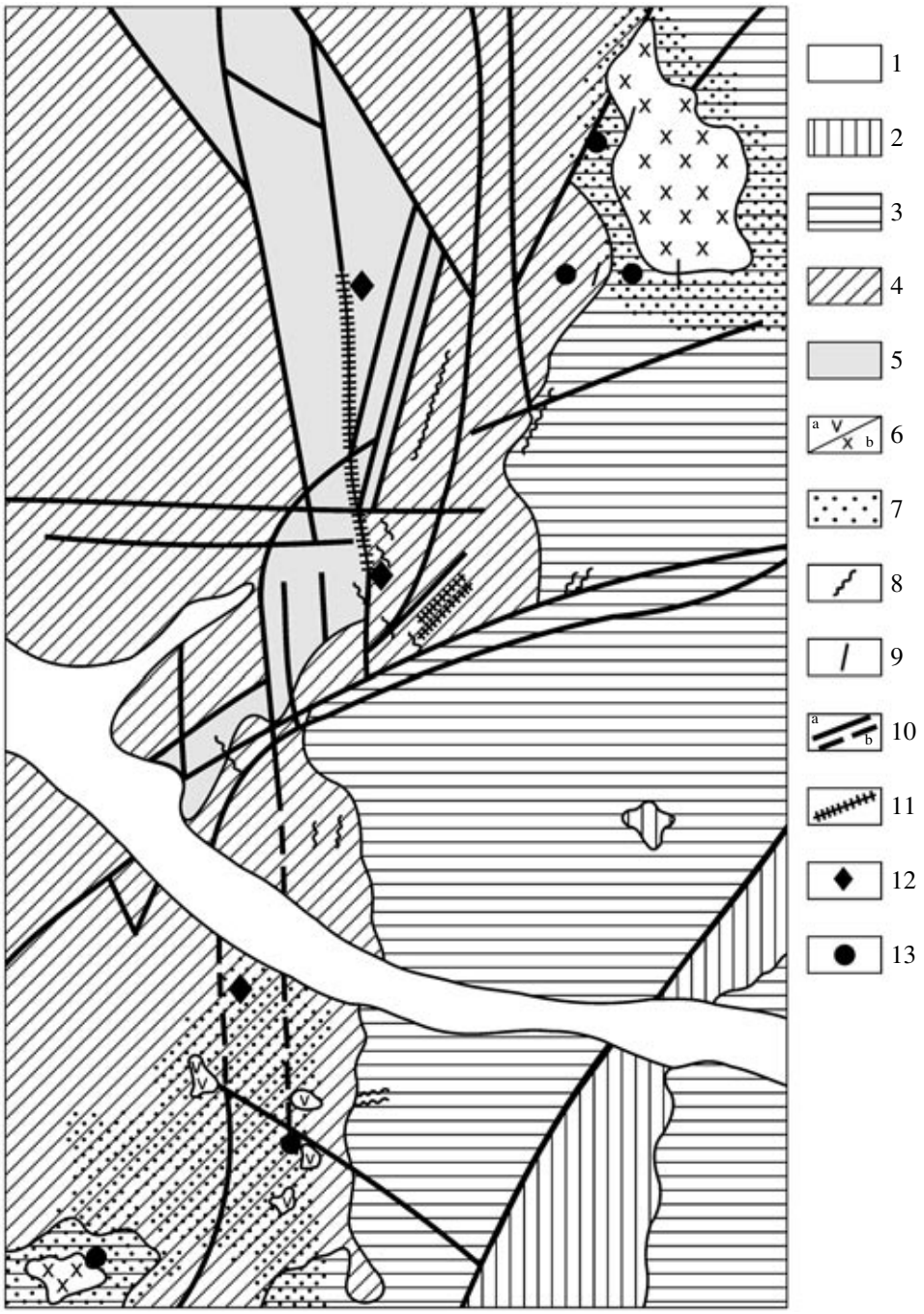

Fig. 2. Geological map of the Nezhdaninsky deposit. Compiled after G.F. Gurin, M.G. Afanas'ev, and others. (1) Quaternary sediments; (2–5) sandshale rocks of the Verkhoyansk Complex: (2) Lower and Middle Triassic sandstone and shale, (3) Upper Permian sandstone and siltstone, (4) Lower Permian shale and siltstone, (5) Lower Permian siltstone, shale, and sandstone; (6) intrusive rocks of (a) intermediate and (b) silicic compositions; (7) hornfels; (8) dikes of porphyritic diorite and lamprophyre; (9) aplite; (10) faults: (a) mapped and (b) inferred; (11) ore zone; (12) gold–quartz ore mineralization; (13) Au–Mo–W ore mineralization.

halos merge and their width increases by many times. The altered rocks of this type do not contain sulfide disseminations and are termed preore beresite.

Wide, steeply dipping tectonic zones trending in the near-meridional direction and, to a lesser extent, faults of other orientations control arsenopyrite–pyrite–quartz–carbonate–albite–sericite metasomatic alteration in the form of zonal infiltration halos reaching a few tens of meters in thickness near ore zones (Alpatov, 1998). Syngenetic sulfide disseminations (pyrite, arsenopyrite, and occasional pyrrhotite) in association with sericite and carbonate with a lower Fe/(Fe + Mg) ratio distinguish this metasomatic rock from preore beresite. The Fe/(Fe + Mg) ratio of newly formed carbonate and

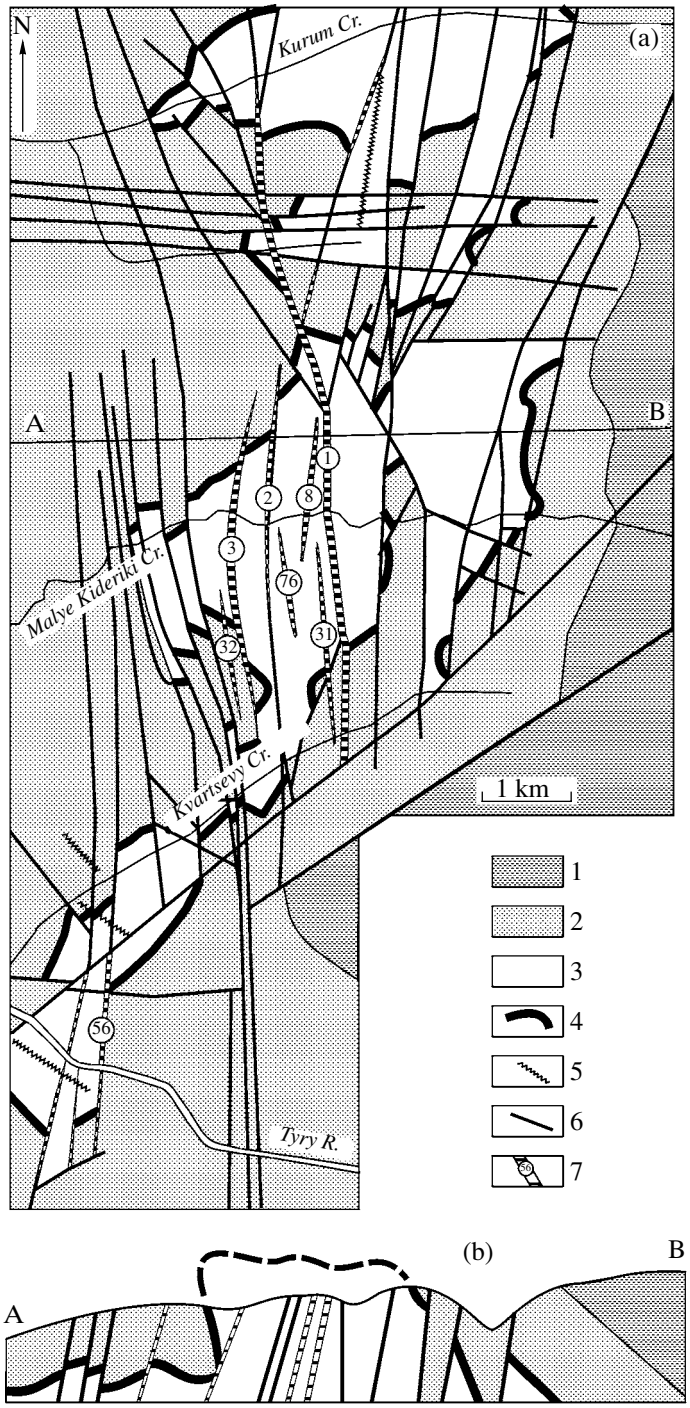

Fig. 3. (a) Geological sketch map and (b) section of the Nezhdaninsky ore field. (1) Upper Permian sandstone and siltstone; (2) Lower Permian sandstone, siltstone, and shale; (3) Lower Permian siltstone and sandstone; (4) Lower Permian reference sandstone bed; (5) dikes of porphyritic diorite and lamprophyre; (6) faults; (7) ore zone and its number.

sericite increases with the sulfide content in host rocks (Alpatov, 2003). Beresite and syngenetic disseminations of prismatic arsenopyrite are older than the productive milky white quartz. Beresitization and related sulfide mineralization do not intensify at contacts of these veins, which crosscut several zones of the metasomatic column and preore altered rocks unaffected by beresitization. Beresites in tectonic zones make up thick orebodies extended in the vertical and lateral directions. The main reserves of the deposits are contained in precisely these orebodies. The average Au grade of disseminated ore is 1–4 g/t. According to secondary ion mass spectroscopy results, the Au content in arsenopyrite varies from 1.17 to 386.64 ppm

(140.24 ppm, on average). The Au content in pyrite reaches 12.47 ppm (2.45 ppm, on average) (Bortnikov et al., 1993; Genkin et al., 1998).

Virtually monomineral albitic metasomatic rock, which, like beresite, is controlled by faults and related tension and shear fractures, was found near orebodies at deep levels of the deposit (Gamyanin et al., 2000). The thickness of albitic halos reaches a few tens of meters in particular sections. Albitic alteration affects siltstone, sandstone, and preore sericite–carbonate altered rock, whereas dikes remain unaltered.

Orebodies and Ore Mineralization

Gold–molybdenum–tungsten, gold–quartz, and silver–base-metal types of ore mineralization are known in the ore field.

Gold–molybdenum–tungsten mineralization predates the main gold–quartz mineralization and occupies a separate spatial position. Lenticular orebodies with Mo–W mineralization are localized in the contact zone of the Kurum granitoid pluton and near small outcrops of granitic rocks south of the Gel'dy group of stocks. The orebodies are composed of the following mineral assemblages (in order of their formation): (i) wall-rock molybdenite–(wolframite)–muscovite, (ii) quartz–pyrrhotite–loellingite–arsenopyrite, (iii) galena–sphalerite–chalcopyrite with scheelite, and (iv) gold–bismuthinite–sulfotelluride–bismuth. Joseite A and B, sporadic volynskite and maldonite grains, and subgraphic aggregates of native gold and bismuth have been identified in the latter assemblage. Native gold occurs as tiny inclusions in loellingite together with pyrrhotite and native bismuth disseminations. Gold is commonly intergrown with bismuthinite and joseite A and B, being localized along cleavage planes of these minerals. The native gold is 750–980 fine.

The gold–quartz ore and silver–base-metal mineralization are juxtaposed spatially. More than 50 orebodies known at the deposit are localized in steeply dipping faults that dissect the anticline's core, as well as in zones of fracturing, mylonitization, and cataclasis oriented in the near-meridional direction. The orebodies are subdivided into three morphological types: (i) mineralized fracture zones that consist of quartz–sulfide veinlets, sulfide disseminations in metasomatically altered rocks, and quartz–sulfide lenses (orebodies 1, 3, 31, and 56); (ii) concordant veins (orebody 8) and discordant sheetlike and lenticular veins (orebodies 5, 6, 14, and 21); and (iii) elongated stockwork zones (orebody 76). The main orebody (zone 1) extends for 10 km in the lateral direction and is traced down to a depth of 1.9 km without indications of pinching out. Its thickness varies from 2 to 40 m.

The orebodies were formed during gold-ore and silver–base-metal stages. The products of the gold-ore stage comprise scheelite–pyrite–arsenopyrite–ankerite–quartz, gold–chalcopyrite–galena–sphalerite, gold–sulfosalt–dolomite, and chalcostibnite–stibnite mineral assemblages.

The scheelite–pyrite–arsenopyrite–ankerite–quartz assemblage occupies about 95% of gold–quartz veins. Arsenopyrite is the predominant mineral in veins and stringer halos, where it was found in both veinlets and their thin metasomatic selvages. Pyrite is found in thin veinlets that occur in the outer portion of ore zones or adjoin quartz veins. Sporadic scheelite is observed in selvages of quartz veins and veinlets and less frequently in the veins themselves as fine disseminations and pockets up to 1–2 cm across. Small grains of native gold reach 0.16–0.25 mm in size, overgrowing sulfide grains or filling fractures therein. Having been formed later, this mineral overgrows arsenopyrite aggregates or fills interstitial spaces between pyrite and arsenopyrite grains.

The gold–chalcopyrite–galena–sphalerite assemblage postdated the scheelite–pyrite–arsenopyrite–ankerite–quartz assemblage, filling fractures in cataclastic pyrite and arsenopyrite grains and forming veinlets in quartz.

The gold–sulfosalt–dolomite assemblage includes a wide group of sulfoantimonites (bournonite, boulangerite, zinkenite, meneghinite) and fine-grained arsenopyrite and pyrite. The relatively late deposition of this assemblage is obvious because its veinlets cross sphalerite aggregates and replace galena. The overgrowing of sphalerite aggregates by pyrite and arsenopyrite metacrystals is typical as well. Fine-grained pyrite and arsenopyrite are confined to the same fractures as sulfosalt aggregates, indicating their simultaneous crystallization. Native gold crystallized together with sulfosalts in the same veinlets.

The chalcostibnite–stibnite assemblage completes the ore deposition at the gold-ore stage. Stibnite—the major mineral of this assemblage—is associated with less abundant chalcostibnite, famatinite, and berthierite.

The ore of the silver–base-metal stage consists of scheelite–pyrite–arsenopyrite–quartz, gold–base-metal–sulfosalt–carbonate, and hydromica–dickite assemblages.

The scheelite–pyrite–arsenopyrite–quartz assemblage was formed largely as a product of recrystallization of minerals belonging to the vein assemblage of the gold-ore stage. Quartz occurs as thin (up to a few centimeters) veins in quartz of the older assemblages and cements fragments of older quartz aggregates. Small (1–10 mm), perfectly faceted rock crystals that line the walls of cavities filled with segregations of redeposited acicular sulfosalts and small pyrite and cleiophane crystals also belong to this assemblage. Arsenopyrite and pyrite of this assemblage commonly reside in short tension and shear fractures and are spatially conjugated with segregations of older arsenopyrite and pyrite. Scheelite II formed at the silver–base-metal stage differs from scheelite I by its orange color.

The gold–base-metal–sulfosalt–carbonate assemblage contains freibergite, owyheeite, diaphorite, andorite,

and pyrargyrite. Sulfides and sulfosalts of this assemblage are enriched in silver and distinguished by a low As content; native gold shows the lowest fineness (<600). Carbonates differ from the replaced older carbonates by enrichment in Mn; kutnohorite appears occasionally. Newly formed manganosiderite has been identified.

The hydromica–dickite assemblage is the final one and, as a rule, fills vugs in regenerated quartz.

GEOCHEMISTRY OF TRACE ELEMENTS, INCLUDING REE

The distribution of trace elements has been studied in igneous and terrigenous host rocks within the ore field, in altered metasomatic rocks formed under compression and decompression, and in minerals crystallized at ore-forming stages. The REE contents were determined in preore carbonates, as well as in carbonates from veins of the gold-ore stage and the silver–base-metal stage (levels of +1230, 700, 670, 620, and 610 m) in ore zones 1, 3, 56, 60, and 76.

The analyses were performed with ICP MS on a VG Elemental PQ2 ICP MS spectrometer with an accuracy of 5–10%, as well as with the INAA and XRF methods, at laboratories of the Institute of Geology of Ore Deposits, Petrography, Mineralogy, and Geochemistry, Russian Academy of Sciences (RAS). REE contents were normalized to chondrite (Taylor and McLennan, 1985). The Eu/Eu* and Ce/Ce* chondrite-normalized values were calculated as $Eu/(Sm*(Tb*Eu)^{1/2})^{1/2}$ and Ce/((2La + Sm)/3), respectively.

Terrigenous Host Rocks

The terrigenous sequence is composed of siltstone, sandstone, and carbonaceous shale. The carbonaceous–calcareous siltstone consists largely of quartz and feldspar, with 2–3% carbonaceous matter and 5–10% carbonate matter. The carbonaceous matter is finely dispersed or segregated as tiny inclusions; laths of graphitized carbonic material are often observed. Sandstone consists of 80% quartz and sodic plagioclase grains 0.1–0.3 mm in size. Shale and carbonaceous shale contain as much as 20–30% carbonaceous matter, which is distributed nonuniformly as lenticular interlayers, clots, chains, and branching segregations.

The titanium module (TiO_2/Al_2O_3) of siltstone is close to the value typical of near-shore marine sediments deposited under conditions of an arid climate (Efremova and Stafeev, 1985). The sodic module (Na_2O/Al_2O_3) characterizes chemical weathering. It equals 0.11–0.13 in siltstone and is higher in sandstone, allowing the studied rocks to be classified as terrigenous. The potassic module (K_2O/Al_2O_3) is 0.16–0.19 and indicates an assemblage of hydromica + chlorite (± plagioclase). The total normative alkalinity, or feldspathic index ($(Na_2O + K_2O)/Al_2O_3$ = 0.29–0.31), fits rocks of normal alkalinity. The $(Fe_2O_3 + MgO)/TiO_2$, Ti/Zr, and La/Sc ratios of host rocks are intermediate between the values characteristic of terrigenous rocks at island arcs and passive continental margins (*Interpretation…*, 2001). The extremely low ratios Ti/Zr = 0.0015–0.0019 and Fe/Mn = 82–133 testify to a distal location of the shallow-water sedimentation basin relative to its provenance.

The unaltered siltstones and sandstones at a distance from faults are characterized by the following geochemical ratios: K/Rb = 313–411, K/Ba = 23–60, Ba/Rb = 4.1–9.2, K/Li = 525–4385, Li/Mg < 0.001–0.014, K/Cs = 5410–250 000, and Rb/Sr = 0.21–0.97 (Figs. 4, 5). The rocks are enriched in LREE (La_n/Yb_n = 7.60–11.33); both LREE and HREE, considered separately, are less fractionated (La_n/Sm_n = 2.59–3.64; Gd_n/Yb_n = 1.86–3.16) (Table 1). Siltstone reveals a negative Eu anomaly (Eu/Eu* = 0.79–0.89). A positive Ce anomaly (Ce/Ce* = 1.17–1.31) is a result of sorption of the oxidized species of this element.

Granitoids of the Kurum Pluton

Fine- and medium-grained hornblende–biotite granodiorite consists (vol %) of plagioclase (38–59), alkali feldspar (13–10), quartz (12–36), amphibole (3–4), and biotite (7–10). In chemical composition, granodiorite is transitional between rocks of normal alkalinity and subalkaline rocks and between metaaluminous and moderately aluminous rocks (ASI = 0.896–1.05); f = Fe/(Fe + Mg) = 57–72%; $f_{ox} = Fe_2O_3/(Fe_2O_3 + FeO)$ = 0.16–0.60; K appreciably prevails over Na; the rock is diopside-normative.

Leucogranite consists of plagioclase (12–35 mol % An), low orthoclase and microcline (up to 20 mol % Ab), and biotite. The rock is high-K, moderately aluminous (ASI = 0.975–1.048), high-Fe (f = 74–86%), and highly oxidized (f_{ox} = 0.50–0.60); the rock is corundum-normative.

Granodiorite contains hornblende with f = 54–57% and biotite with f = 60–64%, while biotite from leucogranite is characterized by f = 94%. Accessory minerals in granodiorite include allanite, ilmenite, titanite, zircon, and apatite. Both granodiorite and leucogranite contain sporadic resorbed grains of pyralspite garnet of two generations. The first generation resembles garnet from the Precambrian metamorphic rocks of the Okhotsk Massif (Grinberg, 1968). According to experimental data (Green, 1977), garnet of the second generation could be a product of magma crystallization at 500–600 MPa pressure, i.e., at a depth of 15–18 km (Gamyanin et al., 2003). Titanite and ilmenite contents in leucogranite are much lower than in granodiorite, but the rock is relatively enriched in high-Fe (f = 95–98%) almandine with 18–38 mol % spessartine; monazite appears as an accessory mineral.

Granitoids of the Kurum pluton are correlated with calc-alkaline series of the granodiorite–granite plutonic association (Gamyanin et al., 2000), which may be con-

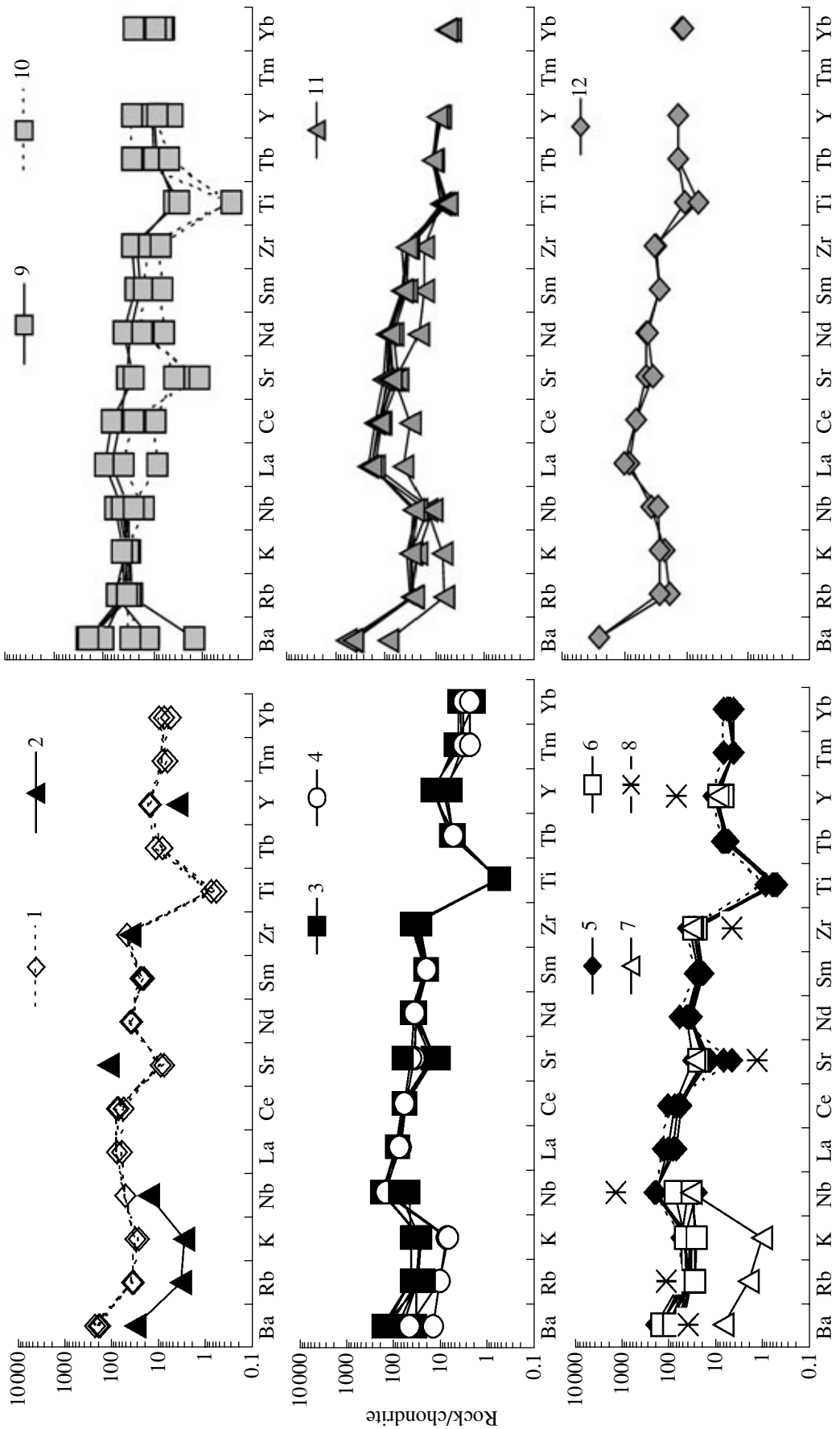

Fig. 4. Spidergrams of igneous, terrigenous, and metasomatic rocks in the Nezhdaninsky ore field. (1, 2) Terrigenous rocks: (1) siltstone, (2) sandstone; (3–8) metasomatic rocks: (3) preore, (4) albitic, replacing (5) siltstone, (6) lamprophyre, (7) sandstone, and (8) diorite; (9–12) igneous rocks: (9) granitoids, (10) aplitic veins and dikes in the Kurum pluton, (11) dikes in the Nezhdaninsky ore field, (12) Gel'dy stocks.

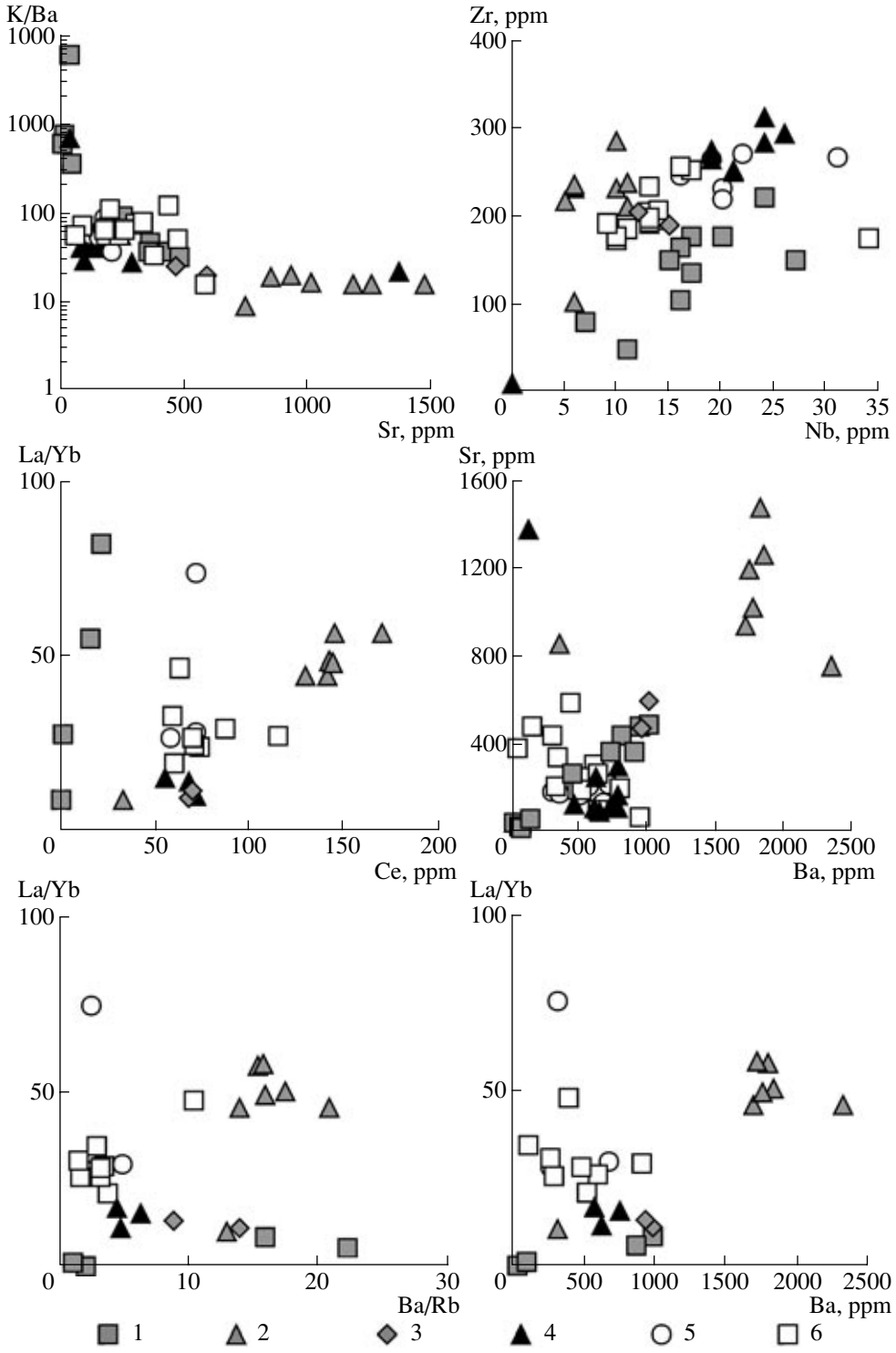

Fig. 5. Trace elements and their ratios in igneous, terrigenous, and metasomatic rocks in the Nezhdaninsky ore field. (1) Granitoids of the Kurum pluton, (2) dikes in the Nezhdaninsky ore field, (3) Gel'dy stocks, (4) host terrigenous rocks, (5) preore metasomatic rocks, (6) ore-bearing metasomatic rocks.

sidered as a derivative of orogenic andesites (Fershtater et al., 1984). In chemical composition, granodiorite corresponds to I-type granitoids, while leucogranite bears attributes of S- or A-granite. Granodiorite was formed at an active continental margin during the late orogenic stage of tectonic evolution, while leucogranite corresponds to collision-related granites with some indications of within-plate rocks.

Table 1. REE distribution in metasomatic rocks of the Nezhdaninsky deposit, ppm

No.	La	Ce	Pr	Nd	Sm	Eu	Gd	Tb	Dy	Ho	Er	Tm	Yb	Lu	Total	Eu/Eu*	Ce/Ce*	La_n/Yb_n	La_n/Sm_n	Gd_n/Yb_n
Siltstone																				
1	22.5	55.8	6.39	26.4	5.45	1.08	5.23	0.51	2.58	0.49	1.31	0.3	1.34	0.21	129.5	0.79	1.20	11.33	2.59	3.16
2	29.4	68.9	7.36	28.0	5.66	1.28	5.69	0.5	3.29	0.59	1.71	0.29	1.91	0.28	154.8	0.89	1.17	10.39	3.27	2.41
3	28.1	72.6	7.71	27.7	4.86	1.22	5.75	0.7	3.32	0.77	1.79	0.23	2.5	0.28	157.6	0.85	1.31	7.60	3.64	1.86
Preore beresite replacing siltstone																				
4	30.4	59.3	6.93	25.5	4.9	0.86	3.08	0.33	1.84	0.33	0.97	0.14	1.09	0.18	135.9	0.78	0.99	18.85	3.91	2.29
5	34.5	72.3	8.64	33.1	5.88	1.1	3.97	0.42	2.09	0.36	1.14	0.16	1.17	0.19	165.0	0.81	1.06	19.93	3.69	2.75
6	36	72.3	8.18	30.3	5.28	0.94	3.47	0.42	2.21	0.42	1.17	0.19	0.48	0.22	161.6	0.76	1.03	50.68	4.29	5.86
Ore-bearing beresitized siltstone																				
7	36	74.7	9.01	33.8	6.1	1.1	3.6	0.44	2.51	0.43	1.29	0.18	1.41	0.21	170.8	0.79	1.05	17.25	3.71	2.07
8	59.6	116.2	13.5	48.8	7.9	1.3	4.72	0.52	2.82	0.56	1.62	0.28	2.07	0.37	260.3	0.75	1.01	19.46	4.75	1.85
9	29.6	60.6	7.25	27.1	4.94	0.98	3.24	0.42	2.12	0.42	1.25	0.18	1.43	0.22	139.8	0.81	1.04	13.99	3.77	1.84
10	35.2	71.8	8.3	30.2	5.17	1.02	3.33	0.4	2.23	0.43	1.22	0.18	1.36	0.24	161.1	0.83	1.05	17.49	4.29	1.98
11	45.9	88.2	10	36	6.27	1.31	4.05	0.47	2.39	0.43	1.23	0.18	1.5	0.21	198.1	0.87	1.00	20.68	4.61	2.19
12	35.1	70.2	8.08	30	5.29	0.93	3.3	0.37	1.98	0.38	1.03	0.17	1.25	0.19	158.3	0.78	1.03	18.98	4.18	2.14
Albitic metasomatic rock replacing siltstone																				
13	29.9	60.2	7.13	26.2	4.9	0.96	3.17	0.36	1.78	0.32	0.82	0.13	0.87	0.12	136.9	0.83	1.02	23.22	3.84	2.95
14	31.6	64.1	7.54	28.3	5.12	0.91	3.11	0.34	1.62	0.27	0.74	0.09	0.66	0.12	144.5	0.79	1.03	32.35	3.88	3.82

Note: (4, 5, 7–10) Metasomatic rocks formed under compression; (6, 11–14) metasomatic rocks formed under extension.

In granodiorite, leucogranite, and aplitic veins from the central portion of the Kurum pluton and in a dike of aplite-like leucogranite from the contact zone, Na, Rb, and Cs contents increase from older rocks to younger, while Mg, Li, and Sr contents decrease in the same direction (Table 2; Figs. 4, 5). The K/Rb ratio changes insignificantly (314–396 in granodiorite, 298–338 in leucogranite, 384 in aplite veins, and 209 in aplite-like leucogranite). The K/Ba, Rb/Sr, and Li/Mg ratios increase in younger rocks, varying from 38–39, 0.22–0.24, and 0.003–0.004, respectively, in granodiorite to 50–95, 0.38–0.57, and 0.005–0.006 in leucogranite; 6400, 2.17, and 0.042 in aplitic veins; and 820, 7.83, and 0.083 in the dike of aplite-like leucogranite. The K/Ba ratio is comparable with the values within the range 20–60 typical of Phanerozoic basic, intermediate, and silicic igneous rocks and their Archean equivalents (Kerrich and Fryer, 1988). The K/Li ratio in granodiorite and leucogranite is 1204–1241 and 1492–3123, respectively. The younger granitic rocks crystallized from melts depleted in Sr owing to the preceding crystallization of plagioclase (Antipin et al., 1984).

Thus, the variation in the contents of components and their ratios are caused by crystal fractionation with enrichment in Li, Rb, Cs, and Ga and depletion in Ba and Sr. The decreasing K/Rb and K/Cs ratios are a distinct indication of the fractionation (Antipin et al., 1984; Kerrich and Fryer, 1988). The K/Li, K/Tl, Ba/Rb, and Rb/Cs ratios decrease, while the K/Ba, Rb/Sr, and Li/Mg ratios increase (Kerrich, 1989). Our estimates are close to or higher than the values reported for granodiorite and granite (Condie, 1981) and are much higher than the mean crustal values (Taylor and McLennan, 1985).

In discriminant diagrams (Pearce et al., 1984; Pike et al., 2002; Velikoslavinsky, 2003), the compositions of granitoids from the Kurum pluton fall into the field of granites from volcanic arcs (Fig. 6a) or the field of granites from volcanic arcs and syncollision granites (Fig. 6b), while the composition of aplite-like leucogranite falls into the field of within-plate granites (Figs. 6a, 6b). These compositional variations might be caused by a different degree of fractionation (Galley, 2003); however, spidergrams indicate that a difference in the source is crucial. Granitoids of the Kurum pluton are enriched in Rb, Y, and Nb and depleted in Sr and Ba (aplitic varieties) relative to subduction-related granitoids (Pearce et al., 1984; Velikoslavinsky, 2003). The highly evolved granitic rocks from the central portion of the pluton are enriched in Nb and characterized by a lower K/Rb ratio; they are also enriched in incompatible Rb, Cs, Y, and Pb and depleted in compatible Ba, Sr, Co, Ni, and V. Aplite-like granite and aplite enriched in silica are products of either advanced crystal fraction-

Table 2. Distribution of lithophile elements in igneous rocks and their minerals in the Nezhdaninsky ore field

No.	Na	K	Li	Cs	Mg	Sc	V	Co	Ni	Rb	Sr	Y	Zr	Nb	Ba	K/Rb	K/Ba	K/Cs	Ba/Rb	Rb/Sr
Plagioclase																				
1	4.76	0.47	0.00018	0.00046	0.063	65	535	74	0	31	0	0	35	7	224	152	21	1022	7.23	
2	6.49	0.67	0.00065	0.0004	0.16	4	1	0	4	32	756	0	84	0	206	209	33	1675	6.44	0.04
3	5.48	0.31	0.0015	0.00056	0.0054	0	0	0	9	20	16	0	84	1	0	155		554	0.00	1.25
Potassium feldspar																				
4	1.3	12.2	0.00018	0.00063	0.049	3	0	0	6	220	294	0	24	1	1472	555	83	19365	6.69	0.75
5	1.38	11.58	0.00021	0.00061	0.021	3	0	0	11	230	196	0	35	0	1260	503	92	18984	5.48	1.17
6	1.4	12.37	0.0003	0.00067	0.042	5	0	0	10	284	88	0	21	0	424	436	292	18463	1.49	3.23
7	2.22	10.34	0.00086	0.0023	0.013	4	0	0	7	551	19	0	59	0	28	188	3693	4496	0.05	29.00
8	2.41	10.34	0.00034	0.0011	0.045	5	0	0	9	250	0	0	26	1	130	414	795	9400	0.52	
Kurum pluton																				
9	2.88	3.6	0.0029	0.00025	0.77	5	62	11	10	111	481	22	178	17	932	324	39	14400	8.40	0.23
10	2.88	3.01	0.0025	0.00041	0.76	9	61	15	14	111	436	11	164	16	794	271	38	7341	7.15	0.25
11	2.46	3.27			0.75	6	47	11	9	120	487	26	149	15	995	273	33		8.29	0.25
12	2.69	3.40			0.49	4	29	8	10	163	363	29	178	20	890	209	38		5.46	0.45
13	2.69	4.06	0.0013	0.00025	0.23	0	8	0	13	166	262	27	151	27	426	245	95	16240	2.57	0.63
14	2.94	3.58	0.0024	0.00061	0.49	13	44	4	8	159	368	26	221	24	714	225	50	5869	4.49	0.43
15	3.06	3.77	0.002	0.00093	0.024	0	0	0	8	247	21	75	136	17	46	153	820	4054	0.19	11.76
16	2.61	3.21			0.06	2	2	5	7	230	17	72	80	7	51	140	629		0.22	13.53
17	2.88	3.84	0.0011	0.00025	0.026	1	0	0	6	133	43	35	105	16	6	289	6400	15360	0.05	3.09
18	2.52	4.47			0.05	3	0	6	6	145	54	23	47	11	117	308	382		0.81	2.69
Dikes in the Nezhdaninsky ore field																				
19	1.97	0.67			4.33	29	217	25	14	25	854	21	102	6	330	268	20		13.20	0.03
20	1.60	2.97			3.14	14	154	19	37	116	1475	20	236	6	1811	256	16		15.61	0.08
21	1.98	3.00			2.47	21	119	16	33	104	1263	21	211	11	1846	288	16		17.75	0.08
22	1.44	2.89			3.35	19	137	18	45	108	1191	22	231	10	1729	268	17		16.01	0.09
23	1.77	2.19			2.23	17	116	16	32	111	753	20	217	5	2339	197	9		21.07	0.15
24	1.88	3.52			2.97	20	129	19	38	119	937	18	286	10	1701	296	21		14.29	0.13
25	2.11	3.06			2.82	15	129	14	34	109	1023	22	238	11	1764	281	17		16.18	0.11
Gel'dy stocks																				
26	2.33	2.06			1.69	8	117	15	12	70	598	34	189	15	999	294	21		14.27	0.12
27	1.87	2.55			1.66	23	110	15	19	103	472	34	204	12	947	258	25		10.12	0.11

Note: (1, 27) Quartz diorite; (2, 5, 12) adamellite; (3, 7, 15, 16) aplite-like leucogranite (dikes); (4, 9–11) granodiorite; (6) leucogranite; (8, 17, 18) aplite from vein in the central portion of the pluton; (19, 26) gabbrodiorite; (20–23) porphyritic diorite; (24, 25) lamprophyre. Na, K, Li, Cs, and Mg contents are given in wt % and other elements, in ppm.

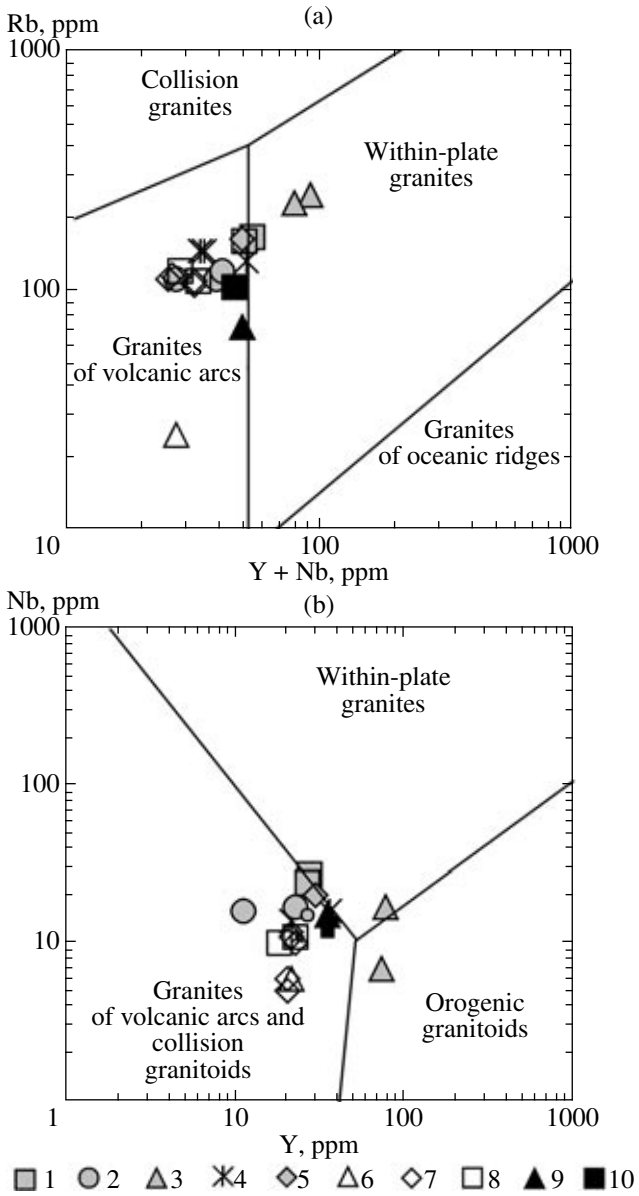

Fig. 6. Chemical compositions of igneous rocks in the Nezhdaninsky ore field plotted on (a) Rb–(Y + Nb) and (b) Nb–Y discriminant diagrams. (1–5) Kurum pluton: (1) granite in central portion of the pluton, (2) granodiorite, (3) aplite-like granite, (4) aplite veins in granite, (5) adamellite; (6, 7) dikes in the Nezhdaninsky ore field: (6) gabbrodiorite, (7) porphyritic diorite; (8) lamprophyre; (9, 10) Gel'dy stocks: (9) gabbrodiorite, (10) quartz diorite.

ation or a lower degree of partial melting in comparison with granodiorite and granite (Kovalenko et al., 2003).

The trace element contents in feldspars from granodiorite and garnite of the Kurum pluton and quartz diorite of the Gel'dy stock are different. Plagioclase is commonly depleted in trace elements relative to the coexisting melt except Sr and Eu and, in some cases, Ba, Zn, and Pb (Nash and Crecraft, 1985). The increase in Ab content in alkali feldspar from transitional orthoclase (14.8–15.3 mol % Ab) in granodiorite to low orthoclase and nonlattice microcline in leucogranite (up to 20 mol % Ab) is accompanied by decreasing K/Rb, Rb/Sr, Ba/Rb, and K/Cs ratios and increasing K/Ba and Li/Mg ratios (Table 2). The Sr partition coefficient does not depend on the proportions of Ab and Or end members (Larsen, 2002), while the Ba and Rb partition coefficients are partly controlled by the amount of K. Because Ba concentrates largely in alkali feldspar of intermediate rocks, the alkali feldspar from the evolved rocks is depleted in Ba (Kerrich and Fryer, 1988). Thus, alkali feldspar in younger granitic rocks accumulates Rb, Li, and Cs and is depleted in Ba, Sr, and Mg, as is typical of evolved rocks. Crystallization of biotite depletes a melt in Ba, while crystallization of plagioclase diminishes Sr content. Alkali feldspar extracts both components from a melt (Antipin et al., 1984), whereas Rb and Pb are left in the residual liquid (Larsen, 2002). The Ba/Rb ratio in alkali feldspar increases with pressure and may serve as an indicator of crystallization depth.

The highest REE contents were detected in granodiorite and adamellite (120.29–170.54 ppm) (Table 3). Enrichment in LREE is typical (La_n/Yb_n = 10.92–15.24); no Ce anomalies were detected. An insignificant negative Eu anomaly was revealed in adamellite (Eu/Eu* = 0.71). The REE content in aplitic rocks is much lower. The REE total in aplite-like granite is 76.34 ppm, and the chondrite-normalized REE pattern is even (La_n/Yb_n = 1.62); the Eu minimum is very deep (Eu/Eu* = 0.06), and a distinct negative Ce anomaly is observed (Ce/Ce* = 0.80) (Fig. 7). The REE content in aplite veins is still lower (24.06 ppm); a slight enrichment in HREE (La_n/Yb_n = 0.92), a deep Eu minimum, and an insignificant positive Ce anomaly are revealed (Fig. 7).

Gel'dy Stocks

The Gel'dy stocks are composed of diorite and quartz diorite grading into gabbrodiorite in contact zones. Diorite and quartz diorite are composed of zonal plagioclase (from An 70–80 mol % in cores to An 20–39 mol % at margins), ortho- and clinopyroxene (hypersthene and less abundant bronzite and augite), biotite, and high and transitional orthoclase. The plagioclase composition in quartz diorite varies from An 50 mol % to An 20 mol %; transitional orthoclase, clinopyroxene (from diopside–augite to subcalcic augite and ferroaugite), hornblende, and biotite are other major minerals.

In their chemical composition, the dioritic rocks of the Gel'dy group of stocks occupy a transitional position between rocks of normal alkalinity and subalkaline rocks and belong to the high-K calc-alkaline series.

The trace element distribution in dioritic rocks is shown in Tables 2 and 3 and Figs. 4 and 5. These rocks are characterized by the following LILE ratios: K/Rb =

Table 3. REE distribution in igneous rocks of the Nezhdaninsky ore field, ppm (INAA results)

No.	Rock	La	Ce	Nd	Sm	Eu	Tb	Yb	Lu	Total	Eu/Eu*	Ce/Ce*	La_n/Yb_n	La_n/Sm_n
							Kurum pluton							
1	Granodiorite	30.2	56.1	24.7	5.13	1.43	0.59	1.9	0.24	120.3	0.97	0.94	10.92	3.71
2	Adamellite	43.2	83.1	33.9	6.25	1.14	0.68	1.9	0.29	170.5	0.71	0.99	15.24	4.35
3	Aplite-like granite	17.5	29.3	15.0	4.51	0.05	1.97	7.3	0.78	76.3	0.06	0.80	1.62	2.44
4	Aplite	3.6	10.2	5.0	1.79	0.09	0.33	2.6	0.43	24.1	0.24	1.17	0.92	1.25
							Dikes							
5	Gabbrodiorite	17.4	33.4	16.9	4.40	1.52	0.68	1.7	0.26	76.3	1.06	0.92	6.89	2.49
6	Porphyritic diorite	91.9	170.8	73.4	12.54	3.05	0.77	1.6	0.19	354.3	1.02	0.96	38.94	4.61
7	″	79.0	143.3	69.3	11.05	2.61	0.75	1.6	0.20	307.8	0.98	0.94	33.93	4.50
8	″	79.3	146.0	66.7	11.14	2.56	0.71	1.4	0.22	308.0	0.97	0.95	39.21	4.48
9	″	70.1	130.2	55.9	9.36	2.29	0.68	1.5	0.20	270.3	0.99	0.97	30.86	4.72
10	Lamprophyre	77.2	141.8	66.6	10.48	2.44	0.81	1.7	0.18	301.2	0.93	0.95	30.87	4.63
11	″	79.2	144.9	64.3	10.84	2.59	0.76	1.6	0.21	304.3	0.98	0.95	33.30	4.60
							Gel'dy stocks							
12	Gabbrodiorite	34.6	68.5	34.5	7.07	2.09	0.87	3.2	0.44	151.3	0.99	0.98	7.33	3.08
13	Quartz diorite	40.0	70.7	32.7	6.72	1.82	0.88	3.1	0.41	156.3	0.92	0.90	8.83	3.75

258–294, K/Ba = 21–25, Ba/Rb = 10–14, and Rb/Sr = 0.1; in discriminant diagrams, the rock compositions fall into the field of volcanic arcs (Fig. 6). Gabbrodiorite and quartz diorite contain 151.28 and 156.29 ppm REE total, respectively. Enrichment in LREE is typical (La_n/Yb_n = 7.33–8.83).

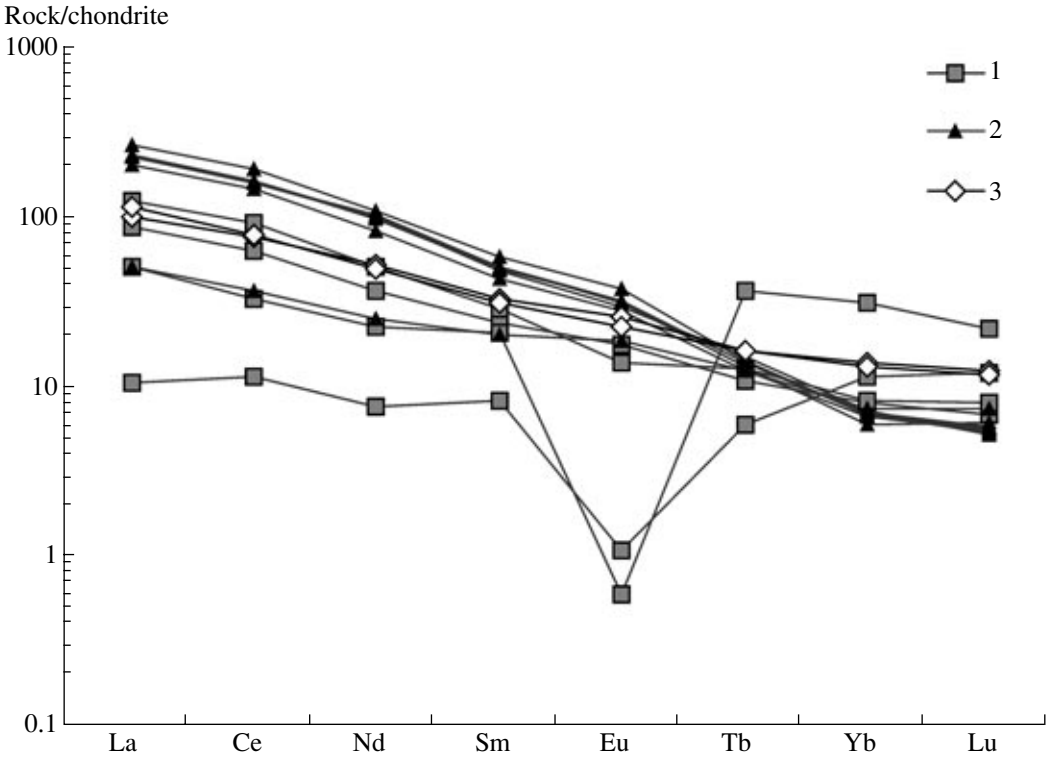

Fig. 7. Chondrite-normalized REE patterns of igneous rocks in the Nezhdaninsky ore field. (1) Granitoids of the Kurum pluton, (2) dikes in the Nezhdaninsky ore field, (3) Gel'dy stocks.

Rocks of the Dike Suite

Gabbrodiorite from the Late Jurassic dikes is characterized by a wide variation in mineral composition (vol %): plagioclase, 52–82; clinopyroxene, 6–10; amphibole, 0–12; and quartz, 3–7; ilmenite, apatite, zircon, pyrrhotite, pyrite, and hematite are accessory minerals; Cr-spinel and garnet are exceptionally rare. In chemical composition, this rock belongs to the calc-alkaline series of elevated alkalinity with a prevalence of Na over K.

Amphibole lamprophyre consists of plagioclase, alkali feldspar, hornblende, quartz, and biotite. The assortment of accessory minerals—ilmenite, apatite, zircon, and titanite—is similar to that of granodiorite in the Kurum pluton, testifying to their cognation, which is emphasized by the occurrence of resorbed pyralspite garnet grains in both rocks. Garnet crystallized at a depth that corresponds to a pressure of 5–6 kbar (Bakharev and Zaitsev, 2000; Bakharev et al., 2002).

The trace element contents in dikes of the Nezhdaninsky ore field are presented in Tables 2 and 3. As can been seen from spidergrams (Figs. 4, 5), the distribution of all elements is rather uniform except for a gabbrodiorite dike that is distinguished by low Ba, Rb, K, Zr, and LREE contents. The LILE ratios are as follows: K/Rb = 197–296, K/Ba = 9–21, Ba/Rb = 13–21, and Rb/Sr = 0.03–0.15. In discriminant diagrams, the compositions of dikes fall into the field of granite from volcanic arcs (Fig. 6). All studied dikes are enriched in LREE (La_n/Yb_n = 30.87–39.21; 6.89 in the gabbrodiorite dike) (Fig. 7). The REE total is 270.32–354.26 ppm (76.3 ppm in gabbrodiorite); Eu and Ce anomalies are absent (Eu/Eu* = 0.93–1.06 and Ce/Ce* = 0.92–0.97).

Metasomatic Rocks

The halo of preore beresite is zonal. In the outer zone, chlorite is replaced with sericite–phengite and Fe-carbonates of the siderite–magnesite and ankerite–dolomite series. As a result, a quartz + chlorite + albite + sericite + Fe-carbonate (pistomesite ± ankerite) mineral assemblage was formed. In the inner zone, chlorite is replaced completely with formation of a quartz + albite + sericite + Fe-carbonate (pistomesite ± ankerite) mineral assemblage. Beresitization in the outer and inner zones results in replacement of albite with quartz, sericite, and carbonate from grain margins to their cores. The amount of newly formed minerals in rock increases from 0–5 vol % in the outer zone to 20–25 vol % in the inner zone. The alteration is accompanied by a gain in Ca, Mg, and CO_2 (and also K in siltstone) and an insignificant loss of Na.

The LILE ratios in preore beresite are as follows: K/Rb = 359–378, K/Ba = 55–75, Ba/Rb = 3.4–4.1, K/Li = 1076–3950, Li/Mg = 0.001–0.003, K/Cs = 3950–6897, and Rb/Sr = 0.56–1.00 (Table 4). In ore-bearing metasomatic rocks, these ratios are K/Rb = 275–380, K/Ba = 35–83, Ba/Rb = 2.8–4.2, K/Li = 707–5193, Li/Mg < 0.001–0.002, K/Cs = 3649–99 000, and Rb/Sr = 0.27–1.09 (Figs. 4, 5). These ratios are higher than the mean crustal estimates (numerals in parentheses) published by Taylor and McLennan (1985) for K/Rb (285), K/Ba (36), K/Li (700), and Rb/Sr (0.12) and lower than those for Ba/Rb (7.8) and K/Cs (9130 for three-fourths of analyses). The K, Rb, and Cs contents are much higher than average crustal values except for metasomatically altered sandstone, where Cs has not been detected. The Li and Sr contents are either below or above the global crustal averages. The K/Rb ratio of altered rocks corresponds to the main trend of igneous rocks (MT) (Shaw, 1968) (Fig. 8) and approaches the pegmatitic–hydrothermal trend and the composition of orthomagmatic fluid of Mo–W greisen (McCuaig and Kerrich, 1998).

It is evident that the behavior of lithophile elements during alteration of terrigenous rocks is accompanied by an increase in the K/Rb and Rb/Sr ratios and a decrease in the Li/Mg ratio from sandstone to lamprophyre and further to siltstone protoliths (Table 4). The K/Ba ratio increases from sandstone and siltstone protoliths to lamprophyre. The K/Cs ratio decreases in the same direction. Thus, in the course of the hydrothermal process, the K/Ba ratio increases and the Ba/Rb and K/Cs ratios decrease owing to a gain in K, Rb, and Cs and depletion in Ba and Sr. The K/Rb, K/Li, and Rb/Sr ratios do not vary so distinctly. The K–Rb and K–Cs pairs show a strong positive correlation.

A typical halo of ore-bearing beresitic alteration is built as follows: (i) a protolith (preore beresite) composed of quartz, sericite, carbonate, and albite; (ii) an outer zone consisting of quartz, sericite, carbonate, albite, and pyrite; and (iii) an inner zone made up of quartz, sericite, carbonate, pyrite, and arsenopyrite.

The occurrence of syngenetic sulfide disseminations (pyrite, arsenopyrite, and occasional pyrrhotite) in association with low-Fe sericite and carbonate that replace Fe-bearing phengite and Fe-carbonates of preore beresite is the main distinguishing feature of ore-bearing beresite and related metasomatic rocks. The Fe/(Fe + Mg) ratios of the newly formed carbonate and sericite decrease with an increase in the sulfide content in host rocks (Alpatov, 2003).

The reaction that describes ore-bearing beresitization implies replacement of feldspars, mainly albite, with sericite and quartz:

$$3\text{Albite} + K^+ + 2H^+ = \text{Sericite} + 6\text{Quartz (or } H_4SiO_4) + 3Na^+.$$

Depending on whether silica precipitates as quartz or is removed partly or completely, the difference between the volumes of the newly formed and replaced phases varies from 8 to 53%. The reaction of albite replacement with sericite and quartz is always accompanied by a decrease in the volume of the newly formed phases, so that an increase in pressure promotes the proceeding of this reaction and an increase in quartz solubility. Albite is replaced with sericite and quartz in

Table 4. Chemical composition of host rocks and metasomatic rocks at the Nezhdaninsky deposit

No.	Na	K	Li	Cs	Mg	Sc	V	Co	Ni	Rb	Sr	Y	Zr	Nb	Ba	As	K/Rb	K/Ba	K/Cs	Ba/Rb	Rb/Sr
Host rocks																					
1	1.56	2.72	n.a.	n.a.	0.97	10	182	12	39	124	91	37	265	19	637	8	219	43		5.14	1.36
2	1.74	2.32	″	″	0.89	9	138	11	32	116	106	35	275	19	763	30	200	30		6.58	1.09
3	1.59	2.71	″	″	0.97	13	143	18	39	125	109	38	273	19	591	64	217	46		4.73	1.15
4	2.75	2.23	0.00091	0.00023	0.66	6	104	6	14	90	299	32	293	26	770	70	248	29	9696	8.56	0.30
5	0.97	3.99	0.00091	0.00061	1	13	213	13	31	155	115	36	253	21	714	215	257	56	6541	4.61	1.35
6	1.85	3.3	0.0017	0.00061	0.88	15	212	14	38	140	165	35	284	24	772	124	236	43	5410	5.51	0.85
7	2.59	3.59	0.0046	0.00064	1.54	16	121	18	20	147	250	38	251	21	602	40	244	60	5609	4.10	0.59
8	2.74	2.1	0.004	0.00029	0.29	11	151	12	32	91	128	36	313	24	438	166	231	48	7241	4.81	0.71
9	3.33	0.25	0.00016	<0.00004	1.94	14	65	11	22	12	1378	9	231	6	110	296	208	23		9.17	0.01
Preore beresite																					
10	1.23	4.16	0.0022	0.00068	1.08	13	220	4	23	164	208	35	231	20	556	9009	254	75	6118	3.39	0.79
11	0.06	3.95	0.001	0.001	1.15	13	212	16	36	171	134	33	264	19	652	913	231	61	3950	3.81	1.28
12	1.99	2.69	0.0025	0.00039	1	8	194	11	46	118	163	41	267	31	486	54	228	55	6897	4.12	0.72
13	n.a.	n.a.	n.a.	n.a.	n.a.	9	122	8	37	85	849	14	165	24	685	306				8.06	0.10
14	1.81	2.45	″	″	″	12	142	12	25	121	178	34	245	16	339	163	202	72		2.80	0.68
15	1.75	2.58	″	″	″	10	138	11	32	122	184	40	219	20	279	81	211	92		2.29	0.66
16	1.67	2.69	″	″	″	11	124	12	38	133	213	38	271	22	695	42	202	39		5.23	0.62
Ore-bearing metasomatic rocks																					
17	0.07	3.49	n.a.	n.a.	n.a.	9	176	10	25	151	204	26	191	13	305	19850	231	114		2.02	0.74
18	0.11	5.56	″	″	″	16	250	31	57	241	63	31	257	16	928	1796	231	60		3.85	3.83
19	0.02	3.25	″	″	″	12	156	17	26	132	246	23	172	10	537	26084	246	61		4.07	0.54
20	0.00	4.16	″	″	″	16	214	14	28	179	265	29	194	13	619	4787	232	67		3.46	0.68
21	0.00	3.42	″	″	″	6	135	11	25	139	188	26	198	13	498	26652	246	69		3.58	0.74
22	0.00	3.6	″	″	″	11	148	6	20	162	440	24	234	13	287	3948	222	125		1.77	0.37
23	1.23	2.79	0.0008	0.00057	0.96	11	172	9	29	117	191	25	204	13	476	499	238	59	4895	4.07	0.61
24	0.076	4.56	0.0021	0.0009	0.91	20	241	21	22	148	99	19	186	11	620	100318	308	74	5067	4.19	1.49
25	n.a.	n.a.	n.a.	n.a.	n.a.	9	224	8	25	195	219	30	201	12	604	22945				3.10	0.89
26	0.056	5.27	0.0024	0.0013	0.97	18	265	5	24	220	197	25	253	17	782	1234	240	67	4054	3.55	1.12
27	0.098	4.57	0.00088	0.0011	1.22	8	152	0	27	179	310	18	175	34	590	583	255	77	4155	3.30	0.58
28	1.49	2.7	0.0026	0.00074	2.33	9	135	4	32	114	342	23	196	14	324	179	237	83	3649	2.84	0.33
29	4.86	0.099	0.00014	<0.00004	0.49	4	46	0	19	8	384	24	207	14	28	37	124	35		3.50	0.02
30	n.a.	n.a.	n.a.	n.a.	n.a.	10	133	21	78	110	482	19	179	30	597	161	0	0		5.43	0.23
31	4.50	0.7	″	″	″	15	134	31	37	40	482	18	177	10	132	23452	175	53		3.30	0.08
32	4.24	0.68	″	″	″	7	123	23	35	39	590	22	192	9	415	29868	174	16		10.64	0.07

Note: (1–6) Siltstone; (7, 8) hornfels; (9) sandstone; (10–16) preore beresite; (17–32) ore-bearing metasomatic rocks replacing (17–26) siltstone, (27, 28) lamprophyre, (29) sandstone, (30) diorite, and (31, 32) albitic metasomatic rock; n.a., not analyzed. Al, Ti, Na, K, Li, Cs, and Mg contents are given in wt % and other elements, in ppm.

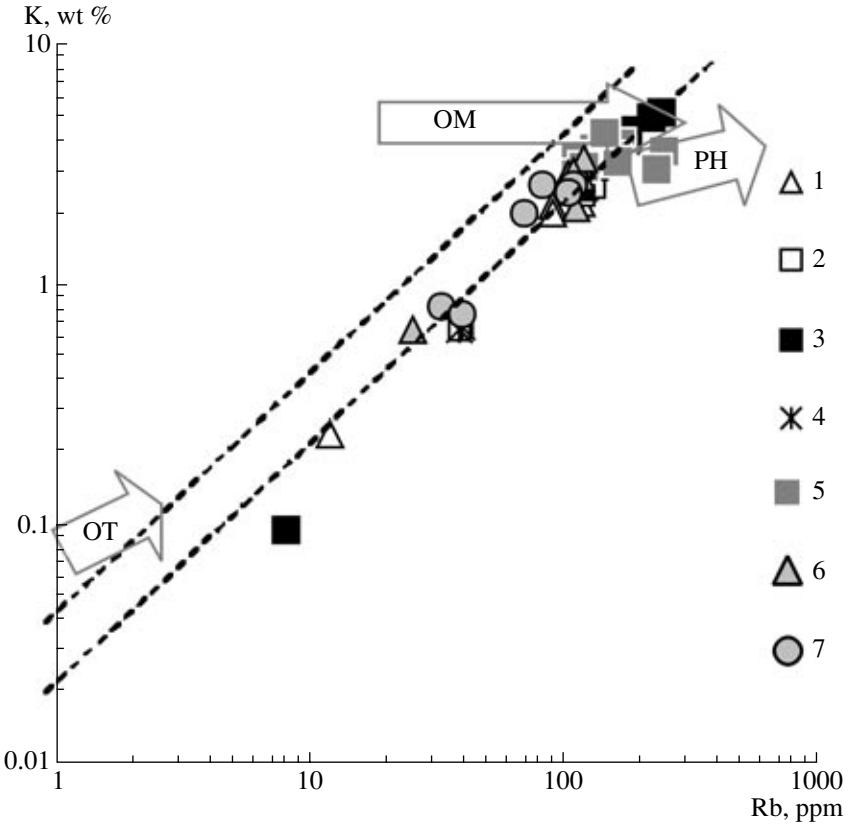

Fig. 8. K and Rb in igneous, terrigenous, and metasomatic rocks in the Nezhdaninsky ore field. MT, main trend of igneous rocks; OT, oceanic tholeiites; PH, pegmatite–hydrothermal trend; OM, orthomagmatic Mo–W greisen (Shaw, 1968; Kerrich, 1989; McCuaig and Kerrich, 1998). (1) Host terrigenous rocks; (2–4) metasomatic rocks: (2) preore, (3) ore-bearing, (4) wall-rock; (5) granitoids of the Kurum pluton; (6) dikes of the Nezhdaninsky ore field; (7) Gel'dy stocks.

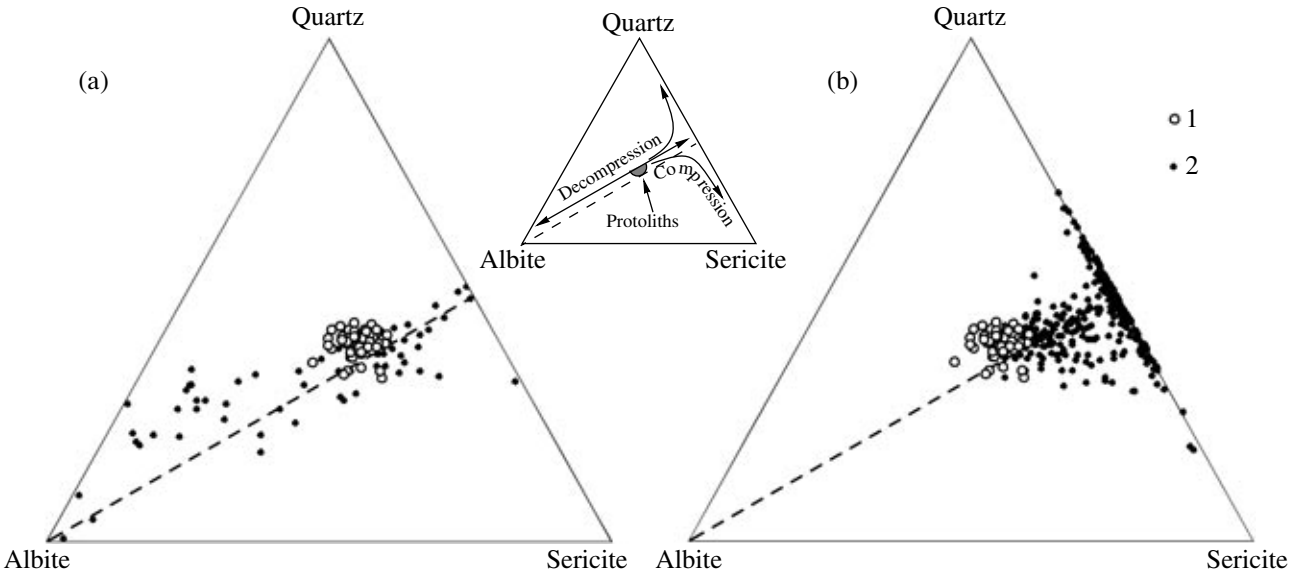

Fig. 9. Quartz, albite, and sericite in metasomatic rocks formed under conditions of (a) decompression and (b) compression. (1) Preore metasomatic rocks (protoliths), (2) ore-bearing metasomatic rocks. The dashed line corresponds to the reaction 3Albite = Sericite + 6Quartz.

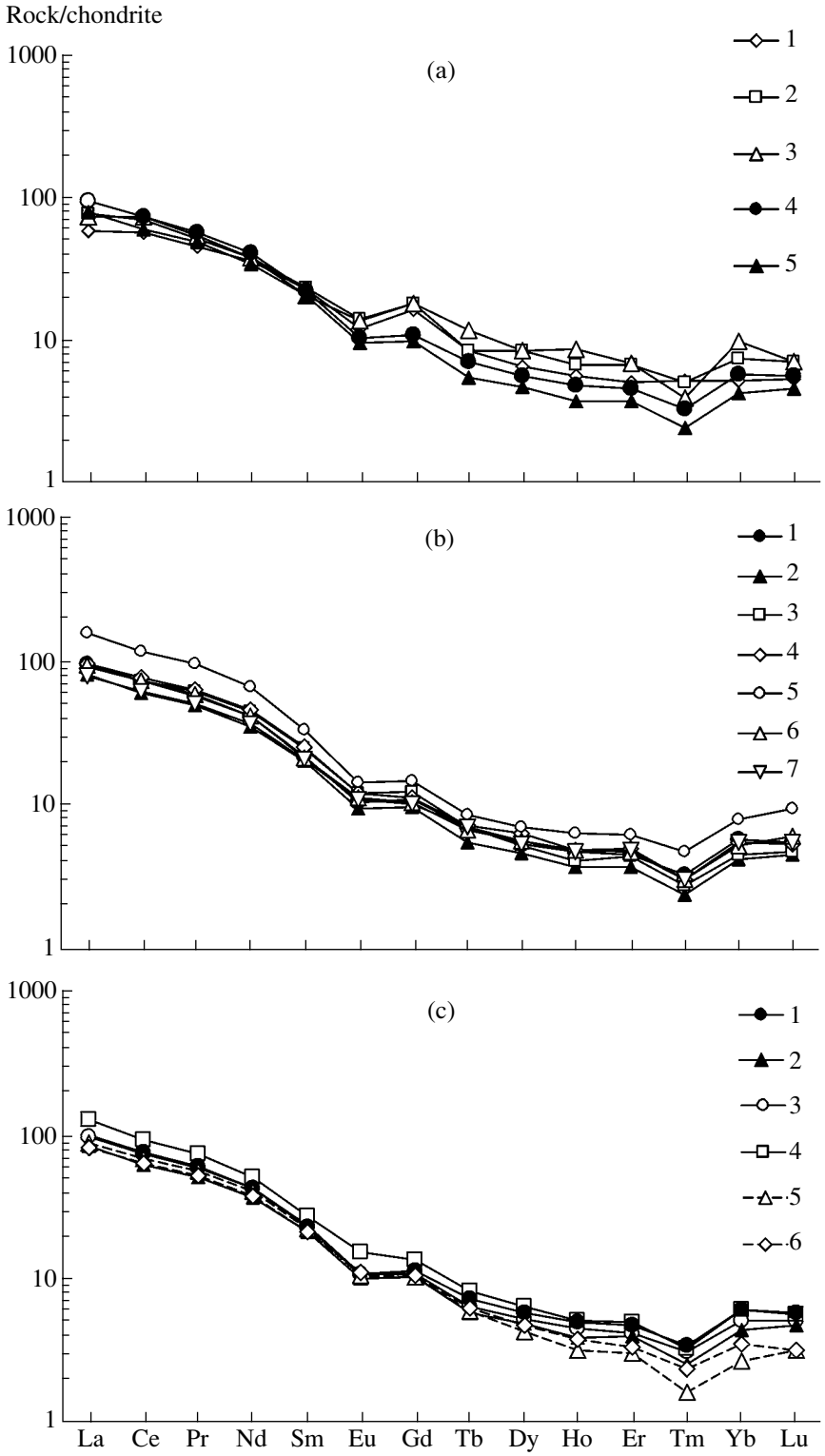

Fig. 10. Chondrite-normalized REE patterns of rocks at the Nezhdaninsky deposit. (a) (1–3) Metamorphic rocks and (4, 5) preore metasomatic rocks; (b) (1, 2) preore beresite and (3–7) ore-bearing metasomatic rocks from compression zones; (c) (1, 2) preore beresite and (3–6) ore-bearing metasomatic rocks from decompression zones.

zones of moderate compression, where monolithic rocks with sporadic slickensides along cleavage fractures are predominant. In zones of high pressure, i.e., along tectonic sutures composed of fine-grained mylonites, substantially sericitic metasomatic rocks (70–75 vol % sericite) are formed. This implies that, while

Table 5. REE distribution in carbonates at the Nezhdaninsky deposit, ppm

No.	Ore zone	La	Ce	Pr	Nd	Sm	Eu	Gd	Tb	Dy	Ho	Er	Tm	Yb	Lu	Total	Eu/Eu*	Ce/Ce*	La_n/Yb_n	La_n/Sm_n	Gd_n/Yb_n
Stage of preore beresitization																					
1	60	13.2	34.8	4.88	21.9	7	3.96	6.04	0.93	5.22	0.9	2.44	0.32	2.33	0.32	104	1.59	1.07	3.83	1.19	2.10
Gold-ore stage																					
2	1	6.34	11.7	1.17	4.3	1.07	0.44	1.25	0.22	1.25	0.26	0.75	0.1	0.59	0.09	29.5	1.12	0.94	7.26	3.73	1.72
3	1	3.65	11.1	1.55	6.86	2.02	1.73	2.49	0.45	2.95	0.55	1.41	0.18	1.13	0.16	36.2	1.91	1.22	2.18	1.14	1.79
4	1	0.75	3.31	0.63	3.27	1.62	0.82	2.14	0.39	2.59	0.5	1.41	0.18	1.32	0.18	19.1	1.26	0.93	0.38	0.29	1.31
5	3	0.13	0.31	0.05	0.28	0.24	0.12	0.79	0.2	1.55	0.33	0.91	0.13	0.82	0.09	6.0	0.92	0.56	0.11	0.34	0.78
6	56	0.38	2.01	0.53	3.75	3.17	0.83	3.14	0.45	2.08	0.32	0.74	0.11	0.71	0.1	18.3	0.88	0.40	0.36	0.08	3.58
7	56	0.46	2.04	0.42	2.39	1.46	0.63	1.96	0.29	1.74	0.29	0.75	0.1	0.63	0.09	13.3	1.17	0.72	0.49	0.20	2.52
8	56	0.68	2.58	0.53	2.92	1.99	1.12	2.93	0.41	1.83	0.29	0.74	0.08	0.56	0.09	16.8	1.42	0.66	0.82	0.22	4.24
Silver–base-metal stage																					
9	76	0.96	2.13	0.3	1.65	0.98	0.46	1.6	0.26	1.16	0.2	0.52	0.06	0.4	0.07	10.8	1.16	0.70	1.62	0.62	3.24
10	3	0.58	3.57	1.04	6.55	3.52	1.1	3.95	0.68	3.85	0.66	1.72	0.2	1.28	0.17	28.9	0.93	0.61	0.31	0.10	2.50

albite is replaced with sericite, silica is released and removed partly or completely from the zones of reaction to areas of decompression (Fig. 9).

Decompression developed in zones of brecciation, in siltstones and sandstones, and in dikes that were emplaced near zones of ductile deformation or updip from these zones. Furthermore, fractures locally opened within zones of ductile deformation close to strike-slip and pull-apart dislocations. As a result, ore microveinlets syngenetic to ore-bearing beresites were formed in these zones and half-opened fractures. The total volume of ore veinlets amounts to hundredths of percent to 1–2% of the volume of host metasomatic rocks. Silica removed from strained zones precipitated in open fissures along with carbonates and sulfides. The formation of ore-bearing beresite, in particular, quartz–sericite metasomatic rocks at upper levels of orebodies, continued simultaneously.

In zones where ore-bearing beresite was formed under compression, this metasomatic rock is enriched in V, Ti, Al, Ga, K, Rb, and HREE; thereby, the K/Rb and La/Y ratios increase from 202–212 to 231–246 and from 0.76–0.90 to 1.21–1.92, respectively, whereas the Nb, Y, and Zr contents and the Zr/Nd ratio drop (from 8.19–8.59 to 5.27–6.42) (Tables 1, 4; Figs. 4, 5, 10). The highest Al, Ti, Ga, V, K, Rb, Nd, and La contents and REE total, as well as elevated Rb/Sr and La_n/Sm_n ratios (3.83 and 4.8, respectively) and the lowest Sr and Eu/Eu* = 0.75, were detected in sample 1/6-29-IVa of beresite replacing intensely foliated siltstone from a tectonic suture zone.

Beresite that was formed under conditions of decompression has insignificantly higher K, Rb, Sr, Nd, and HREE contents and Eu/Eu* ratio relative to preore beresite, whereas Y, Zr, and Nb contents decrease (Tables 1, 4; Figs. 4, 5, 10). The newly formed rock is characterized by elevated K/Rb and La/Y ratios (from 202 to 222–246 and from 1.06 to 1.44–1.77, respectively) and lowered Zr/Nd and La_n/Yb_n ratios (from 8.09 to 5.5–7.8 and from 50.68 to 18.98–20.68, respectively).

Hence, the ore-bearing fluid was enriched in V, Ti, Al, Ga, K, Rb, and HREE in comparison with the replaced rocks and the fluid bringing about preore alteration of host rocks; the Zr/Nd and La_n/Yb_n values were lower.

The albitic metasomatic rocks formed under conditions of decompression are characterized by the following zoning: (i) a protolith (preore beresite) consisting of quartz, carbonate, sericite, and albite; (ii) an outer zone (albitized rock) with quartz, carbonate, sericite, albite, and pyrite ± pyrrhotite; and (iii) an inner zone composed of quartz, carbonate, albite, arsenopyrite, and pyrite ± pyrrhotite. The mechanism of albitic alteration may be suggested to be as follows. The replacement of albite with sericite gave rise to the enrichment of fluid in Na. As a result, a reverse reaction of replacement of sericite with albite became possible at more heated lower levels. The conditions of decompression were preferable for this process because the volume of newly formed minerals was larger than the volume of replaced minerals. The change in volume was due to the porosity of rocks in the outer halo of ore-bearing beresite. However, the small pores rapidly became plugged and limited albite formation in monolithic host rocks. Intense albitization developed in zones of microbrecciated sandstone, where sericite could be completely replaced with albite, and, to a lesser extent, in siltstone.

Albitic metasomatic rock reveals the lowest K, Rb, Nb, and Y contents and the highest Sr content and is enriched in LREE (Table 1, 4; Figs. 4, 5, 10).

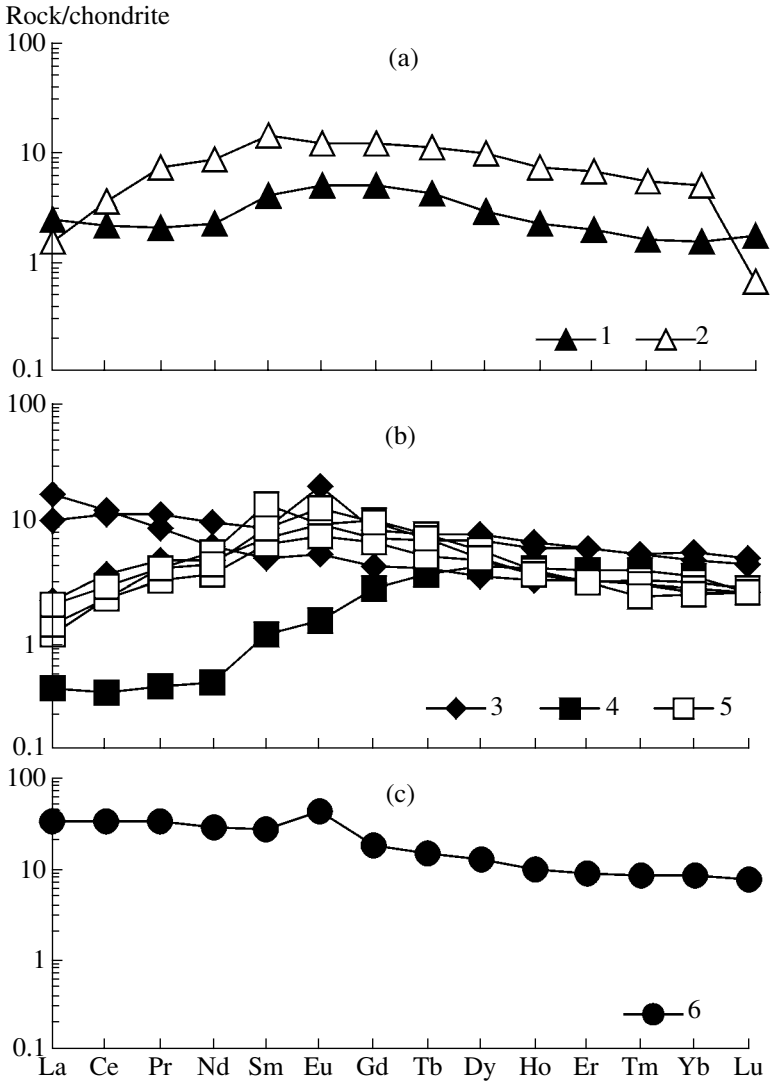

Fig. 11. Chondrite-normalized REE patterns of carbonates from the Nezhdaninsky deposit. Carbonates: (a) regenerated, (b) synore, (c) preore. Ore zones: (1) 76, (2) 3, (3) 1, (4) 3, (5) 56, (6) 60.

Thus, the metasomatic alteration of host rocks results in their enrichment in LILE and HREE and their depletion in HFSE irrespective of the formation conditions. The ore-bearing metasomatic rock formed under conditions of compression is additionally enriched in V, Ti, Al, and Ga in contrast to the rock formed under conditions of decompression, enriched in Sr and Nd and having a higher Eu/Eu*. All metasomatic rocks are enriched in LREE, and their Eu/Eu* and Ce/Ce* ratios are close to unity. This implies that a relatively oxidized fluid participated in metasomatism. The highest La_n/Yb_n = 50.7 was established in preore beresite. The maximum La_n/Sm_n = 4.8 was detected in altered rock from a tectonic suture zone, and the highest Gd_n/Yb_n = 5.9, in preore beresite.

REE Patterns in Minerals from Veins

Preore carbonates are characterized by a high REE total, enriched in LREE (La_n/Yb_n = 3.8, La_n/Sm_n = 1.2, Gd_n/Yb_n = 2.1), and marked by a positive Eu anomaly (Eu/Eu* = 1.6), as shown in Table 5. The highest REE total was detected in ankerite from preore carbonate veinlets in beresite (104.2 ppm). The REE patterns of various generations of carbonates are shown in Fig. 11.

Carbonates that crystallized at the gold-ore stage occur in quartz veins (the ankerite–dolomite series) and stockwork halos (the siderite–magnesite series). In quartz veins, carbonates make up pocketlike segregations up to 1–2 cm in size, commonly near vein selvages. The Fe mole fraction (f' = Fe/(Fe + Mg + Mn), at %) of carbonates pertaining to this assemblage is 0.10–0.35.

The REE total in carbonates precipitated at the gold-ore stage varies from 6.0 to 36.2 ppm (Table 5): 19.1–36.2 ppm in ore zone 1 (+1230 m), 6.0 ppm in ore zone 3 (+700 m), and 13.2–18.3 ppm in ore zone 56 (+620 m). Carbonates from ore zone 1 are enriched in LREE (La_n/Yb_n = 0.4–7.3, La_n/Sm_n = 0.3–3.7, Gd_n/Yb_n =

Table 6. Chemical composition of scheelite from the Nezhdaninsky deposit

Component	Scheelite I			Scheelite II		
	6/6-29	NB-1	6/29	2/21	3/13v	13/6-29
CaO, wt %	18.03	17.94	18.31	18.94	19.62	19.44
SrO	0.69	0.91	0.78	1.82	2.03	1.54
WO_3	80.48	80.85	80.39	79.08	78.81	79.34
Total	99.20	99.70	99.48	99.84	100.46	100.32
La, ppm	129	152	71.4	2.18	1.05	3.53
Ce	348	461	272	6.53	3.39	5.39
Pr	46.7	66.7	48.7	1.25	0.69	0.65
Nd	184	282	242	7.2	4.15	2.37
Sm	54.6	86.2	85.5	5.07	3.07	0.98
Eu	390	343	173	20.1	11.1	44.5
Gd	53.1	95.4	98.4	5.81	3.62	1.25
Tb	7.98	14.6	13.4	0.79	0.48	0.19
Dy	43.8	81.6	65.9	3.4	2.06	1.32
Ho	7.06	13	8.9	0.45	0.26	0.2
Er	17.4	28.6	15.9	0.92	0.58	0.46
Tm	2.14	2.96	1.15	0.11	0.06	0.06
Yb	11.64	13.5	4.09	0.59	0.3	0.26
Lu	1.25	1.23	0.32	0.05	0.03	0.03
Total REE	1296.67	1641.79	1100.66	54.45	30.84	61.19
Eu/Eu*	10.40	6.47	3.97	6.58	6.14	38.81
Ce/Ce*	1.16	1.20	1.12	0.61	0.56	0.72
La_n/Yb_n	7.49	7.61	11.80	2.50	2.37	9.17
La_n/Sm_n	1.49	1.11	0.53	0.27	0.22	2.27
Gd_n/Yb_n	3.70	5.73	19.50	7.98	9.78	3.90

1.3–1.8); carbonates from ore zone 3, in HREE ($La_n/Yb_n = 0.1$, $La_n/Sm_n = 0.3$, $Gd_n/Yb_n = 0.8$); and carbonates from ore zone 56, in MREE ($La_n/Yb_n = 0.4$–0.8, $La_n/Sm_n = 0.1$–0.2, $Gd_n/Yb_n = 2.5$–4.2). The latter are characterized by an insignificant positive Eu anomaly (Eu/Eu* = 1.2–1.4).

Carbonates of the silver–base-metal stage fill vugs in quartz and contain 10.8–28.9 REE in total (Table 5). They are characterized by a convex REE pattern owing to enrichment in MREE ($La_n/Yb_n = 0.3$–1.6, $La_n/Sm_n = 0.1$–0.6, $Gd_n/Yb_n = 2.5$–3.2), as shown in Fig. 11.

Hence, the REE total and LREE contents decrease in the younger carbonates in comparison with the older generations. Variations in REE patterns of carbonates pertaining to the gold-ore stage are probably caused by the composition of the respective mineral assemblage and/or the composition of the carbonate itself. Preore carbonate corresponds to ankerite in composition; dolomite is typical of the gold-ore stage, and the siderite–magnesite series, of the silver–base-metal stage. In ionic radius, Ca (1.06 Å) is close to MREE (from 1.22 to 0.99 Å) and may be replaced with both LREE and HREE; Fe^{2+} (0.82 Å) is replaced with HREE, whereas Mg is not replaced isomorphically with REE at all (Semenov, 2001). Thus, LREE first enter the lattices of calcite and dolomite, and HREE, those of magnesite and siderite (Bau and Möller, 1992).

Scheelite formed during the gold-ore stage occurs as fine disseminations and pockets up to 1–2 cm in size in selvages of quartz veins and veinlets in close association with ankerite and is less abundant in axial parts of veins near arsenopyrite segregations that overgrow this mineral. Scheelite I contains 1101–1642 ppm REE in total (Table 6) and is enriched in LREE ($La_n/Yb_n = 7.5$–11.8). A positive Eu anomaly (Eu/Eu* = 4.0–10.4) and an insignificant Ce anomaly (Ce/Ce* = 1.1–1.2) are revealed (Fig. 12).

Scheelite II crystallized during the silver–base-metal stage. The REE total in this mineral (30.8–61.2 ppm) is much lower than in scheelite I (Table 6); $La_n/Yb_n = 2.4$–9.2 (Fig. 12). A positive Eu anomaly (Eu/Eu* = 6.2–38.8) and a negative Ce anomaly (Ce/Ce* = 0.6–0.7) are typical (Fig. 12).

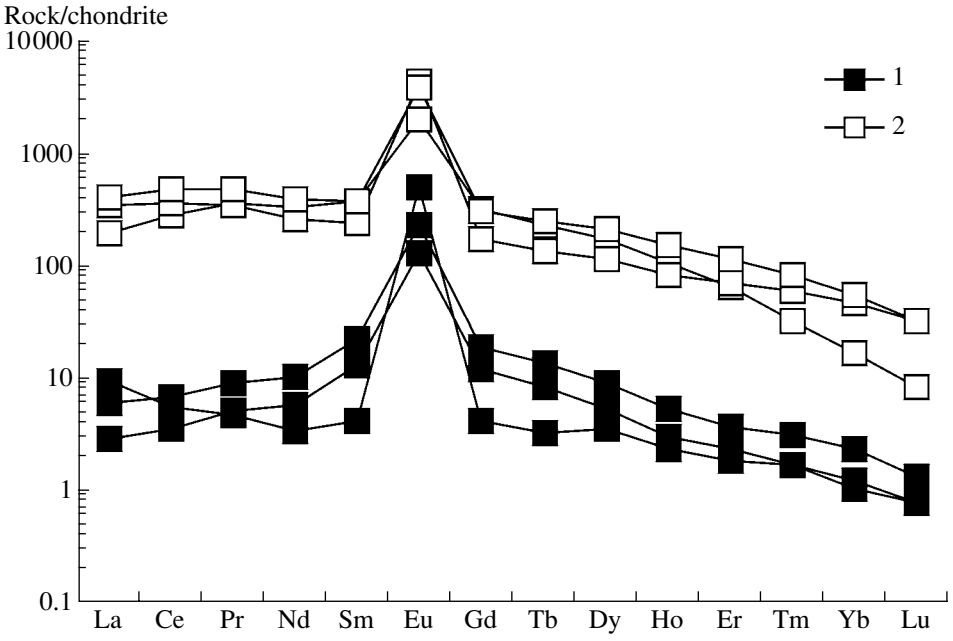

Fig. 12. Chondrite-normalized REE patterns of scheelite from the Nezhdaninsky deposit. (1) Scheelite I, (2) scheelite II.

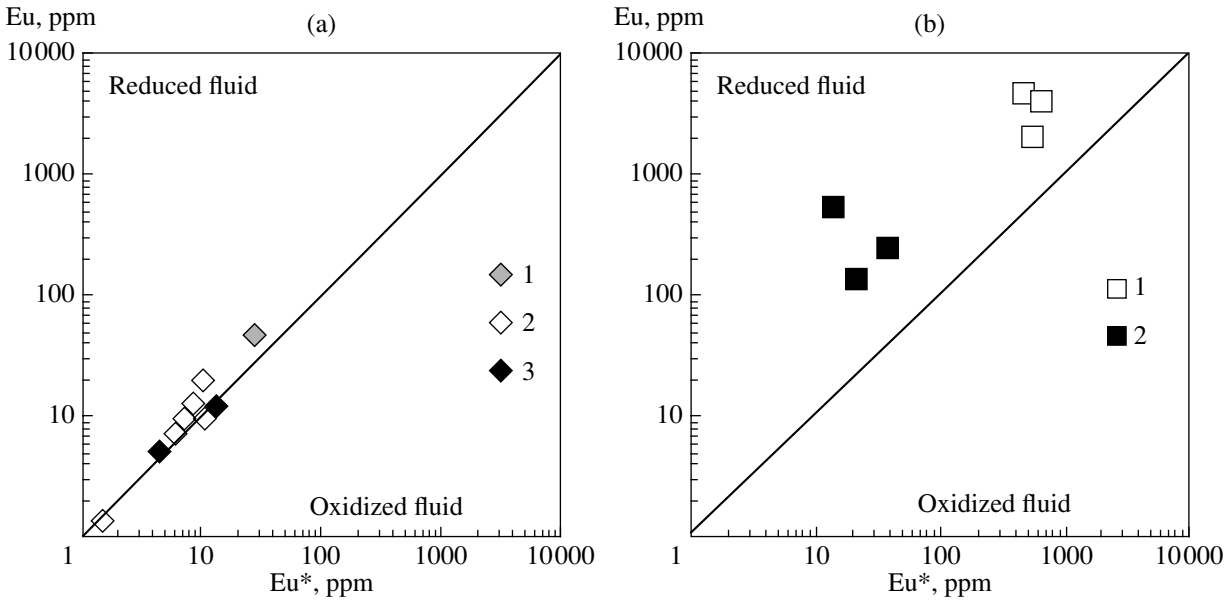

Fig. 13. Eu versus Eu* in the fluid coexisting with carbonates and scheelite at the Nezhdaninsky deposit. (a) Carbonates: (1) preore, (2) synore, (3) regenerated; (b) scheelite: (1) first generation, (2) second generation.

Thus, scheelite crystallized from REE-enriched fluid with La/Yb > 1. REE enter the scheelite lattice as $3Ca^{2+} = 2REE^{3+} + \square_{Ca}$ (Ghaderi et al., 1999). The high Eu/Eu* of scheelite indicates that Eu occurred in fluid as Eu^{2+}, and this implies that scheelite crystallized from a reduced fluid at a temperature above 250°C, as demonstrated by a high positive Eu anomaly (Eu/Eu* = 38.8) in scheelite II from sample 13/6-29 (Fig. 13). Variations in REE patterns of scheelite grains belonging to the same generation (a convex pattern with Gd/Yb > La/Yb and a flat pattern with Gd/Yb < La/Yb) probably depend on the fluid composition and the REE speciation. As has been shown from experimental results, the enrichment of fluid in alkali metals leads to replacement of Ca contained in scheelite with these metals. In this case, the partition coefficient for MREE is higher than for LREE and HREE, which is reflected in a convex shape of the REE pattern. The total charge is balanced by Na. In the

absence of alkali metals, the charge is balanced by a Ca vacancy, as expressed in a flat REE pattern.

FLUID INCLUSIONS

Fluid inclusions were studied in quartz from (i) zones of Au–Mo–W mineralization near the contact of the Kurum pluton, including quartz cores of aplite veins grading into ore-bearing veinlets, pegmatoid veins, and quartz–pyrrhotite veins with arsenopyrite; (ii) milky white quartz from various veins and different depth levels; and (iii) regenerated quartz (rock crystals) formed during the silver–base-metal stage (Table 7).

Research Methods

Microthermometry of fluid inclusions was performed on a THMSG-600 microscope heating stage (Linkam, United Kingdom) that allows measurements within a temperature range from –196 to +600°C. This heating stage is used in most laboratories worldwide for the study of fluid inclusions. The stage provides a stable temperature regime and high accuracy (±0.1°C) and reproducibility and is convenient to use. The accuracy of measurement of the phase transition temperature was controlled by periodic study of reference inclusions. Water in the liquid phase of the studied samples was determined by the increase in volume of the frozen liquid. In the course of cooling, ice was identified by the temperature coefficient of dissolution and optical properties (Borisenko, 1977; Roedder, 1984). Sodium chloride (halite) was identified by the shape of crystals, a refractive index coinciding with the *Ng* value of quartz (1.544), and the transition of fluid inclusion contents to hydrohalite during freezing. Hydrohalite is an anisotropic, easily identified phase, which passes into halite again above +0.5°C (Roedder, 1984). Carbon dioxide was identified by specific features of its freezing and the melting temperature, which is close (±0.5°C) to the triple point of pure CO_2 (–56.6°C) (Roedder, 1984). The density of CO_2 was calculated from the temperature and the type of homogenization, taking admixtures of other gases into account (Thiery et al., 1994). The presence of methane was determined by liquid–gas transitions below the critical temperature of chemically pure methane (–82.6°C) and by the presence of gas hydrates at a temperature above +10°C (Claypool and Kaplan, 1974), while a nitrogen admixture was detected by the closeness of the liquid–gas transition to the critical temperature of chemically pure nitrogen (–146.9°C). Gas hydrates in fluid inclusions were identified by the temperature of their existence and by their growth from the diminishing gas phase. The composition of the main salt components in solutions was determined from the eutectic temperature (Borisenko, 1977). Salt concentrations in solutions of two-phase inclusions were estimated from the temperature of ice melting, and in three-phase inclusions, from the temperature of crystal dissolution in the $NaCl–H_2O$ system (Bodnar and Vityk, 1994). The salt concentration in fluid with a high CO_2 content was estimated from the temperature of gas hydrate melting (Collins, 1979). This method (Collins, 1979; Darling, 1991) cannot be applied to inclusions filled with a dense $CO_2–CH_4$ fluid (largely in quartz pertaining to the gold-ore stage) because the temperature of gas hydrate melting in such inclusions is above +10°C owing to the high methane content. Therefore, the salt concentration in the solution of such inclusions was estimated from the temperature of ice melting with a correction for water bound in the gas hydrate (Distler et al., 2004). Carbon dioxide and methane concentrations in solution were calculated from volumetric proportions of particular fluid components (Prokof'ev and Naumov, 1987). In the cases where minerals contained syngenetic carbon dioxide–water inclusions, the pressure was determined from the intersection of the isochore and the isotherm (Kalyuzhny, 1982). The fluid inclusions that captured heterogeneous fluids on the line of two-phase equilibrium and not requiring corrections for pressure were homogenized at the highest temperature (Roedder, 1984).

Aqueous and gas extracts were analyzed in a charge of 0.5 g (0.50–0.25 mm fraction) at the Central Institute of Geological Exploration for Base and Precious Metals using the technique described by Kryazhev et al. (2003). The basic flow sheet of determination of the bulk chemical composition of fluid inclusions included cleaning of the sample, opening of fluid inclusions, and determination of the composition of the released components. The cleaning was carried out first with a HNO_3 (1 : 1) solution and then electrolytically in a water flow using an ultrasonic bath. This method allowed complete removal of surficial contamination within three hours. A dried sample was placed into a disposable glass reactor, which was vacuumized at 110°C and filled with helium. A special setup enabled fluid inclusions to be opened by mechanical or thermal methods depending on the problem to be solved. Thermal opening was performed by heating to 400°C. Mechanical opening was realized using small corundum balls and a vibrator at 120°C in order to suppress sorption of gases and to permit quantitative analysis of H_2O. The released gases were introduced with a dosing valve into a Tsvet-100 gas chromatograph equipped with a flow divider for simultaneous determination of H_2O, CO_2, CH_4, and other gases. Deionized water (7 ml) was poured into the reactor filled with a crushed or decrepitated sample and the reactor was placed in an ultrasonic bath for 15 min. The solution of extract was separated by centrifuging and analyzed with ion chromatography on a Tsvet-3006 liquid chromatograph to determine Cl^-, F^-, SO_4^{2-}, and NO_3^- with a detection limit of 0.01 mg/l (analyst Yu.V. Vasyuta). Other components were analyzed with ICP MS on an Elan 6100 mass spectrometer (analyst I.V. Grigor'eva). The concentration of HCO_3^- was calculated from the balance of cations and anions in the

Table 7. Results of the study of individual fluid inclusions in quartz from ore veins at the Nezhdaninsky deposit

Sample	Zone, level, m	Mineral	*n*	T_{hom}, °C	T_{eut}, °C	$T_{ice\ melt}$, °C	$T_{CO_2\ melt}$, °C	$T_{CO_2\ hom}$, °C	$T_{gas\ hydr\ melt}$, °C	C_{salt}, wt % NaCl equiv	C_{CO_2}, mol/kg sol	C_{CH_4}, mol/kg sol	*D*, g/cm^3	*P*, bar	$(P_{H_2O} + P_{gas})/P_{H_2O}$
Gold-ore stage															
Sh-22-2	Zone 1,	Quartz* (P)	23	330–280	–36…–30	–5.6…–5.0	–57.4…–57.1	26.9…30.0 (L)	9.4–9.0	6.6–5.4	5.2–3.8	0.9–0.7	0.97–0.95	1870–960	9.6–26.2
	+1450	″* (P)	24	–	–	–	–57.7…–57.2	14.2…27.9 (L)	–	–	–	–	0.83–0.66		
Sh-22-1	Zone 1,	Quartz* (P)	17	318	–29	–7.1	–57.6	26.9…27.8 (L)	9.6	8.3	4.9	0.8	1.00	1370	13.0
	+1450	″* (P)	5	–	–	–	–57.7	23.5 (L)	–	–	–	–	0.73		
64Gr-78	Zone 1	Quartz* (P)	6	293–284	–32	–4.8	–59.2	28.7…29.2 (L)	8.4	3.2	4.0–3.4	0.8–0.7	0.91–0.95	660–490	9.4–7.5
	+1200	″* (P)	18	–	–	–	–60.5…–59.3	22.8…24.3 (L)	–	–	–	–	0.60–0.40		
N-7	Zone 1,	Quartz* (P)	11	290–275	–31	–7.1	–57.2	30.6 (G)	8.1	3.8	3.4	0.7	0.93	1180–560	18.1–10.2
	+1100	″* (P)	9	–	–	–	–58.0…–57.2	20.5…30.6 (L)	–	–	–	–	0.72–0.47		
262Gr-77	Zone 1,	Quartz* (P)	12	344–340	–27…–22	–3.3…–2.9	–	–	–	5.4–3.3	–	–	0.69	1360–1200	9.7–8.6
	+900	″* (P)	23	–	–	–	–64.8…–64.6	–7.2…–6.0 (L)	–	–	–	–	0.71–0.67		
		″ (S)	3	–	–	–	–65.2	–91.0 (L)	–	–	–	–	n.a.	–	–
206Gr-77	Zone 1	Quartz* (P)	3	341	–26	–3.2	–	–	–	5.3	–	–	0.69	880	6.3
	+700	″* (P)	26	–	–	–	–	–92.9 (L)	–	–	–	–	0.18		
		Quartz* (P)	16	283–267	–34	–2.8	–	–	–	4.7	–	–	0.79–0.82	850–810	12.1–16.3
		″* (P)	13	–	–	–	–	–97.6 (L)	–	–	–	–	0.20		

Table 7. (Contd.)

Sample	Zone, level, m	Mineral	*n*	T_{hom}, °C	T_{eut}, °C	$T_{ice\ melt}$, °C	$T_{CO_2\ melt}$, °C	$T_{CO_2\ hom}$, °C	$T_{gas\ hydr\ melt}$, °C	C_{salt}, wt % NaCl equiv	C_{CO_2}, mol/kg sol	C_{CH_4}, mol/kg sol	D, g/cm^3	P, bar	$(P_{H_2O} + P_{gas})/P_{H_2O}$
411-682	Zone 1,	Quartz* (P)	24	315–295	–31	–4.3… –3.7	–58.0… –57.9	26.8 (L)… 26.2 (G)	8.8	2.4	5.3–3.3	0.8–0.7	0.95–0.92	1025–860	12.3–10.2
	+400	″* (P)	27	–	–	–	–57.7	26.2… 27.2 (L)	–	–	–	–	0.63–0.60		
409-168	Zone 1,	Quartz* (P)	20	333–285	–33… –32	–6.7… –6.5	–58.0	28.1… 24.7 (G)	9.6	0.8	3.8–2.8	1.0–0.7	0.95–0.86	1510–890	15.6–8.0
	+320	″* (P)	23	–	–	–	–58.3… –58.0	16.5… 26.2 (L)	–	–	–	–	0.75–0.58		
611-433	Zone 1,	Quartz* (P)	9	335–324	–27	–6.9	–58.0	5.9 (L)	11.2	7.1	7.2	1.0	1.08	1370–1010	11.0–8.6
	+200	″* (P)	35	–	–	–	–58.4… –57.7	25.3… 20.5 (L)	–	–	–	–	0.71–0.61		
418-556	Zone 1,	Quartz* (P)	16	318–301	–32	–8.1	–57.7	28.4 (L)	7.2	5.4	4.0	0.7	0.95	1390–910	17.4–10.0
	+100	″* (P)	29	–	–	–	–58.6… –58.0	17.1… 25.2 (L)	–	–	–	–	0.74–0.61		
250-970	Zone 1,	Quartz* (P)	15	368–326	–34… –33	–7.6… –6.3	–58.1… –57.7	24.6… 26.0 (L)	8.8–7.6	4.7–2.4	4.8–4.2	0.8–0.7	0.98–0.96	1710–990	11.4–7.5
	+50	″* (P)	24	–	–	–	–58.0… –57.8	17.6… 26.8 (L)	–	–	–	–	0.75–0.60		
644b-1045	Zone 1,	Quartz* (P)	6	340–303	–31	–7.9	–57.8	26.6 (L)	8.2	3.6	5.4	0.8	0.98	1480–1190	13.2–10.5
	–200	″* (P)	15	–	–	–	–57.5… –57.4	–13.6… 7.0 (L)	–	–	–	–	0.97–0.87		
1/9-13	Zone 3,	Quartz* (P)	5	320–285	–32	–8.9	–58.0	31.0 (L)	8.6	2.8	3.8–3.0	0.8–0.6	0.95–0.99	1530–1030	17.2–14.5
	+700	″* (P)	24	–	–	–	–57.5… –57.4	18.6… 25.1 (L)	–	–	–	–	0.77–0.68		

Table 7. (Contd.)

Sample	Zone, level, m	Mineral	n	T_{hom}, °C	T_{eut}, °C	$T_{ice\ melt}$, °C	$T_{CO_2\ melt}$, °C	$T_{CO_2\ hom}$, °C	$T_{gas\ hydr\ melt}$, °C	C_{salt}, wt % NaCl equiv	C_{CO_2}, mol/kg sol	C_{CH_4}, mol/kg sol	D, g/cm^3	P, bar	$(P_{H_2O} + P_{gas})/P_{H_2O}$
361-112	Zone 3,	Quartz* (P)	12	345–319	–34…–32	–7.3…–6.7	–58.2…–57.9	27.4…28.0 (L)	8.8–8.4	3.2–2.4	4.5–3.8	0.9–0.7	0.96–0.90	1060–670	7.6–5.7
	+450	″* (P)	16	–	–	–	–58.2…–57.9	24.6…28.8 (L)	–	–	–	–	0.60–0.46		
671-276	Zone 8,	Quartz* (P)	7	334	–39	–4.7	–57.8	30.6 (LC)	4.6	6.3	3.7	0.5	0.94	1460–1250	11.3–9.6
	+1150	″* (P)	11	–	–	–	–57.8…–57.4	23.3…27.1 (L)	–	–	–	–	0.74–0.68		
Silver–base-metal stage															
168/1Gr-78	Zone 1,	Quartz* (P)	7	387–369	–35…–32	–6.2…–6.0	–59.2…–59.0	23.6 (L)…7.4 (G)	10.0	8.4–7.9	3.9–2.0	1.1–0.8	0.85–0.88	1330–730	5.6–3.7
	+900	″* (P)	29	–	–	–	–59.8…–58.6	13.5…19.7 (L)	–	–	–	–	0.62–040		
		″ (S)	11	241	–36	–5.5…–4.3	–	–	–	8.6–6.9	–	–	0.88–0.87	–	–
39Gr-78	Zone 1,	Quartz* (P)	5	337	–33	–4.3	–	–	14.8	6.7	0.1	1.6	0.78	1840	14.2
	+700	″* (P)	11	–	–	–	–65.6	–35.8 (G) CO_2 –96.6 (G) CH_4	–	–	–	–	0.54		
		Quartz (S)	13	239	–38	–5.3	–	–	–	8.3	–	–	0.88	–	–
16/16	Zone 1,	Quartz* (P)	22	325–249	–36…–31	–4.5…–3.1	–57.8…–57.7	30.7 (L)…28.2 (G)	8.6–7.8	4.3–2.8	3.0–1.9	0.7–0.5	0.96–0.92	1680–520	14.0–11.5
	+700	″* (P)	42	–	–	–	–58.1…–57.7	14.1…28.7 (L)	–	–	–	–	0.79–0.48		
		″ (S)	3	129	–21	–1.4	–	–	–	2.4	–	–	0.95	–	–
ShG-16	Zone 1, +700	Calcite (P)	15	183–170	–23…–21	–2.6…–2.3	–	–	–	4.3–3.9	–	–	–	–	–

Table 7. (Contd.)

Sample	Zone, level, m	Mineral	*n*	T_{hom}, °C	T_{eut}, °C	$T_{ice\ melt}$, °C	$T_{CO_2\ melt}$, °C	$T_{CO_2\ hom}$, °C	$T_{gas\ hydr\ melt}$, °C	C_{salt}, wt % NaCl equiv	C_{CO_2}, mol/kg sol	C_{CH_4}, mol/kg sol	D, g/cm^3	P, bar	$(P_{H_2O} + P_{gas})/P_{H_2O}$
Au–Mo–W stage															
Kurum-1		Quartz	17	282	–23	–3.9	–	–	4.2	6.3	–	–	0.81	–	–
		″	10	247–201	–35…–28	–4.6…–4.2	–	–	–	7.3–6.7	–	–	0.92–0.87	–	–
		″	3	196	–25	–3.1	–	–	–	5.1	–	–	0.91	–	–
Kurum-vein		Quartz* (P)	5	374–367	–25	–6.2	–	–85.9 (G)	17.6	9.5	–	2.5	0.79	390	2.0
		″* (P)	9	–	–	–	–	–149.2 (G)	–	–	–	–	0.17		
		″ (PS)	4	373	–33	–5.2	–	–	–	8.1	–	–	0.68	–	–
13-G-85		Quartz (P)	12	294–275	–35…–31	–4.3…–4.0	–	–	–	6.9–6.5	–	–	0.80–0.83	–	–
K-11		Quartz (P)	11	368	–33	–1.3	–66.0	3.5 (L)	15.5	1.9	3.5	1.3	0.96	–	–
		″* (P)	13	324–319	–30…–27	–5.7…–3.7	–63.7	–7.3 (G)	14.8–14.1	7.5–6.0	1.8	1.5	0.86	510–460	4.0–4.5
		″* (P)	19	–	–	–	–	–142 ... –140 (G)	0.9 N_2 0.1 CH_4	–	–	–	0.22	–	–
		″ (PS)	3	260	–54	–29.7 (+13.5)	–	–	–	26.3	–	–	1.02	–	–
		″ (PS)	6	258	–40	–17.2	–	–	–	20.4	–	–	0.96	–	–
		″ (PS)	15	204–199	n.a.	(183…181)	–	–	–	31.1–31.0	–	–	1.11–1.12	–	–
K-59		Quartz* (P)	3	336	–33	–2.0	–	–	–	3.4	–	–	0.66	1410	10.6
		″* (P)	2	334 G	–28	–4.5	–	–88 (L)	–	7.2	–	–	0.25		
		″* (PS)	3	339	–32	–1.9	–	–	–	3.2	–	–	0.65	400	2.9
		″* (PS)	8	–	–	–	–	–89 (G)	–	–	–	–	0.08		

Note: *n*, number of studied inclusions; *, heterogeneous state of fluid (boiling); n.a., not analyzed. Fluid homogenization: to liquid (L), to gas (G), and with critical phenomena (C). Genetic types of inclusions: P, primary, PS, pseudosecondary, and S, secondary.

solution. Thus, gases, salts, and the aqueous solvent were extracted simultaneously from a fluid inclusion during analysis, enabling reliable calculation of concentrations in solutions. Minimization of the number of analytical procedures dimimished the probability of sample contamination with foreign admixtures in the course of analysis. Standardization of the process ensured the maximum compensation of errors and increased the reliability of determination of the specific composition of each sample. The data on blank extracts were subtracted from the results obtained. The remaining useful signal is related to the contents of fluid inclusions with a high probability. Therefore, it may be assumed that the results of bulk analyses reflect the total concentrations of elements in the solutions that fill fluid inclusions.

Characteristics of Fluid Inclusions

According to the well-known criteria in (Roedder, 1984), we distinguished primary, pseudosecondary, and secondary inclusions. The main attention was focused on primary inclusions, which fill negative crystals and are rounded or irregular in shape. They are located along the growth zone of minerals or distributed uniformly throughout quartz grains. The size of these fluid inclusions mostly varies from 5 to 30 μm; largely, they are 10–15 μm across. The pseudosecondary inclusions are related to fractures that are cut off by outer contours of grains and do not go out farther. The secondary inclusions make up chains that are related to fractures crosscutting grain boundaries.

According to phase composition at room temperature, the fluid inclusions are subdivided into four types (Fig. 14):

(I) Carbon dioxide–water fluid inclusions, in particular, two-phase inclusions with liquid water and a gas phase of mainly dense CO_2 and three-phase inclusions that contain liquid water and liquid and gaseous CO_2.

(II) Substantially gas inclusions, single-phase or two-phase, with a rim of aqueous solution. In most such inclusions, CO_2 is prevalent and admixtures of other phases are insignificant. However, in some inclusions, largely in quartz from Au–Mo–W assemblages, dense methane and nitrogen have been detected.

(III) Two-phase fluid inclusions that contain an aqueous solution of variable mineralization and a low-density gas bubble filled with water vapor.

(IV) Three-phase inclusions with a liquid aqueous solution, a gas bubble, and an isotropic cubic crystal identified as halite.

Fluid inclusions of types I–IV are abundant in quartz from Au–Mo–W veins. The primary inclusions of type II are syngenetic to the primary inclusions of types I and III. Thus, quartz crystallized from boiling fluid that was separating into gas and liquid phases. The primary inclusions of types I and II were found mostly in milky white and regenerated quartz as irregular clusters related to the same growth zones of quartz. This means that these inclusions were captured simultaneously during quartz crystallization. Thus, the minerals crystallized in a system where fluid was separating into an aqueous liquid phase with dissolved carbon dioxide and a gas phase with a predominance of carbon dioxide.

Microthermometric Investigations

The results of thermo- and cryometric measurements of fluid inclusions in quartz pertaining to different stages are summarized in Table 7.

The fluid inclusions of type I in quartz from Au–Mo–W-bearing veins hosted in the Kurum pluton are homogenized at a temperature from 374 to 319°C. The eutectic temperature from –25 to –33°C indicates that $MgCl_2$ and NaCl are dissolved in the fluid. The gas phase is a carbon dioxide–methane mixture with a melting temperature ranging from –64 to –66°C or dense methane with a temperature of homogenization into gas of –84°C. Melting of gas hydrates within a temperature range of 14.1–17.6°C also indicates the presence of methane (Claypool and Kaplan, 1974). CO_2 is homogenized into both liquid (+3.5°C) and gas (–7.3°C) phases. The salinity of the fluid is 3.2–9.5 wt % NaCl equiv (Fig. 15).

In the fluid inclusions of type II, the gas phase is composed of either dense methane homogenized into the gas phase at –89.0°C and into liquid with a density of 0.08–0.25 g/cm^3 at –88.0°C or dense nitrogen homogenized into gas with a density of 0.19 g/cm^3 at –149.2°C. There are also substantially gas inclusions homogenized at –140 to –142°C and containing an admixture of nitrogen (~90 mol %) and methane (~10 mol %) with a total density of 0.22 g/cm^3. The pressure is estimated to be within the range 0.4–1.4 kbar at 375–320°C.

The fluid inclusions of type III are homogenized at 373–196°C. The eutectic temperature varies from –23 to –40°C, indicating that $MgCl_2$ and NaCl are dissolved in the fluid. Ice is melted at a temperature from –3.1 to –17.2°C. Hence, the salinity of the captured fluid ranges from 1.9 to 20.4 wt % NaCl equiv.

The fluid inclusions of type IV are homogenized at 204–199°C. The halite crystal is dissolved at 183–181°C, and the salinity of the fluid is 31.1–31.0 wt % NaCl equiv.

Thus, the microthermometric investigations show that three types of fluids different in composition were captured during crystallization of quartz: (i) an aqueous fluid with dissolved CO_2, CH_4, and Na and Mg chlorides; (ii) a substantially gaseous fluid containing methane and nitrogen; and (iii) a largely aqueous fluid of variable salinity. Since the inclusions that contain fluids (i) and (ii) were captured simultaneously, they are derivatives of one parental fluid that was split into two phases in the course of cooling and pressure release or

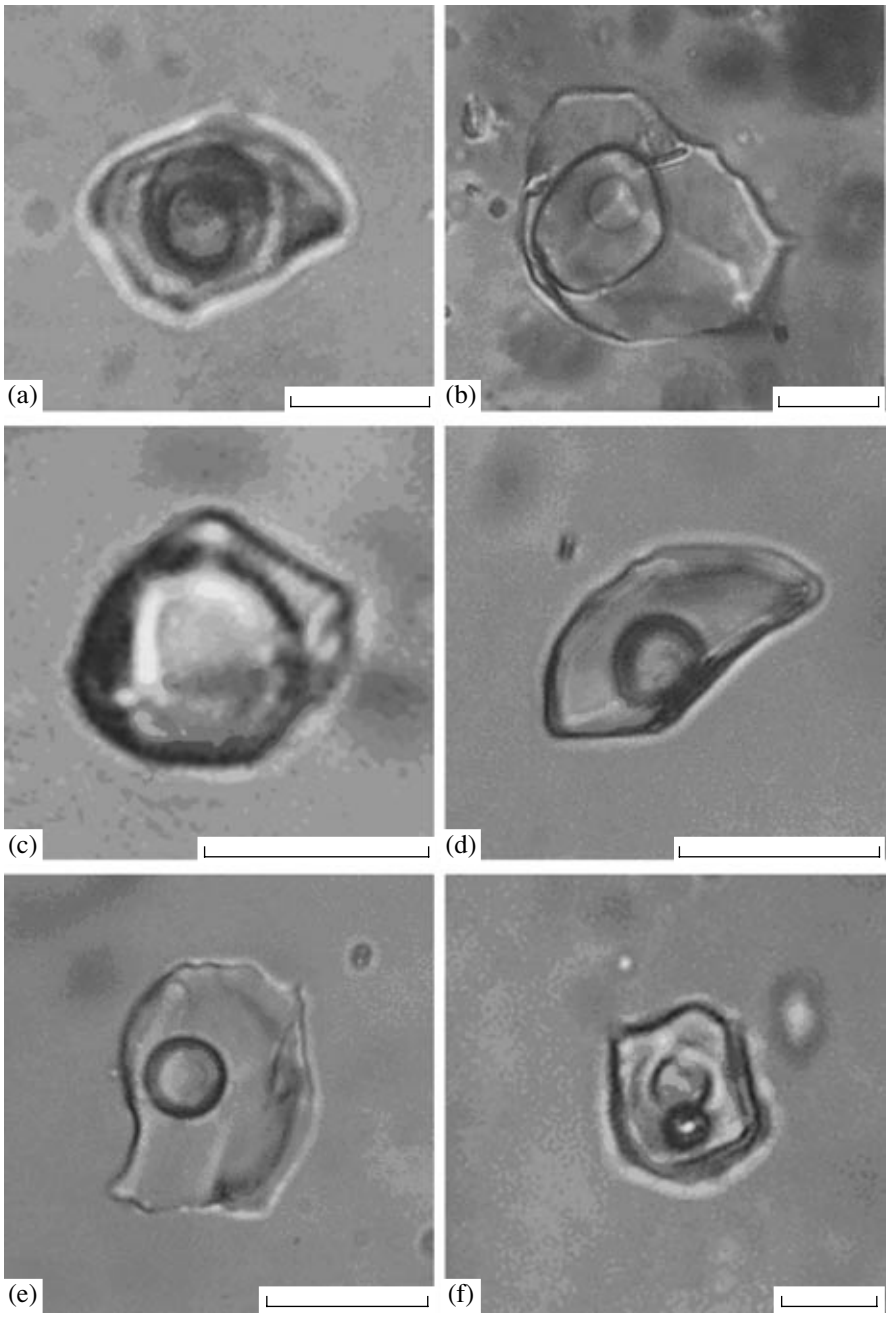

Fig. 14. Types of primary fluid inclusions in quartz from ore of the Nezhdaninsky deposit. (a, b) Carbon dioxide–water (type 1), (c) gas (type 2), (d, e) two-phase gas–liquid (type 3), (f) three-phase inclusions of brine (type 4). Scale bar is 10 μm.

as a result of a pressure drop only (Bowers and Helgeson, 1983; Roedder, 1984). The separation of a fluid consisting of H_2O, CO_2, and NaCl into gas and a water–salt phase may lead to the formation of highly concentrated brines (Bowers and Helgeson, 1983). In the H_2O–CO_2–NaCl system containing 6 wt % NaCl equiv, the separation of fluid into a phase enriched in H_2O and CO_2, on the one hand, and an NaCl-rich liquid, on the other hand, occurs within a temperature range from 600 to 1000°C at 1.0–1.5 kbar pressure. The salinity of the water–salt solution varies widely, probably, owing to the mixing of fluids with different salinity derived from different sources. The variation in carbon dioxide, methane, and nitrogen concentrations in the gas phase may be related to different stages of organic matter decomposition and heterogenization of fluid.

The fluid inclusions of type I captured by *milky white quartz of the gold-ore–quartz stage* are homogenized at 368–267°C. The eutectic temperature, measured within the range –39 to –22°C, allows us to sug-

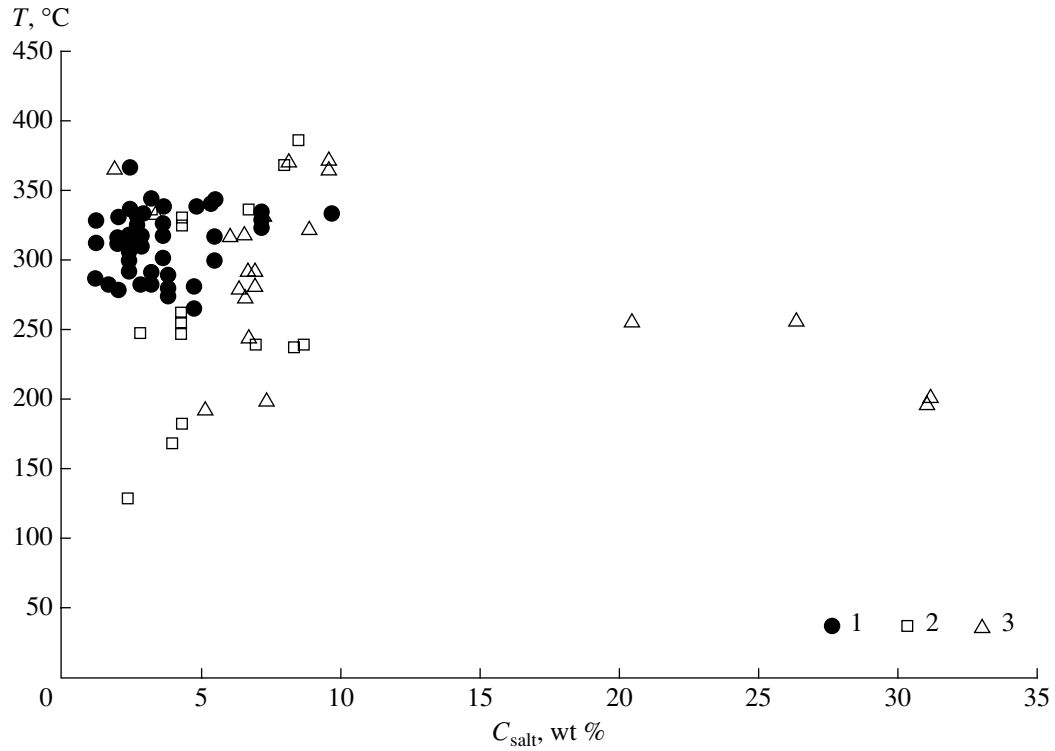

Fig. 15. Concentration–temperature diagram for fluids of the Nezhdaninsky deposit. Mineral assemblages: (1) gold-ore, (2) silver–base-metal, and (3) Au–Mo–W.

gest that KCl, $MgCl_2$, and NaCl were dissolved in the captured fluid. The temperature of gas hydrate melting varies from +4.6 to +11.2°C. The sporadic fluid inclusions with a temperature of gas hydrate melting above +10°C reveal a high methane content. The salinity of the mineral-forming fluid calculated from these data is 7.1–0.8 wt % NaCl equiv. Carbon dioxide is homogenized into liquid within the temperature range 5.9–31.0°C or into gas from 24.7 to 30.6°C. The temperature of CO_2 melting, from –57.1 to –59.2°C, is appreciably lower than melting point of pure CO_2 (–56.6°C) and thus indicates that methane or nitrogen occurs as well. The CO_2 and CH_4 contents in the fluid vary from 7.2 to 3.0 and from 1.0 to 0.5 mol/kg of solution, respectively.

The fluid inclusions of type II in milky white quartz are homogenized within the same temperature interval as the inclusions of type I. Carbon dioxide is homogenized into liquid within the range –13.6 to +30.6°C. According to these results, the carbon dioxide density varies from 0.40 to 0.97 g/cm^3. The temperature of CO_2 melting in these inclusions changes from –57.4 to –63.5°C with a maximum falling at –57.7 to –59.6°C; hence, a small (7–4 mol %) admixture of CH_4 and N_2 occurs in the gas phase.

The homogenization temperature of inclusions in milky white quartz belonging to the gold–quartz stage was measured for the groups of fluid inclusions with similar relative amounts of phases corresponding to the curve of two-phase equilibrium. In this case, the homogenization temperature of inclusions filled with a carbon dioxide–aqueous fluid coincides with the true temperature of mineral formation and does not require corrections for pressure (Naumov, 1982; Roedder, 1984). Hence, milky white quartz crystallized approximately at 370–270°C. The fluid pressure at this temperature was estimated at 0.7–2.0 kbar, taking into account that the density of carbon dioxide inclusions equals 0.83–0.40 g/cm^3.

The primary fluid inclusions of type I found in the *regenerated rock-crystal quartz at the silver–base-metal stage* are homogenized at 387–249°C, and the secondary inclusions, at 241–129°C; inclusions in regenerated carbonate are homogenized at 183–170°C. The eutectic temperature varies from –36 to –21°C, indicating the prevalence of dissolved $MgCl_2$ and NaCl. The salinity of the mineral-forming fluid ranges from 8.6 to 2.4 wt % NaCl equiv. In addition to CO_2, with a concentration varying from 3.9 to 0.1 mol/kg of solution, the fluid contains methane (1.6–0.5 mol/kg of solution) because the temperature of CO_2 melting in inclusions varies from –59.2 to –57.7°C, i.e., is lower than the melting point of pure carbon dioxide.

Fluid inclusions of type II contain dense (0.83–0.61 g/cm^3) CO_2 with an admixture (22–6 mol %) of methane, as follows from the melting and homogenization temperatures of carbon dioxide, changing from –65.6 to –57.7 and –35.8 to +28.7°C, respectively.

Table 8. Chemical composition of aqueous extracts from fluid inclusions in quartz (results of gas and ion chromatography and ICP MS)

Component	Gold-ore stage			Silver–base-metal stage		Au–Mo–W stage	
	1/9-13	250-970	64Gr-78	21Gr-78	39Gr-78	13-G-85	12-G-85
				g/kg H_2O			
CO_2	1546.9	1743.3	266.3	98.2	272.0	29.5	16.3
CH_4	9.9	30.1	1.1	1.0	1.3	54.5	148.5
Cl^-	2.50	2.5	1.6	2.5	1.6	27.8	213.8
HCO_3^-	257.2	293.6	16.6	127.4	18.7	279.0	154.6
Na	34.4	15.3	6.7	n.a.	6.0	27.6	60.3
K	149.6	10.0	1.3	14.4	2.2	131.3	12.8
Ca	3.1	71.1	0.3	21.1	0.3	13.6	101.4
Mg	9.4	4.9	0.04	12.5	0.25	1.5	7.4
				mg/kg H_2O			
Br	1578.6	597.7	34.2	n.a.	13.5	391.0	50.7
Li	102.4	46.7	6.5	257.5	18.2	393.4	200.4
B	2707.9	2774.3	287.1	1015.0	139.9	2625.8	2066.6
Rb	232.9	18.1	1.4	34.2	8.4	199.3	63.1
Cs	37.0	12.3	1.4	7.4	2.0	30.2	32.1
Sr	167.2	241.4	4.6	313.4	10.8	149.1	2828.2
Mo	8.6	n.a.	2.7	n.a.	n.a.	n.a.	n.a.
Ag	52.9	4.8	1.8	2.4	1.0	9.3	0.8
Sb	362.7	88.1	1.1	120.3	088.8	93.9	1610.0
Cd	13.5	7.4	0.3	n.a.	n.a.	6.6	n.a.
Pb	475.7	21.5	1.4	6.6	3.6	40.0	16.0
Bi	2.4	n.a.	0.04	n.a.	0.1	2.2	0.9
Th	2.2	0.4	0.02	0.4	0.05	12.7	1.2
U	4.0	n.a.	0.02	0.8	0.05	5.2	0.8
Ga	20.5	4.6	0.1	24.3	0.9	16.0	2.5
Ge	134.6	71.0	1.1	30.4	9.2	40.8	31.3
Sc	873.9	1220.9	41.8	1907.0	66.3	923.0	253.6
Ti	487.2	114.7	60.5	207.4	17.8	330.3	78.5
Mn	69.2	1046.2	n.a.	1077.4	4.7	39.2	840.9
Fe	4097.5	1497.4	n.a.	5572.8	221.1	2847.5	4611.3
Co	57.4	8.4	0.3	23.3	0.4	6.2	21.5
Ni	114.1	58.7	1.7	52.3	1.1	30.6	124.7
Cr	143.8	134.8	n.a.	130.7	9.5	111.6	93.3
Y	1.6	0.6	0.03	2.2	0.2	4.0	2.2
Zr	11.1	14.7	0.3	9.5	0.7	23.5	2.5
Nb	3.0	1.4	0.1	1.2	0.2	4.6	3.4
In	n.a.	2.0	n.a.	n.a.	0.02	0.2	1.2
Sn	n.a.	1387.5	1.0	n.a.	n.a.	n.a.	n.a.
Ba	658.8	191.1	2.6	4549.6	12.8	257.7	1140.1
W	30.0	36.4	127.1	6.2	0.9	3.4	19.8
Te	n.a.	n.a.	9.2	n.a.	n.a.	n.a.	n.a.
Au	19.9	1.2	0.03	″	0.3	0.8	1.3

Table 8. (Contd.)

Component	Gold-ore stag			Silver–base-metal stage		Au–Mo–W stage	
	1/9-13	250-970	64Gr-78	21Gr-78	39Gr-78	13-G-85	12-G-85
				mg/kg H_2O			
Hg	n.a.	n.a.	0.4	n.a.	n.a.	n.a.	n.a.
Se	″	″	109.0	10.9	184.9	14.9	7.3
Tl	2.4	2.2	0.7	n.a.	0.04	1.6	0.1
ΣREE	24.3	14.1	0.7	24.3	1.4	51.9	5.5
La	6.6	3.4	0.1	7.4	0.37	11.7	1.6
Ce	11.9	7.4	0.13	10.9	0.57	20.1	2.1
Pr	1.6	0.6	0.13	1.0	0.09	3.6	0.26
Nd	2.8	1.8	0.4	2.2	0.2	13.3	0.66
Sm	n.a.	0.4	n.a.	1.0	0.06	1.2	0.26
Eu	0.2	0.2	″	1.0	0.02	0.2	0.26
Gd	0.4	0.2	″	0.2	0.03	0.8	0.13
Tb	0.2	n.a.	″	n.a.	0.01	0.2	n.a.
Dy	0.2	0.2	″	0.2	0.02	0.4	0.26
Yb	0.4	n.a.	″	0.2	n.a.	0.2	n.a.
Hf	0.2	0.2	″	0.2	″	1.0	″
Ta	0.2	n.a.	″	0.2	0.01	1.4	0.3
CO_2/CH_4	156.3	57.9	242.1	98.2	209.2	0.5	0.1
Br/Cl	0.63	0.24	0.02		0.008	0.014	0.0002
K/Rb	642	812	942	420	261	659	202
Br/Cl (molar)	0.30	0.11	0.01		0.0035	0.006	0.0001
K/Ba	227	52	506	3.2	171	509	11
Ba/Rb	2.8	10.6	1.9	133	1.5	1.3	18.1
Rb/Sr	1.4	0.07	0.3	0.11	0.8	1.3	0.02
La/Yb	16.5			37	37		
La/Sm		8.5		7.4	6.5	9.8	6.0
K/Ca	48	0.14	4.2	0.68	6.9	9.7	0.13
Mn/Fe	0.017	0.70		0.19	0.02	0.014	0.18
Zr/Nd	4.0	8.2	0.87	4.4	3.1	1.8	3.8
La/Y	9.9	5.7	3.6	3.4	1.7	3.0	0.7
T, °C	320–285	368–326	293–284	n.a.	337	294–275	n.a.
C, wt % NaCl equiv	2.5	4.7–2.4	3.2	″	6.7	6.9–6.5	″
P, bar	1530–1030	1710–990	660–490	″	1840	n.a.	″

Because in this case the inclusions were captured under conditions of two-phase equilibrium, the homogenization temperatures may be accepted as temperatures of mineral formation. Hence, quartz crystallized at 390–130°C. The pressure of the carbon dioxide fluid (the density is 0.83–0.64 g/cm^3) varied from 1.9 to 0.8 kbar at 390–250°C.

Analysis of Aqueous and Gas Extracts from Fluid Inclusions in Quartz

Additional evidence for the composition of the mineral-forming fluid has been obtained from the bulk compositions of fluid inclusions.

The fluid from inclusions in quartz of the Au–Mo–W stage from pegmatoid and quartz–pyrrhotite veins (Table 8, samples 13-G-85 and 12-G-85) contains HCO_3^- ions (279–155 g/kg H_2O), Cl^- (214–28 g/kg H_2O), and CH_4 (149–55 g/kg H_2O), whereas the CO_2 concentration is relatively low (30–16 g/kg H_2O). These results are consistent with the data on individual inclusions discussed above, in particular, as concerns the occurrence of dense methane in gas inclusions. The fluid from inclusions in quartz from pegmatite is enriched in HCO_3^-, while inclusions from quartz–sulfide veins contain much Cl^- and CH_4. Ca (101–13.6 g/kg

H_2O) and Na (60–28 g/kg H_2O) are predominant as dissolved cations. The fluid from inclusions in quartz from pegmatitic veins contains K (131.3 –12.8 g/kg H_2O), while Mg is detected in insignificant amounts (7.7–1.5 g/kg H_2O). Rather stable B and Br contents (2.6–2.1 and 0.4–0.05 g/kg H_2O, respectively) are typical of this fluid. Fe (4.6–2.8 g/kg H_2O) and Sb (1.6–0.09) have been detected as ore components of the fluid. The highest concentrations of these metals were determined in aqueous extracts from fluid inclusions in quartz of quartz–sulfide veins. The fluids of the Au–Mo–W stage are characterized by Zr/Nd = 1.8–3.8, K/Rb = 202–659, Rb/Sr = 0.11–1.3, La/Y = 0.7–3.0, and La_n/Sm_n = 6.0–9.8.

Three quartz samples from gold–quartz veins (Table 8, samples 1/9-13, 250-970, and 64Gr78) have been studied, including a sample of milky white quartz with large arsenopyrite pockets from ore zone 3 (a level of +700 m) and two samples without sulfides from ore zone 1: one taken at the upper level +1200 m and the second, at the deep level +50 m. The following cations (g/kg H_2O) are predominant in fluids: K (150–1.5), Ca (71–0.3), and Na (34–6.7); Mg (9.5–0.04) occurs in subordinate amounts. The high CO_2 concentration (1743–266 g/kg H_2O) exceeds the solubility of carbon dioxide in an aqueous solution at any parameters, thus indicating the occurrence of abundant gas inclusions formed as a result of fluid heterogenization. Appreciable amounts (g/kg H_2O) of HCO_3^- (294–16.6), CH_4 (30–1.1), B (2.8–0.3), Cl^- (2.5–1.6), and Br (1.6–0.03) have been detected; Fe occurs in a significant amount (4.1–1.5) as an ore element. Many trace elements have been established in fluid (Table 8). The highest concentrations of some ore elements, especially Pb, were revealed in fluid inclusions in quartz that contains arsenopyrite pockets (ore zone 3). Such enrichment could hardly be a result of sample contamination because quartz from deep levels of ore zone 1 is characterized by a rather high contents of these elements as well. The fluid inclusions in quartz from lower levels are enriched in CO_2, CH_4, and HCO_3^- and depleted in Ca, Na, K, and Mg in comparison with the inclusions in quartz from upper levels. It is notable that the concentrations of virtually all components except W decrease upward. However, Bi, Te, Se, and Hg have been detected in fluid inclusions only at the upper levels, where the Ag/Sb, Pb/Zn, and Li/Al ratios increase 24, 12, and 8 times, respectively. The K/Rb ratio reaches 942 at the upper levels against 642 at the lower levels. The K/Rb, La/Y (3.6–6.9), and La_n/Sm_n (8.5) ratios of fluid are much higher than for beresite, whereas the Rb/Sr ratio of fluids pertaining to the gold-ore stage is lower than for beresite (0.07–1.4); the Zr/Nd ratios partly overlap (0.87–8.2).

Two monofractions of quartz regenerated at the silver–base-metal stage (Table 8, samples 21Gr78, 39Gr78) have been investigated: one from a stringer up to 1.5 cm thick that cuts milky white quartz and the other from transparent crystals (1–5 mm in size) lining a leached cavity in milky white quartz. The fluid composition in quartz of these samples turned out to be similar to the compositions of extracts from fluid inclusions hosted in milky white quartz (Table 8). The Zr/Nd (3.1–4.4) and Rb/Sr (0.11–0.80) ratios in fluids of the silver–base-metal stage are obviously lower than in beresite, whereas the K/Rb (261–420), La/Y (1.7–3.4), and La_n/Sm_n (6.5–7.4) ratios approach these parameters of beresite.

Some specific features of trace element and metal behavior in solutions from fluid inclusions (Table 8) should be emphasized. The fluids captured by quartz of pegmatoid veins are enriched in Li, Zr, Y, Nb, REE total, Ta, and Th, i.e., in the elements typical of granite. The contents of ore-forming Pb, Bi, Se, and Ag are relatively high as well. The Sb content is comparable with that in aqueous extracts from fluid inclusions in quartz from sulfide-bearing veins. These data are consistent with the results of mineralogical studies, which have shown that rare Pb, Bi, Se, Ag, and Sb sulfosalts are identified in quartz from pegmatites and cores of aplitic veins, whereas these minerals are not observed in quartz–sulfide veins.

The ICP MS method is applied widely to the analysis of solutions from individual fluid inclusions (Audetat et al., 2000) and in bulk samples (Campbell et al., 1995). The estimates obtained with ICP MS are broadly consistent with the results yielded by other methods (Bodnar and Vityk, 1994) and theoretical estimates of the solubility of various elements (Ridley and Diamond, 2000). Elevated (>1 g/kg H_2O) concentrations of ore elements (Fe, Mn, Zn, Cu, B, etc.) are often detected in ore-bearing fluids (Bodnar et al., 1993; Prokof'ev et al., 2003). High concentrations of ore elements in an ore-forming solution are a necessary condition for the formation of economic ore. At the same time, the fluid composition strongly depends on the mass ratio of the fluid and the host rock involved in reaction with this fluid. If the rock is predominant, the fluid composition reaches equilibrium with the host rock, whereas, in the fluid-dominated regime, the ore-forming fluid retains the specific features of its source, first of all, the ratios of some elements. Judging from the study of fluid inclusions, the fluid- and rock-dominated regimes alternate during the ore formation, so that the host rock exerts a strong influence on the composition of the fluid, which nevertheless retains some attributes of its source.

OXYGEN ISOTOPIC COMPOSITION

The oxygen isotopic composition of quartz was determined for metasomatic rocks and quartz veins of the gold-ore and silver–base-metal stages recognized at the Nezhdaninsky deposit, as well as for Au–Mo–W ore mineralization related to the Kurum pluton. Monofractions of specific quartz generations carefully selected under a binocular microscope were used for this pur-

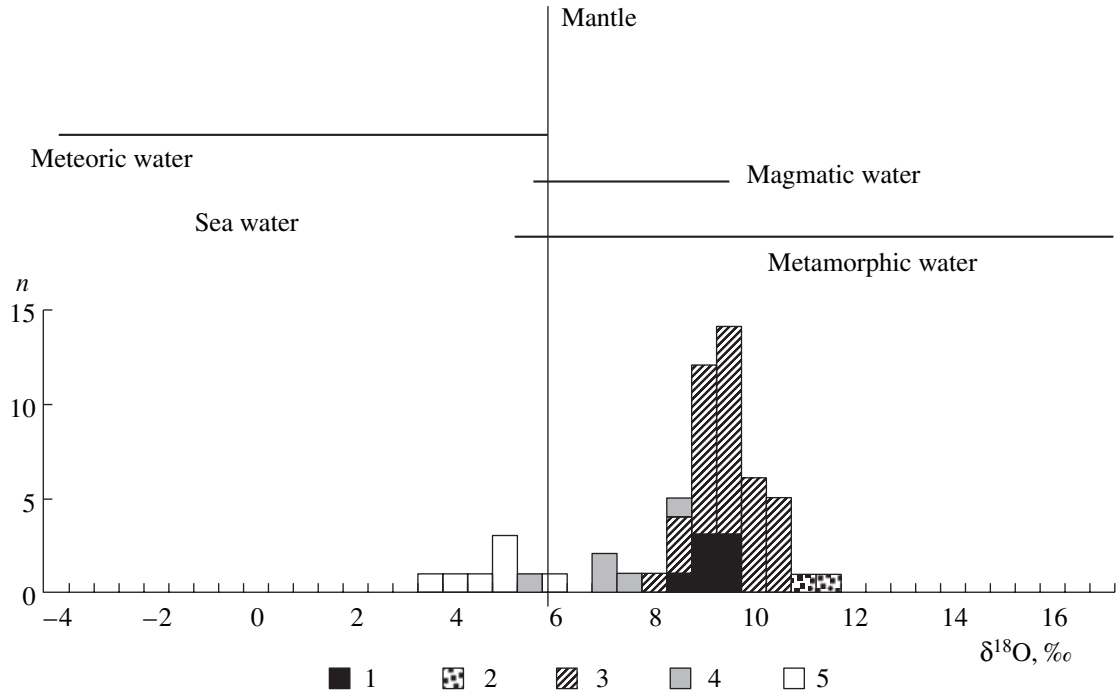

Fig. 16. Oxygen isotopic composition of mineral-forming fluid in the Nezhdaninsky hydrothermal system. (1) Metamorphic quartz, (2) metasomatic quartz, (3) quartz of the gold–ore stage, (4) quartz of the silver–base-metal stage, (5) quartz of Au–Mo–W veins in the Kurum pluton.

pose. The measurements were carried out with IRMS on a DELTA^{plus} (Finnigan) mass spectrometer at the Institute of Geology of Ore Deposits, Petrography, Mineralogy, and Geochemistry, RAS (analyst A.A. Avdeenko). The NBS-28 silicate standard was used. The isotope ratio was measured in CO_2 gas, which was released by interaction of quartz with BrF_5 at 600°C and then with a heated graphite rod. The results are presented as $\delta^{18}O$ relative to SMOW. Repeated measurements of the same sample showed that the uncertainty of $\delta^{18}O$ determinations was ±0.05‰.

The $\delta^{18}O$ values of quartz are rather stable: 10.3–12.6‰ in zones of Au–Mo–W ore mineralization, 15.9–16.4‰ in metasomatic rocks, 14.8–16.6‰ in gold-bearing quartz veins, and 13.5–16.9‰ in silver–base-metal ore mineralization. Our investigation did not confirm the data on enrichment of quartz from Au-bearing veins in the light oxygen isotope (5.0–15.2‰) reported by Bortnikov et al. (1998a). This discrepancy may be caused by an insufficient number of samples and by sampling of different ore zones.

The oxygen isotopic composition of fluid was calculated from equations of isotope fractionation in hydrothermal systems (Ohmoto, 1986) using the measured $\delta^{18}O$ of quartz and homogenization temperature of fluid inclusions therein. The average homogenization temperatures of fluid inclusions were involved in the calculations. It was assumed that isotopic equilibrium between the hydrothermal fluid and precipitating minerals in the quartz–water system had been reached at the temperature of mineral formation and then remained unchanged. The equation $\delta^{18}O_{quartz} - \delta^{18}O_{water} = 3.34(10^6/T^2) - 3.31$ (Matsuhisa et al., 1979), where T is the Kelvin temperature, was used. The fluid that participated in the deposition of Au–Mo–W ore mineralization at 300°C turned out to be enriched in the light oxygen isotope: $\delta^{18}O_{H_2O} = 3.2 \pm 1.2$‰ (Fig. 16). Assuming that quartz of metasomatic rocks precipitated at 360°C, it has been established that $\delta^{18}O_{H_2O}$ of the fluid responsible for metasomatism varied from 10.9 to 11.4‰. The value of $\delta^{18}O_{H_2O}$ of the Au-bearing fluid from which quartz of the gold-ore stage crystallized at 320°C equals 9.0 ± 1.2‰. At the silver–base-metal stage, quartz crystallized from a fluid heated to 260°C that had $\delta^{18}O_{H_2O} = 6.9 \pm 1.7$‰, i.e., was enriched in the light oxygen isotope.

DISCUSSION

The distribution of LILE and REE in rocks, minerals, and fluid inclusions and the oxygen isotopic composition of minerals allowed us to obtain additional insights into the chemical composition of mineral-forming fluid in the Nezhdaninsky ore-forming system and its evolution and probable sources and to develop a genetic model of ore deposition. The results obtained were used for elucidation of the formation conditions of

Table 9. Main parameters of quartz crystallization at different stages of the formation of the Nezhdaninsky deposit

Stage	T_{hom}, °C	C_{salt}, wt % NaCl equiv	C_{CO_2}, mol/kg sol	C_{CH_4}, mol/kg sol	P, bar	P_{tot}/P_{H_2O}
Gold-ore	368…267 (314)	9.6…1.2 (3.5)	7.2…3.0	1.0…0.5	1950…720 (1370)	46.6…8.8 (15.0)
Siver–base-metal	387…129 (264)	8.6…2.4 (5.4)	3.9…0.1	1.6…0.5	1890…790 (1260)	38.9…5.8 (16.1)
Au–Mo–W	374…199 (293)	31.1…1.9 (10.2)	3.5…0	2.5…1.3	1410…400 (710)	10.6…2.9 (5.4)

Note: Numerals in parentheses are average values for the stage.

ore deposition and sources of hydrothermal fluids. Both similarities and differences in the fluid regime during the development of the Nezhdaninsky hydrothermal–magmatic system have been revealed (Table 9). The similarity in maximum homogenization temperatures of fluid inclusions in quartz from ore veins of different types attracts attention. This implies that mineral formation started at a similar, relatively high (365–380°C) temperature and went on against a temperature drop. In the fluid responsible for crystallization of quartz at the gold-ore stage, the salt and CH_4 concentrations are the lowest, while the CO_2 content is relatively high. The highest salt and CH_4 contents, along with the minimal CO_2 concentration, were established in the parental fluid of quartz that bears Au–Mo–W ore mineralization. At the gold-ore stage, the CO_2/CH_4 and CO_2/HCO_3^- ratios in fluid decrease with depth from 242 to 58 and from 16 to 6, respectively. The alkali earth metal/alkali metal ratio increases in the same direction: (Mg + Ca)/(Na + K) grows from 0.04 to 3.0 and Ca/Na, from 0.04 to 4.65. In the fluid of the silver–base-metal stage, CO_2/CH_4 varies from 209 to 98. In the fluid related to the Au–Mo–W ore mineralization in the Kurum pluton, this ratio is 0.1–0.5, while CO_2/HCO_3^- is 0.1. High-temperature fluids have low CO_2/CH_4 values that increase with cooling and release of the gas phase (Sherlock et al., 1999). The increase in CO_2/CH_4 from the Au–Mo–W stage to the later productive stages indicates that oxygen activity increases in the hydrothermal ore-forming system, probably, as a result of involvement of meteoric water enriched in oxygen.

The maximum fluid pressure occurred during formation of quartz veins of the gold-ore stage, whereas the minimum pressure was established for the Au–Mo–W stage. The K/Ca ratio of ore-forming fluids at all three stages often is above unity, while Mn/Fe is below 0.24, as is typical of the early postmagmatic fluids at gold deposits of Alaska (Baker et al., 2006). At the same time, the occasional values of K/Ca < 1 and Mn/Fe > 0.24 may indicate that a fluid distinct in its origin participated in the hydrothermal process. The K/Ba and Rb/Sr ratios (3.2–509 and 0.02–1.40, respectively) of ore-forming fluids at the Nezhdaninsky deposit are rather low, as is characteristic of postmagmatic fluids (Kerrich, 1989). The rather high La/Yb ratio (16.5–37) is also acceptable for postmagmatic fluid. The anionic ratios in a solution change as a result of interaction with host rocks to a lesser extent than the cationic composition does. Therefore, the Br/Cl ratio is often used for the identification of fluid origin. The Br/Cl ratios of fluid inclusions in quartz of the silver–base-metal stage (0.008) and the Au–Mo–W stage (0.001–0.014) are close to the values typical of magmatic water (Boehlke and Irvin, 1992). However, in fluid inclusions in quartz of the gold-ore stage, the value is higher (0.021–0.631), probably, owing to the supply of Br from terrigenous rocks deposited under conditions of an arid climate.

Boron accumulates in the volatile phase of hydrothermal–magmatic systems. The fluids enriched in boron are the closest to the magmatic process. Fluid inclusions at pegmatite and skarn deposits contain 0.6–54 g B/kg of solution, while, at Sn, W, and Be deposits, fluid inclusions contain from 0.07 to 3.5–6.0 g B/kg of solution (Prokof'ev et al., 2003). For gold deposits, values of 0.01–4.6 g B/kg of solution were reported. Similar values were established for fluid inclusions in quartz of the Au–Mo–W and gold-ore stages at deep levels of the Nezhdaninsky deposit (2.1–2.6 and 2.7–2.8 g B/kg, respectively). In fluid inclusions in quartz of the gold-ore stage at the upper levels and in quartz of the silver–base-metal stage, the boron content is lower by an order of magnitude (0.3 and 0.1–1.0 g B/kg of solution, respectively), indicating a decrease in the contribution of magmatic fluid from the lower to the upper levels and from the older to the younger stages of mineral formation.

A distinct relationship has been revealed between the temperature of fluid inclusion homogenization and the salt concentration in the solution (Fig. 15). The T_{hom}–C_{NaCl} diagram demonstrates three trends that characterize this relationship for the gold-ore, Au–Mo–W, and silver–base-metal types of ore mineralization. The flat trend for fluid inclusions in quartz of gold orebodies testifies to a relatively stable temperature regime (350–275°C) and only a slight variation in the salt concentration. The trend for fluid inclusions in quartz from Au–Mo–W zones is slightly inclined to the axis of concentration and exhibits a steadily decreasing concentration of salts from the initial crystallization temperature (420°C) to the final temperature (340°C). The most evident is the trend for homogeneous aqueous inclusions in quartz associated with silver–base-metal mineralization. In the region of low temperatures, this trend is

inclined to the axis of concentration at a still greater angle. A systematic decrease in solution salinity and homogenization temperature of fluid inclusions is commonly regarded as an indication of mixing of solutions different in salinity and temperature (Roedder, 1984). It may be suggested that the revealed T_{hom}–C_{NaCl} trends point to the participation of high-temperature and highly concentrated fluids together with low-temperature and low-concentration solutions in the mineral deposition at the Au–Mo–W and silver–base-metal stages. In general, a wavelike change of physicochemical parameters with depth is observed at the deposit.

The results obtained expand substantially the previous knowledge on the fluid regime of mineral formation at the Nadezhdinsky deposit (Bortnikov et al., 1998a). It has become evident that the ranges of crystallization temperature, salinity of solutions, and pressure (Table 9) are wider than was suggested several years ago. It has been established that high-temperature and highly concentrated fluids participated in the mineral formation and that phase separation of the fluid, giving rise to the coexistence of a CO_2-bearing aqueous liquid and a carbon dioxide gas phase, was supplemented by mixing of a high-temperature, relatively highly concentrated chloride solution with a fluid having a low temperature and low mineralization. An aqueous salt solution also took part in the mineral formation. The redox conditions changed from equilibrium with CH_4-bearing fluid at the Au–Mo–W stage to equilibrium with carbon dioxide at the gold-ore stage. Thus, the fluid regime of mineral formation in the Nezhdaninsky hydrothermal–magmatic system turned out to be more complex than was assumed previously.

In the Nezhdaninsky ore field, minerals precipitated from fluids that differed in cationic, anionic, and gas compositions. At the Au–Mo–W stage, quartz was formed from K- and Ca-bicarbonate–chloride–methane fluid and a substantially water fluid; quartz of the gold-ore stage crystallized from K- and Ca-carbonate and bicarbonate fluid; and quartz of the silver–base-metal stage, from Ca-, K-, and Mg-carbonate and bicarbonate fluid.

The composition and *P–T* parameters of fluid inclusions in quartz of the Au–Mo–W, low-sulfide gold-ore, and silver–base-metal stages testify to their different formation conditions and structural localization. The trace element composition of fluid inclusions show that fluids of the Au–Mo–W and gold-ore stages are close to each other in ore components of solutions, assortment of granitophile elements, concentrations of elements, and their ratios. These data corroborate the previous statement about low-sulfide gold and Au–Mo–W mineralization as derivatives of a common gold-ore–magmatic system.

As has been shown above, the K/Rb ratio decreases in preore beresite along with enrichment in both elements relative to terrigenous rocks. In the superimposed ore-bearing beresite, K and Rb contents and the K/Rb ratio increase. The preore metasomatic rocks are distinguished by enrichment in K, Rb, and Cs and depletion in Ba and Sr. As a result, the K/Ba ratio grows, whereas the Ba/Rb, Li/Mg, and K/Cs ratios diminish. A similar enrichment in Rb along with decreasing a K/Rb ratio was established in some Chilean porphyry copper deposits and interpreted as a result of interaction of host rocks with high-Rb postmagmatic fluid (Armbrust et al., 1977). The progressive development of the hydrothermal process is accompanied by increasing LILE and HREE contents and depletion in HFSE irrespective of the formation conditions of metasomatic rocks. A gain in REE with increasing degree of rock foliation was pointed out. The Eu/Eu* and Ce/Ce* ratios are close to unity, indicating that a relatively oxidized fluid participated in the formation of metasomatic rocks.

Decreasing K/Rb and K/Li ratios in line with increasing K/Ba and Rb/Sr ratios in mineralized rocks relative to host granitoids at Sn–W deposits is regarded as evidence for the participation of magmatic fluid (Govett, 1985; Kerrich, 1989). Hence, the behavior of lithophile elements during the formation of preore metasomatic rocks may be related to the replacement of terrigenous rocks with magma-derived fluid. Indeed, Li, Rb, Cs, and Ga are gained and Ba and Sr lost in the late derivatives of the Kurum pluton spatially associated with metasomatic rocks; thereby, the K/Rb, K/Cs, K/Li, K/Tl, Ba/Rb, and Rb/Cs ratios decrease and the K/Ba, Rb/Sr, and Li/Mg ratios increase.

Magmatic processes commonly lead to diminishing K/Rb, K/Li, K/Cs, K/Tl, Rb/Cs, and Al/Ga ratios and increasing K/Ba and Rb/Sr ratios relative to the average crustal values or MT (Kerrich, 1989). The Archean mesothermal gold deposits are characterized by the following specific features: (i) K/Rb, K/Cs, K/Tl, and K/Ba ratios are close to the crustal values or higher; (ii) Rb/Sr, K/Cs, and K/Tl ratios are variable; and (iii) Al and Ga behave isochemically. As has been shown for the Nezhdaninsky deposit, (i) K/Rb, K/Li, Rb/Sr, and K/Ba ratios are higher and considerably higher than the respective average crustal values and (ii) the K/Cs ratio (three-fourths of analyses) is below the average crustal value. In the course of the hydrothermal process (the formation of ore-bearing metasomatic rocks), the decrease in the Ba/Rb and Li/Mg ratios is combined with a magmatic tendency toward an increase in the K/Ba ratio and a decrease in the K/Cs ratio, which may indicate the participation of magmatic fluid in the ore deposition. The correspondence of the K/Rb and K/Ba ratios to the MT implies that K, Rb, and Ba contents are distributed in the hydrothermal ore-forming fluid in line with the respective ratios in the magma source.

For recognition of the fluid origin, it is important to establish a similar distribution of trace elements, including REE, in igneous, terrigenous, and metasomatic rocks (Fig. 4). In distribution of trace elements, dikes in the Nezhdaninsky ore field are similar to gran-

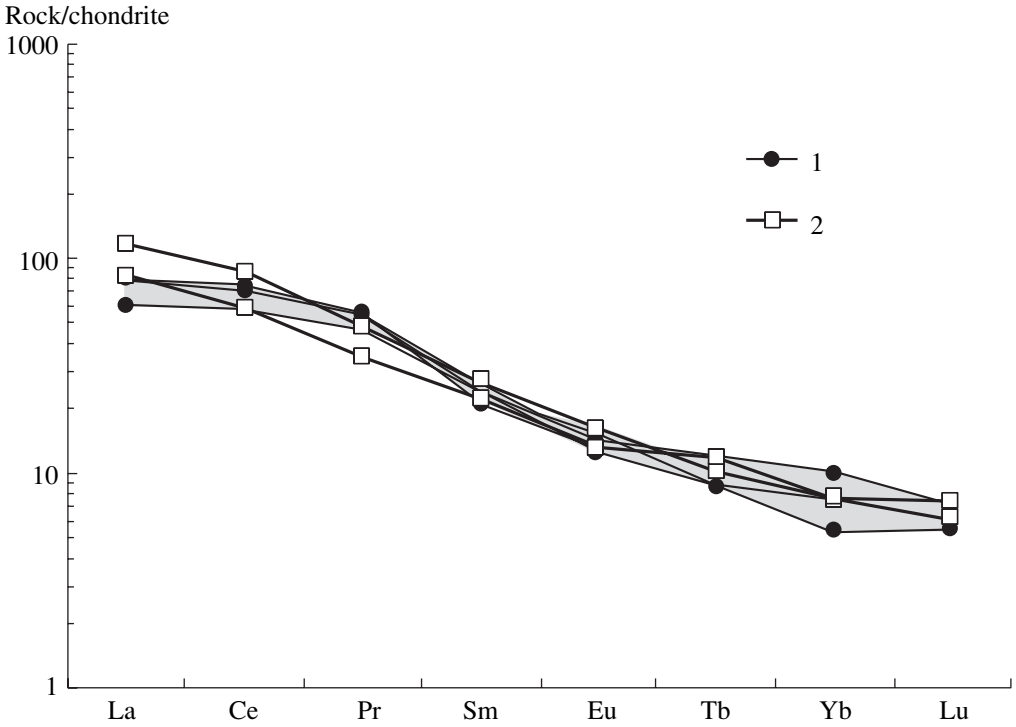

Fig. 17. Chondrite-normalized REE patterns of igneous and country terrigenous rocks in the Nezhdaninsky ore field. (1) Siltstone, (2) granitoids of the Kurum pluton. The field of terrigenous rock is gray.

itoids of the Kurum pluton, but they are distinguished by somewhat lower Rb, K, and Nb contents and higher REE contents. Metasomatic rocks are similar to terrigenous and igneous rocks in distribution of elements but are enriched in Nb, while Sr and Ti concentrations are comparable with those in terrigenous rocks (Fig. 17). Similar REE patterns of igneous and terrigenous rocks (Fig. 17) prevent an unequivocal suggestion on the REE source from being made. The lithological control of LILE distribution more likely testifies in favor of involvement of components extracted from host rocks in the hydrothermal system.

At the stage of preore mineralization, both rocks and minerals are enriched in LREE and show a positive Eu anomaly. The La_n/Yb_n ratio may be explained by accumulation of LREE in fluid at the stage of preore beresitization; deposition of carbonates at the productive stages is accompanied by complexing. The redox parameters of fluid during carbonate crystallization are shown in Fig. 13a. A significant positive Eu anomaly (Eu/Eu* = 38.8) in scheelite II (sample 13/6-29) indicates its crystallization from a reduced fluid and/or from a fluid with a positive Eu anomaly (Fig. 13b). The enrichment of the early scheelite and coexisting carbonate in REE testifies to the enrichment of hydrothermal fluid in REE.

All studied rocks and minerals are enriched in LREE. However, fractionation of granitoids in the Kurum pluton resulted in depletion in REE and growth of the contribution of HREE. A similar tendency is observed in the hydrothermal process as well. The contribution of HREE increases from preore to ore-bearing metasomatic rocks, from preore to regenerated carbonates, and from earlier to later scheelite. The REE contents are directly correlated with the mineral composition of metasomatic rocks. In the compression zones, the increase in REE content is caused by the reduction of the quartz volume by 30–35%. In the zones of decompression, REE contents are diluted by newly formed quartz and albite. The REE concentrations in fluid inclusions in quartz are not high (0.7–50 ppm); however, the enrichment in LREE is obvious.

The fluids related to granitoids are enriched in LILE (Rb, Cs, and Li); sedimentary rocks are distinguished by high concentrations of Sr, Mn, Sc, and V (Jiang et al., 2004). The enrichment of metasomatic rocks at the Nezhdaninsky deposit in Rb, Cs, Sc, and V testifies to the dual nature of the hydrothermal fluid. The enrichment of fluid inclusions captured by quartz of the Au–Mo–W assemblage and of the gold-bearing veins at the lower levels of the deposit in Rb, Cs, and Li indicates that magma-derived water participated in the Nezhdaninsky hydrothermal system.

The percentage of the light oxygen isotope in mineral-forming fluid of the Nezhdaninsky hydrothermal–magmatic system increases from older to younger stages of mineral formation. As was pointed out by Bortnikov et al. (1998a), the Nezhdaninsky deposit differs from many mesothermal gold deposits elsewhere in its formation from fluid with a relatively low ^{18}O. As a rule, ^{18}O of the fluids responsible for deposition of

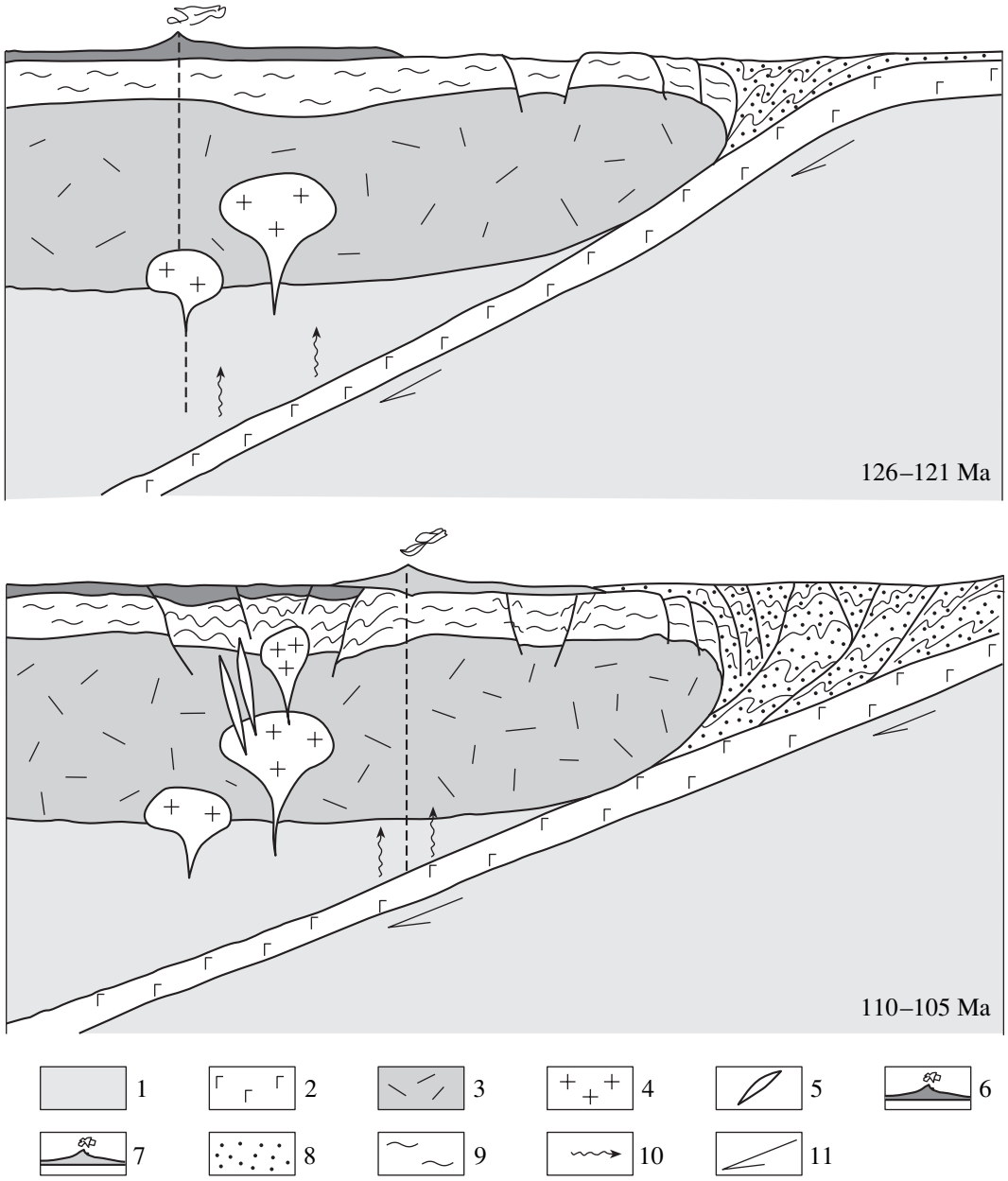

Fig. 18. Sequence of magmatic events in the Nezhdaninsky ore field. (1) Mantle; (2) oceanic plate; (3) Earth's crust; (4) granitoids; (5) dikes; (6) Early Cretaceous (Neocomian) lava; (7) Albian–Late Paleozoic lava; (8) Cretaceous sandstone; (9) Carbonaceous–Triassic intercalating mudstone, siltstone, and sandstone; (10) migration of solution; (11) movement of tectonic blocks.

gold ore localized in metasedimentary rocks falls within a range of 5–10‰ (Nesbitt, 1991) or 7–13‰ (Goldfarb et al., 1991). Our results fall within the interval typical of the fluids of mesothermal ore-forming systems. It is not always possible to distinguish the fluid of magmatic origin from the fluid that was produced by dehydration in the process of regional metamorphism because the oxygen isotopic compositions of the fluids partly overlap or may be changed owing to interaction with host rocks. The values of $\delta^{18}O_{H_2O}$ of +9.0 ± 1.2‰ in fluid of the gold-ore stage and +6.9 ± 1.7‰ in fluid responsible for deposition of the silver–base-metal ore allow us to suggest that water was supplied from both a magmatic source with $\delta^{18}O$ = +(5.5–9.0)‰ and as a product of dehydration of sedimentary rocks. The oxygen isotopic composition of the fluid that gave rise to the formation of Mo–W ore mineralization shows that the water also could have been of magmatic origin and subsequently enriched in the light oxygen isotope owing to interaction with host rocks, whose $\delta^{18}O$ ranges from 1.5 to 12.3‰ (Bortnikov et al., 1998a) and is lower than that of shales and mudstones, with typical $\delta^{18}O$ values varying from 13 to 20‰ (Tay-

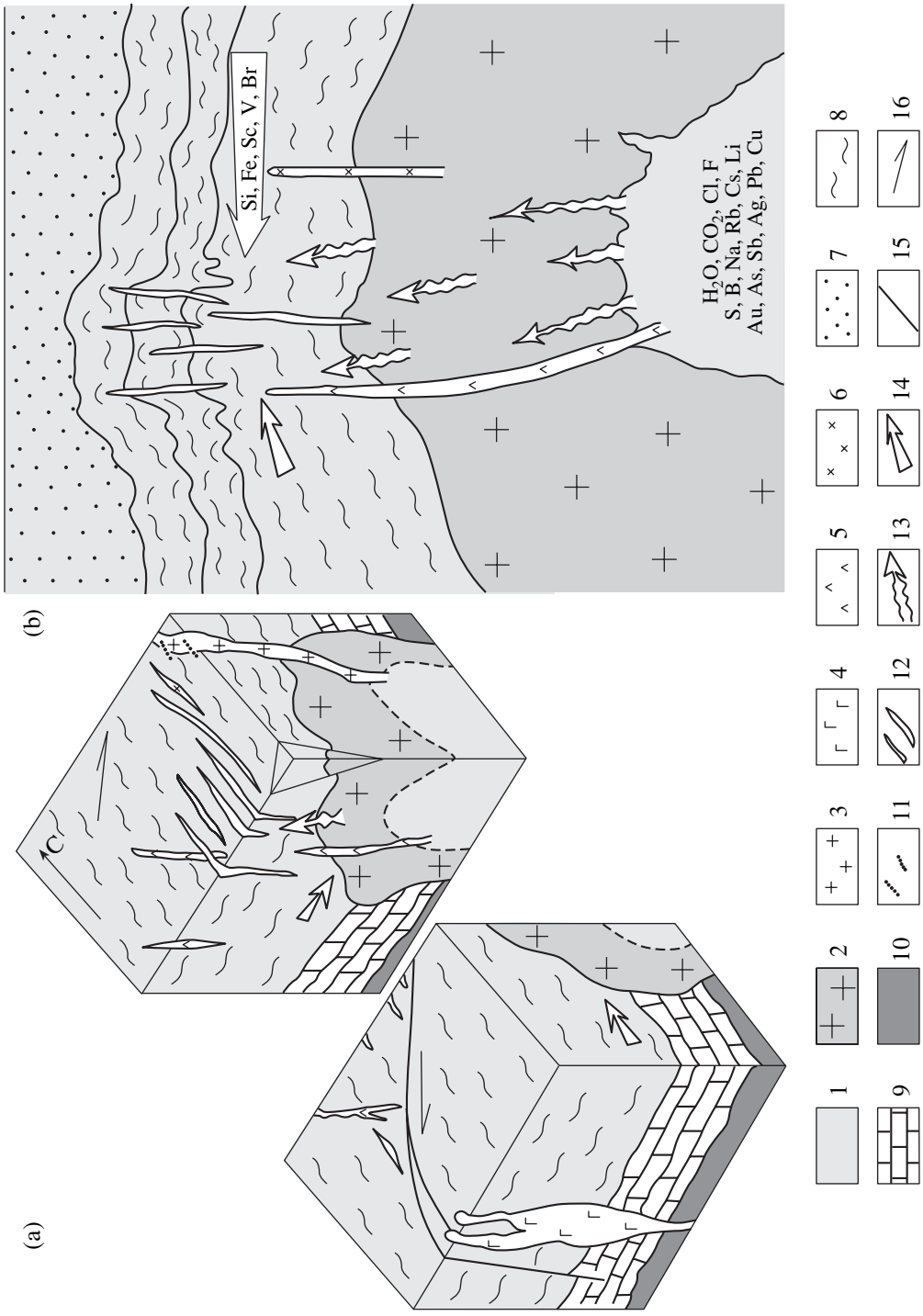

Fig. 19. Models of formation of the Nezhdaninsky deposit. (a) Geological–tectonic model of the stage of gold–quartz vein formation (105 Ma); (b) geochemical model of the ore-forming system. (1) Magmatic melt; (2) granitoids; (3) granite and granodiorite (Kurum pluton); (4) gabbrodiorite (Gel'dy stocks); (5) lamprophyre; (6) microdiorite; (7) Upper Permian–Triassic sandstone and conglomerate; (8) Carboniferous–Lower Permian intercalating mudstone, siltstone, and sandstone; (9) Lower Carboniferous limestone; (10) Devonian volcanic and sedimentary rocks; (11) Au–Mo–W veins; (12) gold–quartz veins; (13) magmatic fluid; (14) extraction of components from country rocks; (15) faults; (16) movement of tectonic blocks.

lor and Sheppard, 1986). Thus, the oxygen isotopic composition of fluid indicates that magmatic water participated in the ore formation.

The data obtained allowed us to extend our ideas on a genetic model of the Nezhdaninsky ore field, which was formed as a result of complex, multistage regional geodynamic evolution and is localized at the intersection of several deep-rooted faults. The gold ore is closely related in time and space to the emplacement of silicic and intermediate intrusive rocks. No rocks that underwent amphibolite facies metamorphism are known in the ore field or nearby. The ore was deposited from H_2O–CO_2 fluids with a low salt concentration and variable sulfur, carbon, and oxygen isotopic compositions (Bortnikov et al., 1998a).

The Nezhdaninsky deposit is situated in an area that underwent complex geodynamic evolution, reflected in magmatism and ore mineralization. As was mentioned above, the Nezhdaninsky hydrothermal–magmatic system originated 126–121 Ma ago (Bakharev, 2002). This time corresponded to the final stage of the Uda subduction resulting in the decompression–dissipative melting of the lower crust (Bakharev et al., 2002) beneath the South Verkhoyansk Synclinorium (Fig. 18). Ascending, the melt temporarily stopped at the boundary of the sedimentary cover and the pre-Riphean crystalline basement, forming an intermediate magmatic chamber. A part of the melt penetrated further into the sedimentary cover and crystallized as the Kurum pluton at a depth corresponding to a pressure of 100 MPa. The Au–Mo–W veins were formed at the final stage of this process 110 Ma ago.

A new phase of deformation 110–105 Ma ago was related to the origination of a new Benioff zone and the initial evolution of the Okhotsk–Chukotka volcanic–plutonic belt. This event gave rise to activation of the intermediate chamber. A lamprophyric, malchite-type magma had been formed as a product of the decompression–dissipative melting of still incompletely solidified early cumulates that resided in the lower portion of the magma chamber and then was extruded into the upper layers of the sedimentary cover as lamprophyre dikes. The fluid that separated from the intermediate chamber afterward gave rise to the formation of economic gold–quartz ore. Deformation resulted in metamorphism of host rocks, while emplacement of igneous rocks was accompanied by contact metamorphism of country rocks. These processes led to dehydration and decarbonation of sedimentary rocks and formation of a H_2O–CO_2 fluid with an admixture of CH_4 and N_2. Finally, a convective cell involved meteoric water in the hydrothermal system. Interacting with host rocks, this water turned into mineral-forming fluid. Precisely these processes ensured recovery of REE, LILE, and probably gold from host rocks and their dissolution in mineral-forming fluids. This event occurred not later than 105–100 Ma ago (Fig. 19).

The Okhotsk subduction not only reactivated the Nezhdaninsky ore–magmatic system but also provoked the inception of a new such system related to the Gel'dy stocks (Bakharev and Zaitsev, 2000).

The trace element composition of fluid inclusions indicates the close relations of fluids formed at the gold-ore and Au–Mo–W stages as concerns ore-forming components and the assortment of granitophile elements and their concentrations and ratios. These data confirm the previously stated view on Au-bearing veins and Au–Mo–W mineralization as derivatives of a common hydrothermal–magmatic system. In our opinion, the data obtained suggest that formation of the deposit was related to igneous activity, which ensured the generation of fluid, the direct supply of chemical elements from the magma chamber, and their mobilization as products of dehydration and decarbonation induced by contact and regional metamorphism.

ACKNOWLEDGMENTS

We thank V.V. Yarmolyuk and V.B. Naumov for their critical comments and S.A. Gorbacheva, E.O. Dubinina, A.A. Avdeenko, Yu.V. Vasyuta, and I.V. Grigor'eva for analytical results. This study was supported by the Program of Basic Research of the Division of Earth Sciences, Russian Academy of Sciences, and by the Russian Foundation for Basic Research (project nos. 05-05-64803, 06-05-64369, and 06-05-96070). O.V.V. is grateful to the Council for Grants of the President of the Russian Federation (grant no. MK-510.2006.5).

REFERENCES

1. V. V. Alpatov, "Disseminated Gold Mineralization in the Nezhdaninsky Deposit," Otech. Geol., No. 6, 63–65 (1998).
2. V. V. Alpatov, "Zoning of Disseminated Gold Mineralization in the Nezhdaninsky Gold Deposit," Otech. Geol., No. 6, 15–19 (2003).
3. V. S. Antipin, V. I. Kovalenko, and I. D. Ryabchikov, *Partition Coefficients of Trace Elements in Igneous Rocks* (Nauka, Moscow, 1984) [in Russian].
4. G. A. Armbrust, J. Oyarzun, and J. Arias, "Rubidium as a Guide to Ore in Chilean Porphyry Copper Deposits," Econ. Geol. **72**, 1086–1100 (1977).
5. A. Audetat, D. Gunter, and C. A. Heinrich, "Magmatic-Hydrothermal Evolution in a Fractionating Granite: A Microchemical Study of the Sn–W–F–Mineralized Mole Granite (Australia)," Geochim. Cosmochim. Acta **64** (19), 3373–3393 (2000).
6. T. Baker, S. Ebert, C. Rombach, and C. G. Ryan, "Chemical Composition of Fluid Inclusions in Intrusion-Related Gold Systems, Alaska and Yukon, Using PIXE Microanalysis," Econ. Geol. **101**, 311–327 (2006).
7. A. G. Bakharev, "Magmatism of the Nezhdanino Magmatic Ore Cluster," Otech. Geol., No. 4, 5–8 (1999a).
8. A. G. Bakharev, "Indicator Minerals of Deep Magmatic Processes in the Nezhdaninsky Magmatic Ore Cluster," in *Abstracts of Papers. IX Congress of Russian Mineral-*

ogical Society (St. Petersburg, 1999b), pp. 50–51 [in Russian].

9. A. G. Bakharev and A. I. Zaitsev, "Reanimated Nezhdaninsky Au-Bearing Ore–Magmatic System," in *Proceedings of the 11th All-Russia Petrographic Conference* (Syktyvkar, 2000), Vol. 1, pp. 145–147 [in Russian].
10. A. G. Bakharev, V. V. Alpatov, and A. I. Zaitsev, "Geological and Genetic Model of the Nezhdaninsky Au-bearing Ore–Magmatic System," Otech. Geol., No. 4, 3–7 (2002).
11. M. Bau and P. Möller, "Rare Earth Elements Fractionation in Metamorphogenic Hydrothermal Calcite, Magnesite, and Siderite," Mineral. Petrol. **45**, 231–246 (1992).
12. F. P. Bierlein and S. Maher, "Orogenic Disseminated Gold in Phanerozoic Fold Belts. Examples from Victoria, Australia and Elsewhere," Ore Geol. Reviews **17**, 215–232 (2001).
13. R. J. Bodnar and M. O. Vityk, "Interpretation of Microthermometric Data for H_2O–NaCl Fluid Inclusions," in *Fluid Inclusions in Minerals: Methods and Applications* (Siena, Pontignano, 1994), pp. 117–130.
14. J. K. Boehlke and J. J. Irvin, "Laser Microprobe Analyses of Cl, Br, I, and K in Fluid Inclusions: Implications for Sources of Salinity in Some Ancient Hydrothermal Fluids," Geochim. Cosmochim. Acta **56**, 203–225 (1992).
15. A. S. Borisenko, "Cryometric Analysis of Salt Composition from Fluid Inclusions in Minerals," Geol. Geofiz. **18** (8), 16–27 (1977).
16. N. S. Bortnikov, "Mineralogy, Geochemistry, and Origin of the Black Shale Hosted Gold Deposits of the Former Soviet Union," in *Mineral Deposits: From Their Origin to Their Environmental Impacts* (Prague, 1995), pp. 935–937.
17. N. S. Bortnikov, "Geochemistry and Origin of the Ore-Forming Fluids in Hydrothermal–Magmatic Systems in Tectonically Active Zones," Geol. Rudn. Mestorozhd. **48** (1), 1–26 (2006) [Geol. Ore Deposits **48** (1), 1–22 (2006)].
18. N. S. Bortnikov, G. N. Gamyanin, V. B. Naumov, and L. P. Nosik, "The Nezhdaninskoye Mesothermal Gold Deposit, Russia: Ore-Forming Fluid and Deposition Environment," in *Current Research in Geology Applied to Ore Deposits* (Univ. Granada, Granada, 1993), pp. 419–422.
19. N. S. Bortnikov, V. Yu. Prokof'ev, and N. V. Razdolina, "Origin of the Charmitan Gold–Quartz Deposit (Uzbekistan)," Geol. Rudn. Mestorozhd. **38** (3), 238–257 (1996) [Geol. Ore Deposits **38** (3), 208–226 (1996)].
20. N. S. Bortnikov, V. N. Sazonov, I. V. Vikentyev, et al., "The Berezovsky Giant Gold Quartz Deposit, Urals, Russia: Fluid Inclusion and Stable Isotope Studies," in *Mineral Deposits: Research and Exploration—Where Do They Meet?* (Balkema, Rotterdam, 1997), pp. 157–160.
21. N. S. Bortnikov, G. N. Gamyanin, V. V. Alpatov, et al., "Mineralogy, Geochemistry and Origin of the Nezhdaninsky Gold Deposit (Sakha-Yakutia, Russia)," Geol. Rudn. Mestorozhd. **40** (2), 137–156 (1998a) [Geol. Ore. Deposits **40** (2), 121–138 (1998a)].
22. N. S. Bortnikov, V. N. Sazonov, O. V. Vikent'eva, et al., "Role of the Magmatogenic Fluid in the Formation of the Mesothermal Berezovsky Gold–Quartz Deposit, Urals," Dokl. Akad. Nauk **363** (2), 82–85 (1998b) [Dokl. Earth Sci. **363** (8), 1078–1081 (1998b)].
23. N. S. Bortnikov, I. A. Bryzgalov, N. N. Krivitskaya, et al., "The Maiskoe Multistage Stringer–Disseminated Gold–Sulfide Deposit (Chukotka, Russia): Mineralogy, Fluid Inclusions, Stable O and S Isotopes, Evolution and Origin," Geol. Rudn. Mestorozhd. **46** (6), 475–509 (2004) [Geol. Ore Deposits **46** (6), 409–440 (2004)].
24. T. S. Bowers and G. H. Helgeson, "Calculation of the Thermodynamic and Geochemical Consequences of Nonideal Mixing in the System H_2O–CO_2–NaCl on Phase Relations in Geologic Systems. Equation of State for H_2O–CO_2–NaCl Fluids at High Pressures and Temperatures," Geochim. Cosmochim. Acta **47**, 1247–1275 (1983).
25. V. A. Buryak, I. S. Nemenman, N. V. Berdnikov, et al., "Fluid Regime of Formation and a Source of Ore-Forming Solutions of Gold–Quartz Veins in the Allakh–Yun Zone," Tikhookean. Geol. **9** (3), 62–70 (1990).
26. A. R. Campbell, D. A. Banks, S. R. Phillips, and B. W. D. Yardley, "Geochemistry of Th–U–REE Mineralizing Magmatic Fluids, Capitan Mountains, New Mexico," Econ. Geol. **90**, 1271–1287 (1995).
27. G. M. Claypool and J. R. Kaplan, "The Origin and Distribution of Methane in Marine Sediments," in *Natural Gases in Marine Sediments* (Plenum Press, New York, 1974), Vol. 3, p. 132.
28. P. L. P. Collins, "Gas Hydrates in CO_2-Bearing Fluid Inclusions and the Use of Freezing Data for Estimation of Salinity," Econ. Geol. **74**, 1435–1444 (1979).
29. K. C. Condie, *Archean Greenstone Belts* (Elsevier, Amsterdam, 1981).
30. R. S. Darling, "An Extended Equation to Calculate NaCl Contents from Final Clathrate Melting Temperatures in H_2O–CO_2–NaCl Fluid Inclusions: Implications for *P-T*-Isochores Location," Geochim. Cosmochim. Acta **55**, 3869–3871 (1991).
31. V. V. Distler, M. A. Yudovskaya, G. L. Mitrofanov, et al., "Geology, Composition, and Genesis of the Sukhoi Log Noble Metal Deposit, Russia," Ore Geol. Reviews **24** (1–2), 7–44 (2004).
32. S. V. Efremova and K. G. Stafeev, *Petrochemical Methods of Rock Examination. Handbook* (Nedra, Moscow, 1985) [in Russian].
33. R. W. Faibridge, *The Encyclopedia of Geochemistry and Environmental Sciences* (Dowdwen, Stroudsburg, 1972).
34. G. B. Fershtater, L. V. Malakhova, N. S. Borodina, et al., *Eugeosynclinal Gabbro–Granite Series* (Nauka, Moscow, 1984) [in Russian].
35. A. G. Galley, "Composite Synvolcanic Intrusions Associated with Precambrian VMS-Related Hydrothermal Systems," Miner. Deposita **38**, 443–473 (2003).
36. G. N. Gamyanin and G. A. Grinberg, "Cordierite and Garnet from Pegmatites of the Kurum Pluton," in *Magmatism of the Northeast of the USSR* (Nauka, Moscow, 1973), pp. 89–92 [in Russian].
37. G. N. Gamyanin, M. K. Silichev, N. A. Goryachev, and N. V. Belozertseva, "Polygenetic Gold Deposits," Geol. Rudn. Mestorozhd. **27** (5), 86–89 (1985).
38. G. N. Gamyanin, N. S. Bortnikov, and V. V. Alpatov, *The Nezhdaninsky Gold Deposit—a Unique Deposit in the*

Northeastern Russia (GEOS, Moscow, 2000) [in Russian].

39. G. N. Gamyanin, N. A. Goryachev, A. G. Bakharev, et al., *Origin and Evolution of Gold-Ore Granitoid Magmatic Systems in the Mesozoides of Northeast Asian* (SVKNII, Magadan, 2003) [in Russian].
40. A. D. Genkin, N. S. Bortnikov, L. Cabri, et al., "A Multilevel Study of Invisible Gold in Arsenopyrite from Four Mesothermal Gold Deposits in Siberia, Russian Federation," Econ. Geol. **93** (24), 463–487 (1998).
41. M. Ghaderi, M. Palin, I. H. Campbell, and P. J. Sylvester, "Rare Earth Element Systematic in Scheelite from Hydrothermal Gold Deposits in the Kalgoorlie–Norseman Region, Western Australia," Econ. Geol. **94**, 423–438 (1999).
42. R. J. Goldfarb, D. L. Leach, S. C. Rose, and G. P. Landis, "Fluid Inclusion Geochemistry of Gold-Bearing Quartz Veins of the Juneau Gold Belt, Southeastern Alaska: Implications for Ore Genesis," Econ. Geol., Monogr. **6**, 363–375 (1989).
43. R. J. Goldfarb, R. J. Newberry, W. J. Pickthhorn, and C. L. Gent, "Oxygen, Hydrogen and Sulfur Isotope Studies in the Juneau Gold Belt, Southeastern Alaska: Constraints on the Origin of Hydrothermal Fluids," Econ. Geol. **86**, 66–80 (1991).
44. G. J. S. Govett, *Rock Geochemistry in Mineral Exploration. Handbook of Exploration Geochemistry* (Elsevier, Amsterdam, 1985), Vol. 3.
45. T. H. Green, "Garnet in Silicic Liquids and Its Possible Use as a P–T Indicator," Contrib. Mineral. Petrol. **65**, 59–67 (1977).
46. G. A. Grinberg, *Precambrian of the Okhotsk Massif* (Nauka, Moscow, 1968) [in Russian].
47. G. A. Grinberg, A. G. Bakharev, G. N. Gamyanin, et al., *Granitoids of Southern Verkhoyan'e* (Nauka, Moscow, 1970) [in Russian].
48. D. I. Groves, R. J. Goldfarb, F. Robert, and C. J. R. Hart, "Gold Deposits in Metamorphic Belts: Overview of Current Understanding, Outstanding Problems, Future Research, and Exploration Significance," Econ. Geol. **98**, 1–29 (2003).
49. D. I. Groves, K. C. Condie, R. J. Goldfarb, et al., "Secular Changes in Global Tectonic Processes and Their Influence on the Temporal Distribution of Gold-Bearing Mineral Deposits," Econ. Geol. **100**, 203–224 (2005).
50. C. J. Hodgson, D. A. Love, and J. V. Hamilton, "Giant Mesothermal Gold Deposits: Descriptive Characteristics, Genetic Model and Exploration Area Selection Criteria," in *Giant Ore Deposits. SEG SP-2* (1993), pp. 157–206.
51. *Interpretation of Geochemical Data. Textbook*, Ed. by E. V. Sklyarov (Intermet Engineering, Moscow, 2001) [in Russian].
52. S.-Y. Jiang, J.-M. Yu, and J.-J. Lu, "Trace and Rare-Earth Element Geochemistry in Tourmaline and Cassiterite from the Yunlong Tin Deposit, Yunnan, China: Implication for Migmatitic-Hydrothermal Fluid Evolution and Ore Genesis," Chem. Geol. **209**, 193–213 (2004).
53. V. A. Kalyuzhny, *Principles of the Theory on Mineral-Forming Fluids* (Naukova Dumka, Kiev, 1982) [in Russian].
54. R. Kerrich, "Source Processes for Archean Au–Ag Vein Deposits: Evidence from Lithophile-Element Systematic of the Hollinger-McInture and Buffalo Ankerite Deposits, Timmins," Can. J. Earth Sci. **26**, 755–781 (1989).
55. R. Kerrich and B. J. Fryer, "Lithophile-Element Systematic of Archean Greenstone Belt Au–Ag Vein Deposits: Implications for Source Processes," Can. J. Earth Sci. **25**, 945–953 (1988).
56. R. Kerrich, R. J. Goldfarb, D. I. Groves, and S. Garwin, "The Geodynamics of World-Class Gold Deposits: Characteristics, Space-Time Distribution, and Origins," Reviews Econ. Geol **13**, 501–551 (2000).
57. M. M. Konstantinov, E. M. Nekrasov, A. A. Sidorov, and S. F. Struzhkov, *Gold-Ore Giants of Russia and the World* (Nauchnyi Mir, Moscow, 2000) [in Russian].
58. V. I. Kovalenko, V. V. Yarmolyuk, E. B. Sal'nikova, et al., "Sources of Igneous Rocks and Genesis of the Early Mesozoic Tectonomagmatic Area of the Mongolian–Transbaikalian Igneous Province: 2. Petrology and Geochemistry," Petrologiya **11** (3), 227–254 (2003) [Petrology **11** (3), 205–229 (2003)].
59. S. G. Kryazhev, Yu. V. Vasyuta, and M. K. Kharrasov, "Technique of Bulk Chemical Analysis of Inclusions in Quartz," in *Proceedings of XI International Congress on Thermobarogeochemistry* (VNIISIMS, Aleksandrov, 2003), pp. 6–10 [in Russian].
60. N. K. Kurbanov, Ch. Kh. Arifulov, P. G. Kucherevsky, et al., "Geological and Genetic Models of Gold Deposits in Carbonaceous Terrigenous Complexes," Rudy Metally, No. 2, 55–69 (1994).
61. R. B. Larsen, "The Distribution of Rare Earth Elements in K-Feldspar as an Indicator of Petrogenetic Processes in Granitic Pegmatites: Examples from Two Pegmatite Fields in Southern Norway," Can. Mineral. **40**, 137–151 (2002).
62. Y. Matsuhisa, J. R. Goldsmith, and R. N. Clayton, "Oxygen Isotopic Fractionation in the System Quartz–Albite–Anorthite–Water," Geochim. Cosmochim. Acta **43**, 1131–1140 (1979).
63. T. C. McCuaig and R. Kerrich, "*P-T-t*–Deformation–Fluid Characteristics of Lode Gold Deposits: Evidence from Alteration Systematic," Ore Geol. Reviews **12**, 381–453 (1998).
64. A. Miltra, H. Elderfield, and M. J. Greaves, "Rare Earth Elements in Submarine Hydrothermal Fluids and Plumes from the Mid-Atlantic Ridge," Mar. Chem. **46**, 217–235 (1994).
65. W. P. Nash and H. R. Crecraft, "Partition Coefficients for Trace Elements in Silicic Magmas," Geochim. Cosmochim. Acta **49**, 2309–2322 (1985).
66. V. B. Naumov, "Possibilities to Determine Pressure and Density of Mineral-Forming Media from Inclusions in Minerals," in *Application of Thermobarogeochemical Methods for Exploration and Study of Ore Deposits* (Nedra, Moscow, 1982), pp. 85–94 [in Russian].
67. B. E. Nesbitt, "Phanerozoic Gold Deposits in Tectonically Active Continental Margins," in *Gold Metallogeny and Exploration* (Blackie, 1991), pp. 104–132.
68. B. E. Nesbitt and K. Muchlenbachs, "Geology, Geochemistry, and Genesis of Mesothermal Lode Gold Deposits of the Canadian Cordillera: Evidence for Ore Formation from Evolved Meteoric Water," Econ. Geol. Monogr. **6**, 553–563 (1989).

69. H. Ohmoto, "Stable Isotope Geochemistry of Ore Deposits," Review Mineral. **16**, 491–560 (1986).
70. J. A. Pearce, N. B. W. Harris, and A. G. Tindle, "Trace Element Discrimination Diagrams for the Tectonic Interpretation of Granitic Rocks," J. Petrology **25** (4), 956–983 (1984).
71. G. Pike, R. Cas, and R. H. Smithies, "Geologic Constraints on Base-Metal Mineralization of the Whim Creek Greenstone Belt, Pilbara Craton, Western Australia," Econ. Geol. **97**, 827–845 (2002).
72. V. Yu. Prokof'ev and V. B. Naumov, "Geochemical Features of Ore-Forming Solutions at the Zyryanovsk Base-Metal Massive Sulfide Deposit," Geokhimiya **25** (3), 375–386 (1987).
73. V. Yu. Prokof'ev, I. S. Peretyazhko, S. Z. Smirnov, et al., *Boron and Boric Acids in Endogenic Ore-Forming Fluids* (Pas'va, Moscow, 2003) [in Russian].
74. A. V. Prokop'ev, A. G. Bakharev, Kh. Toro, et al., "Middle Paleozoic Marginal Continental Magmatism and Mesozoic Metamorphic Events in the Junction Zone of the North Asian Craton and the Okhotsk Terrane: New Geochemical and Geochronological Data and Their Geodynamic Interpretation," Otech. Geol., No. 6, 57–64 (2003).
75. E. Roedder, *Fluid Inclusions in Minerals* (Reviews in Mineralogy, Mineral. Soc. Amer., 1984, Vol. 12; Mir, Moscow, 1987).
76. J. R. Ridley and L. W. Diamond, "Fluid Chemistry of Orogenic Lode Gold Deposits and Implications for Genetic Models," in *Gold in 2000. SEG Reviews* (2000), Vol. 13, pp. 141–162.
77. E. I. Semenov, *Ores and Minerals of Rare Earth Elements, Thorium, and Uranium* (GEOS, Moscow, 2001) [in Russian].
78. D. M. Shaw, "A Review of K–Rb Fractionation Trends by Covariance Analysis," Geochim. Cosmochim. Acta **32**, 573–601 (1968).
79. R. L. Sherlock, T. Roth, E. T. C. Spooner, and C. J. Bray, "Origin of the Eskay Creek Precious Metal-Rich Volcanogenic Massive Sulfide Deposit: Fluid Inclusion and Stable Isotope Evidence," Econ. Geol. **94**, 803–824 (1999).
80. A. A. Sidorov and I. N. Tomson, "Black Shale Mineralization: Convergence of Alternative Concepts," Vestn. Ross. Akad. Nauk **70** (8), 719–724 (2000).
81. S. R. Taylor and S. M. McLennan, *The Continental Crust: Its Composition and Evolution* (Blackwell, Oxford, 1985; Mir, Moscow, 1988).
82. H. P. Taylor, Jr. and S. M. F. Sheppard, "Igneous Rocks," in *Processes of Isotopic Fractionation and Isotope Systematic. Stable Isotopes in High Temperature Geological Processes*, Review Mineral. **16**, 227–272 (1986).
83. R. Thiery, A. M. Kerkhof, and J. Dubessy, "VX Properties of CH_4–CO_2 and CO_2–N_2 Fluid Inclusions: Modeling for $T < 31°C$ and $P < 400$ Bars," Eur. J. Mineral., No. 6, 753–771 (1994).
84. S. D. Velikoslavinsky, "Geochemical Typification of Silicic Igneous Rocks in Major Geodynamic Settings," Petrologiya **11** (4), 363–380 (2003) [Petrology **11** (4), 327–342 (2003)].
85. V. A. Zharikov, "Physicochemical Study of Wall-Rock Metasomatism," Geokhimiya **25** (12), 1754–1779 (1987).
86. V. A. Zharikov and B. I. Omel'yanenko, "Some Problems of Studying Host Rock Alteration in Line with Metallogenic Research," in *The Study of Ore Mineralization Localization During Metallogenic Investigations in Ore Districts* (Nedra, Moscow, 1965), pp. 119–194 [in Russian].